REPORT DOCUMENTATION PAGE

1. REPORT DATE *(DD-MM-YYYY)* 30-09-2009	2. REPORT TYPE Final Report	3. DATES COVERED *(From - To)* 1 June. 2006 – 30 Sept. 2009

4. TITLE AND SUBTITLE
Experimental and Numerical Characterization of Polymer Nanocomposites for Solid Rocket Motor Internal Insulation – Final Report

5a. CONTRACT NUMBER

5b. GRANT NUMBER
FA9550-06-1-0356

5c. PROGRAM ELEMENT NUMBER

6. AUTHOR(S)
Koo, J. H., Ezekoye, O. A., Bruns, M. C., and Lee, J. C.

5d. PROJECT NUMBER

5e. TASK NUMBER

5f. WORK UNIT NUMBER

7. PERFORMING ORGANIZATION NAME(S) AND ADDRESS(ES)

The University of Texas at Austin, Dept. of
Mechanical Engineering, 1 University
Station, C2200, Austin, TX 78712-0292

8. PERFORMING ORGANIZATION REPORT NUMBER

9. SPONSORING / MONITORING AGENCY NAME(S) AND ADDRESS(ES)
Dr. Charles Y-C Lee
AFOSR/NL
875 N. Randolph St., Ste. 325
Arlington, VA 22203

10. SPONSOR/MONITOR'S ACRONYM(S)
AFOSR

11. SPONSOR/MONITOR'S REPORT NUMBER(S)
AFRL-OSR-VA-TR-2012-0434

12. DISTRIBUTION / AVAILABILITY STATEMENT

Approved for public release; distribution unlimited

13. SUPPLEMENTARY NOTES

14. ABSTRACT Research objective is to develop a modeling framework for simulating the insulative behavior of thermoplastic polyurethane elastomer nanocomposites (TPUNs) for solid rocket motors (SRMs). This research combines numerical modeling and experimental characterization of TPUNs for SRM insulation. Two families of TPUNs based on nanoclay, carbon nanofiber (CNF), and multiwall carbon nanotubes (MWNT) were developed. TGA experiments were conducted on Kevlar-EPDM, TPU, TPUN-clay, TPUN-CNF, and TPUN-MWNT in both air and nitrogen at low heating rates. Kinetics was calculated using isoconversion technique. High heating rate TGA was conducted on selective TPUNs. Flammability tests indicated TPUN-clay has the toughest char, followed by TPUN-MWNT, then TPUN-CNF. We connected the population balance framework to atomistic calculations to determine what aspects of the atomistic simulations would likely affect the meso-scale evolution. We focused on understanding the role that the scission kernel has on the overall degradation process and also on the role of the stoichiometry parameter has on the overall degradation kinetics. We began using the atomistic simulation code RXN MD to compute scission kinetics parameters. We recognized that the critical issue in characterizing a particular materials ablation rate could be captured by investigating the steady state ablation process. The meso-scale (mechanistic) modeling is integral to understanding what pyrolysis products form during the decomposition process and how these products affect the char.

15. SUBJECT TERMS Ablation Modeling, Population Balance Equation, Solid Rocket Motor Internal Insulation, Polymer Nanocomposites, Thermoplastic Elastomer, Surface Modified MMT Clay, Multiwall Carbon Nanotubes, and Carbon Nanofibers

16. SECURITY CLASSIFICATION OF:			17. LIMITATION OF ABSTRACT	18. NUMBER OF PAGES	19a. NAME OF RESPONSIBLE PERSON Joseph H. Koo, Sc.D.
a. REPORT U	b. ABSTRACT U	c. THIS PAGE U	U	119	19b. TELEPHONE NUMBER *(include area code)* (512) 589-4170

TABLE OF CONTENTS

LIST OF FIGURES

Figure 3.74 Bond location distribution for 25 unit PE chain.

LIST OF TABLES

EXECUTIVE SUMMARY

Research Objective

The objective of this research is to develop a modeling framework for simulating the insulative behavior of thermoplastic polyurethane elastomer nanocomposites (TPUNs) for solid rocket motors (SRMs) and the creation of software capable of predicting the properties of these TPUNs.

Research Approach

The proposed research combines numerical modeling and experimental characterization of TPUNs for SRM insulation. The TPUN thermophyscial properties and kinetic parameters are to be found using thermogravimetric analysis, Multi-Function Sensor (MFS) gauges, and other thermal analysis techniques. Numerical techniques for small scale physics from molecular dynamics (MD) simulations through population balance methods will be used to gain insight and intuition on the interactions between the polymeric and inorganic materials. These insights will help us to develop macroscopic kinetic models/descriptions which can be embedded in macroscale continuum models. These models will be first exercised against the thermogravimetric data and data generated from the MFS gauges. Subsequently, small scale experiments using the low heat flux radiant panel, simulated solid rocket motor (SSRM), and LHMEL facility with known heating conditions and well-controlled experiments will be conducted to provide us with data to further verify and validate the numerical code. The numerical code and model will also be validated with meso-scale experiments using AFRL 2-lb Pi-K and 15-lb Bates SRM firings. Once this code is validated, numerical experiments with the code will help us to design optimized compositions of new TPUNs.

Scientific Relevance

The mechanisms through which the addition of nanoparticles modifies the decomposition of thermoplastic elastomers are not fully understood. One promising method for understanding these mechanisms is through the use of atomistic simulations such as Molecular Dynamics (MD). Because of the time scales over which MD simulations must be conducted, it has not been obvious how to incorporate MD findings into continuum type simulations. Further, reacting molecular dynamics simulation are still very much in their infancy as far as the ability to predict the degradation of complex polymeric systems. During our studies we anticipated that a critical scientific breakthrough could occur if we are able to develop a mechanistic description of the polymer-inorganic material coupling process that can reside in a continuum code. The approach proposed required a meso-scale modeling strategy that took the model form for the decomposition processes that occurs when the system is viewed from an atomistic perspective and estimating critical parameters from optimization and other techniques to close the model form.

One meso-scale approach that has merit is rooted in probabilistic approaches for transitions of bonds. We have focused attention on population balance equations where a notional particle description of the polymer and inorganic material distributions is used. In population balance treatment of aerosols, kinetics of breakage and coalescence are

often included in continuum codes. There is a striking analogy between polymer bond breakage and subsequent capture by nanoparticles and aerosol aggregate breakage and subsequent capture by a scrubber particle. We have exercised the population balance methodology and have used lower scale molecular dynamics research to move towards development of a continuum kinetic description of thermoplastic degradation. This approach and continued work on expanding the techniques could create important scientific contributions to facilitate the Air Force's identification and design of new and future compositions for SRM insulation materials.

Annual Progress

This report summarizes the first two years' highlights and accomplishments and the past 12 months of our research effort from Oct. 1, 2008 to Sept. 30, 2009. During this period, we made significant progress in the experimental and modeling areas.

Experimental

We performed TGA on formulations of Kevlar-EPDM, TPU (Desmopan™ DP 6065A), TPUN-clay, TPUN-carbon nanofiber (CNF), and TPUN-multiwall carbon nanotube (MWNT) in nitrogen to study their thermal degradation at low heating rates. TGA data were used for kinetics calculations. High heating rate TGA experiments were conducted on selective TPU and TPUNs. A concern is raised using low heating rate TGA data for high heating rate application. We conducted extensive flammability test using UL 94 test method and studied the microstructures of post-test TPUN specimens to compare the char strength of TPUNs. The following is a summary of our experimental activities:

- Processed three TPUN families via twin screw extrusion using the new TPU (Desmopan™ DP 6065A), TPUN-clay (2.5, 5, 7.5, and 10% of Cloisite® 30B), TPUN-MWNT (2.5, 5, 7.5, and 10% of Graphistrength™ C100), and TPUN-CNF (2.5%, 5%, 10%, and 15% PR-19-XT LHT)

- Fabricated injection molded specimens of the new TPUNs for ablation, flammability, mechanical, physical, thermal, and thermophysical properties characterization

- Completed morphological analyses and physical (density and hardness) of TPUN-clay, TPUN-MWNT, and TPUN-CNF materials

- Studied the thermal degradation of Kevlar-EPDM, TPU (Desmopan™ DP 6065A), TPUN-clay, TPUN-MWNT, and TPUN-CNF at using TGA at low heating rates (5, 10, and 20°C/min) and determined their kinetic parameters using the isoconversion technique

- Conducted high heating rates (100, 250, and 500°C/min) TGA of TPU, TPUN-5% clay, and TPUN-5% MWNT and determined their kinetic parameters using isoconversion technique. This analysis suggested that the assumption of using low heating rate TGA data to describe high heating rate application would be a concern.

- Performed extensive flammability studies on neat TPU, TPUN-clay, TPUN-MWNT, TPUN-CNF using UL 94 test method; specimens were burnt at different

degrees and were examined under SEM

- Flame tests revealed the neat TPU burns and drips and the TPUN-clay specimens formed tougher char than neat TPU, followed by the TPUN-MWNT specimens, and TPUN-CNF specimens are the worst

- Shipped TPUN specimens to AFRL/Edwards for Pi-K char motor firing

- Fabricated TPUN specimens for SSRM ablation test at Texas State Univ.

Modeling

We worked on connecting the population balance framework to atomistic calculations to determine what aspects of the atomistic simulations would likely affect the meso-scale evolution. Specifically, we focused on understanding the role that the scission kernel has on the overall degradation process and also on the role of the stoichiometry parameter has on the overall degradation kinetics. In terms of connections with atomistic tools, we began using the atomistic simulation code RXN MD to compute scission kinetics parameters. On the large scale, we recognized that the critical issue in characterizing a particular materials ablation rate could be captured by investigating the steady state ablation process. This is a major finding that has implications in the overall analysis of material thermal response for ablative systems. However, there are significant challenges to the use of this approach that we have not worked out. In particular, we note that the decomposition products of ablation have a significant impact on the overall rate of ablation through their interaction with the char layer. We view the meso-scale (mechanistic) modeling as being integral to understanding what pyrolysis products form during the decomposition process. The following list is a summary of the progress made towards modeling of ablation:

- Recognized appropriateness of quasi-steady ablation model to clarify material effects on ablation rate

- Compared quasi-steady ablation results to results from Chaleur to see quasi-steady behavior

  - Performed parametric analysis of model forms in meso-scale model to understand sensitivities of model forms to decomposition process

- Exercised reacting molecular dynamics code to clarify approximations made in the meso-scale decomposition model

In summary, we presented/published 12 papers during this reporting period (Oct. 1, 2008 to Sept. 30, 2009).

Personnel Supported

Morgan C. Bruns	PhD student, Mechanical Engineering
Jason C. Lee	PhD student, Mechanical Engineering
David W. Ho	MS student, Mech. Engineering (Graduated 12/7)
Khiet C. Nguyen	MS student, Mech. Engineering (Graduated 12/7)
Christopher Lam	Undergraduate student, Mechanical Engineering

Ofodike A. Ezekoye, Ph.D.   Professor, Mechanical Engineering

Joseph H. Koo, Sc.D.   Senior Research Scientist, Mechanical Engineering

Publications and Presentations (as of Sept. 30, 2009)

A total of 35 technical papers were presented/published/prepared through the sponsorship of this research program for the past three years:

1. Koo, J. H., Ho, D. W., and Ezekoye, O. A., "A Review of Numerical and Experimental Characterization of Thermal Protection Materials – Part I. Numerical Modeling", Paper AIAA-2006-4936, *42nd AIAA/ASME/SAE/ASEE Joint Propulsion Conference*, Sacramento, CA, July 9-12, 2006.

2. Koo, J. H., and Ezekoye, O. A., "Experimental and Numerical Characterization of Polymer Nanocomposites for Solid Rocket Motor Internal Insulation – Annual Report (Report 1)," Annual Report to AFOSR, Arlington, VA, Sept. 30, 2006.

3. Koo, J. H., Ho, D. W., Bruns, M., and Ezekoye, O. A., "A Review of Numerical and Experimental Characterization of Thermal Protection Materials - Part II. Material Properties Characterization," Paper AIAA-2007-2131, *48th AIAA/ASME/ASCE/AHS Structures, Structural Dynamics, and Materials Conference*, Waikiki, HI, Apr. 23-26, 2007.

4. Ho, D. W., Koo, J. H., Bruns, M., and Ezekoye, O. A., "A Review of Numerical and Experimental Characterization of Thermal Protection Materials - Part III. Experimental Testing," Paper AIAA-2007-5773, *43rd AIAA/ASME/SAE/ASEE Joint Propulsion Conference*, Cincinnati, OH, July 8-11, 2007.

5. Bruns, M. C., Ezekoye, O. A., and Koo, J. H., "Determining Failure Time for Weak-Char Ablatives," Paper AIAA-2007-5772, *43rd AIAA/ASME/SAE/ASEE Joint Propulsion Conference*, Cincinnati, OH, July 8-11, 2007.

6. Nguyen, K., Koo, J. H., Ho, D. W., Bruns, M., and Ezekoye, O. A., "Experimental Characterization of Thermoplastic Polyurethane Nanocomposite under Extreme Conditions," Paper AIAA-2007-5770, *43rd AIAA/ASME/SAE/ASEE Joint Propulsion Conference*, Cincinnati, OH, July 8-11, 2007.

7. Luo, Z. P., and Koo, J. H., "Quantifying the dispersion of mixture microstructures," *J. of Microscopy*, 225 (22), 2007, pp. 118-125.

8. Koo, J. H., Ezekoye, O. A., Bruns, M. C., Ho, D. W., and Nguyen, K., "Experimental and Numerical Characterization of Polymer Nanocomposites for Solid Rocket Motor Internal Insulation – Annual Report (Report 2)," Annual Report to AFOSR, Arlington, VA, Sept. 30, 2007.

9. Koo, J. H., and Ezekoye, O.A. "1st Annual Program Review at AFRL/Edwards," Lancaster, CA, Dec. 2007.

10. Ho, D. W., "Determination of Kinetics Parameters and Char Microstructural Analysis of Thermoplastic Polyurethane Elastomer Nanocomposites for Propulsion Systems," MS thesis, Dept. of Mechanical Engineering, The University of Texas at Austin, Austin, TX, Dec. 2007.

11. Nguyen, K. C., "Experimental Characterization of Thermoplastic Polyurethane Elastomer Nanocomposites Under Extreme Conditions," MS thesis, Dept. of Mechanical Engineering, The University of Texas at Austin, Austin, TX, Dec. 2007.

12. Luo, Z. P., and Koo, J. H., "Determining the layer dispersion degree in polymer layered silicate nanocomposites by quantitative transmission electron microscopy," *Polymer*, 49, 2008, pp. 1841-1852.

13. Luo, Z. P., and Koo, J. H., "Quantitative electron microscopy of carbon nanofibers/nanotubes enhanced polymer nanocomposites," *Materials Letters*, 62, 2008, pp. 3493-3496.

14. Ezekoye, O.A., Bruns, M. C., and Koo, J. H., "Polymer Degradation using Population Balance Techniques," *NIST-BFRL 2008 Annual Fire Conference*, Mar. 31, 2008.

15. Bruns, M. C., Koo, J. H., and Ezekoye, O. A., "An Examination of Polymer Degradation and Heat Transfer using Population Balance Techniques," *2008 Spring Technical Meeting of the Central States of the Combustion Institute*, Tuscaloosa, AL, April. 2008.

16. Ho, D. W., Koo, J. H., and Ezekoye, O. A., "Thermoplastic Polyurethane Elastomer Nanocomposites: Morphology, Thermophysical, and Flammability," *Proc. International SAMPE 2008 Symposium and Exhibit*, Long Beach, CA, May 19-22, 2008.

17. Koo, J. H., Ezekoye, O.A., Bruns. M. C., and Lee, J. C., "Semi-Annual Program Review with AFRL/Edwards," Video Conference with AFRL/Edwards AFB personnel, UT-Austin, Austin, TX, June 2008.

18. Ho, D. W., Koo, J. H., Lee, J. C., and Ezekoye, O. A., "Thermophysical Properties Characterization of Thermoplastic Polyurethane Elastomer Nanocomposites," Paper AIAA-2008-5146, *44th AIAA/ASME/SAE/ASEE Joint Propulsion Conference*, Hartford, CT, July 21-23, 2008.

19. Luo, Z. P., and Koo, J. H., "Quantifying the layer dispersion degree in clay/polymer nanocomposites by advanced quantitative transmission electron microscopy," *Proc. MSA 2008 Meeting,* Albuquerque, NM, Aug. 3-7, 2008.

20. Ho, D. W., Koo, J. H., and Ezekoye, O. A., "Kinetics of Thermal Degradation of Thermoplastic Polyurethane Elastomer Nanocomposites," *Proc. International SAMPE 2008 Technical Conference,* Memphis, TN, Sept. 8-11, 2008.

21. Koo, J. H., Ezekoye, O. A., Bruns, Lee, J. C., M. C., Ho, and D. W., Nguyen, K., "Experimental and Numerical Characterization of Polymer Nanocomposites for Solid Rocket Motor Internal Insulation – Annual Report (Report 3)," Annual Report to AFOSR, Arlington, VA, Sept. 30, 2008.

22. Koo, J. H., and Ezekoye, O.A. "2nd Annual Program Review at AFRL/Edwards," Lancaster, CA, Dec. 2008.

23. Bruns, M. C., Koo, J. H., and Ezekoye, O. A., "Population-Based Models of Thermoplastic Degradation: Using Optimization to Determine Model Parameters," *Polym Deg Stab.*, 94, (2009), 1013-1022.

24. Ho, D. W., Koo, J. H., and Ezekoye, O. A., "Kinetics and Thermophysical Properties of Polymer Nanocomposites for Solid Rocket Motor Insulation," *J. of Spacecraft and Rockets,* 46 (3), (2009), 526-544.

25. Lee, J., Koo, J. H., and Ezekoye, O. A., "Flammability Studies of Thermoplastic Polyurethane Elastomer Nanocomposites," AIAA-2009-2544, *50th AIAA/ASME/ASCE/AHS/ASC Structures, Structural Dynamics, and Materials Conference*, Palm Spring, CA May 4-7, 2009.

26. Bruns, M. C., Ezekoye, O. A., and Koo, J. H., "Thermal Degradation of a Spatially Lumped Population of Thermoplastic Chains," *6th U.S. National Combustion Meeting*, An Arbor, MI, May 17-20, 2009.

27. Koo, J. H., Ezekoye, O. A., Bruns, M. C., and Lee, J. C., "Characterization of Polymer Nanocomposites for Solid Rocket Motor – Recent Progress," *Proc. International SAMPE 2009 ISSE,* Baltimore, MD, May 18-21, 2009.

28. Lee, J. C., Koo, J. H., Lam, C., Ezekoye, O. A., and Erickson, K., "Heating Rate and Nanoparticle Loading Effects on Thermoplastic Polyurethane Elastomer Nanocomposite Kinetics," AIAA-2009-4096, *AIAA Thermophysics Conference*, San Antonio, TX, June 22-25, 2009.

29. Koo, J. H., Nguyen, K. C., Lee, J. C., Ho, W. C., Bruns, M. C., and Ezekoye, O. A., "Flammability Studies of a Novel Class of Thermoplastic Elastomer Nanocomposites," *J. of Fire Sciences*, July 30 (2009) as doi: 10.1177/0734904109339616.

30. Lee, J. C., Koo, J. H., and Ezekoye, O. A., "Thermoplastic Polyurethane Elastomer Nanocomposites: Density and Hardness Correlation with Flammability Performance," AIAA-2009-5273, *AIAA Joint Propulsion Conference*, Denver, CO, Aug. 2-5, 2009.

31. Ho, D. W., Koo, J. H., and Ezekoye, O. A., "Thermoplastic Polyurethane Elastomer Nanocomposites: Morphology, Thermophysical, and Flammability Properties," *Journal of Nanomaterials*, (2009), under review.

32. Koo, J. H., Ezekoye, O. A., Bruns, and Lee, J. C., "Experimental and Numerical Characterization of Polymer Nanocomposites for Solid Rocket Motor Internal Insulation – Final Report (Report 4)," Final Report to AFOSR, Arlington, VA, Sept. 30, 2009.

33. Koo, J. H., Coates, G. R., Ho, D. W., Bruns, M. C., and Ezekoye, O. A., "A Comprehensive Review of Numerical Modeling and Experimental Characterization of Thermal Protection Materials," an invited paper to *J. of Spacecraft and Rockets* in preparation.

34. Lee, J. C., Koo, J. H., and Ezekoye, O. A., "Roles of Clay, Multiwall Carbon Nanotube, and Carbon Nanofiber to Flammability and Char Strength of

Thermoplastic Polyurethane Elastomer Nanocomposites," *J. of Fire Sciences* in preparation.

35. Koo, J. H., Ezekoye, O. A., Lee, J. C., and Bruns, M. C., "Rubber Composites with Layered Clays, Based on Thermoplastic Elastomers," in *Rubber Clay Nanocomposites*, M. Galimberti (eds.), Wiley & Sons, NY (2010) in preparation.

1. INTRODUCTION

Insulation materials are required to protect solid rocket motor (SRM) cases against hostile combustion gaseous products generated in the rocket chamber. Various internal system components must be protected from extreme flow temperatures of 1,000 to 4,000°C and highly abrasive particles ejected at velocities less than Mach 1 in the rocket combustion chamber. Kevlar®-filled ethylene-propylene-diene rubber (EPDM) is the baseline insulation material for solid rocket motor cases. A novel class of insulation materials was developed by the Air Force Research Laboratory that is lighter, exhibits better ablation performance and insulation characteristics and possesses a more cost-effective manufacturing process than the current baseline material [1-6]. We propose to develop a comprehensive numerical and experimental research program to understand the ablation and heat transfer characteristics of this new class of thermoplastic elastomer nanocomposites to facilitate the Air Force's identification and design efforts for new and future components of SRM insulation materials.

A subscale solid rocket Pi-K char motor developed by AFRL/PRSM was used to study the ablation characteristics of the insulation materials [1-6]. Testing insulative or ablative materials in full-scale firings is not only expensive, but also requires lengthy planning and limited exposure time. Thus reducing the number of samples and the variety of test conditions available is a worthwhile endeavor. The Pi-K char motor has been shown to be a cost-effective, "fast turnaround" device to evaluate different insulative materials under identical conditions for initial material screening and development. The Pi-K char motor was intended to be used in this study in collaboration with AFRL/Edwards AFB, CA researchers. Physical, mechanical, and thermophysical properties of these novel polymer nanocomposites (PNCs) have also been determined and compared with baseline materials [2].

Military interest in the use of polymer nanocomposites for ablatives has grown steadily since Vaia *et al.* [7] examined the ablative performance of polycaprolactam (nylon 6) nanocomposites. A relatively tough, inorganic char forms during the ablation of these nanocomposites resulting in at least an order-of-magnitude decrease in the mass loss (erosion) rate relative to the neat polymer. This occurs for as little as 2 wt% ($\approx$ 0.8 vol%) exfoliated mica-type layered silicate. Vaia *et al.* noted that the presence of the char layers does not alter the first-order decomposition kinetics of the polymer matrix. Instead, the nanoscopic distribution of silicate layers appears to create a uniform char layer that enhances the ablative performance. The formation of this char is only minutely influenced by the type of organic modification on the silicate surface of specific interactions between the polymer and the aluminosilicate surface, such as end-tethering of a fraction of the polymer chains through ionic interaction to the layer surface.

Patton *et al.* [8] reported the ablation, mechanical, and thermal properties of vapor grown carbon nanofiber (VGCF)/phenolic resin composites for potential usage in solid rocket motor nozzles. Composites specimens with varying loadings (30 to 50 wt%) including one sample with ex-rayon carbon fiber plies were prepared and exposed to a plasma torch for 20s with a heat flux of 16.5 MW/m^2 at approximately 1650°C. Low erosion rates and little char formation were observed. When fiber loadings increased, mechanical and ablative properties improved. The VGCF composites had low thermal

conductivities (approximately 0.56 W/m-K) indicating they are good insulating materials. If a 65% fiber loading in VGCF composite could be achieved, then ablative properties are projected to be comparable to or better than the composites currently used on the Space Shuttle Reusable Solid Rocket Motor (RSRM).

Koo *et al.* [9-13] reported a new class of polymer nanocomposites that are lighter and have better ablation performance and insulation characteristics than current state-of-the-art materials. For rocket nozzle ablative, MMT clay, VGCF, and POSS were incorporated into a resole phenolic and were impregnated into a rayon carbon fiber to fabricate into polymer matrix composites. Different loadings of MMT clay (2.5, 5, and 7.5 wt%), POSS (1, 3, and 5 wt%), and VGCF (20, 24, and 24 wt% without the rayon carbon fiber reinforcement) were incorporated into the phenolic resin. The simulated solid rocket motor (SSRM) was employed to test these nanocomposite rocket ablative materials (NRAMs) with an industry standard ablative (MX-4926, a carbon phenolic composite) using 14 MW/m^2 with Al$_2$O$_3$ particle loading simulating particle impingement for a test duration of 15s. The ablation rate of MX-4926 is about 0.4 mm/s. For the Clay-NRAM group, only the 7.5 wt% Clay-NRAM has a lower ablation rate than MX-4926. For the CNF-NRAM group, all three loadings have lower ablation rate than MX-4926 with 28% CNF-NRAM being the lowest. For the POSS-NRAM group, all three loadings have lower ablation rate than MX-4926 with 5 wt% POSS-NRAM being the lowest. All NRAMs have lower maximum backside heat-soaked temperature than MX-4926. The CNF-NRAM group has the lower heat-soaked temperature, followed by the POSS-NRAM group, then the Clay-NRAM group.

A recent review by Koo *et al.* [14] has shown continued progress in using polymer nanocomposites for rocket propulsion research. Polymer nanocomposites have been developed to enhanced materials' properties for high temperature applications. The feasibility of using polymer nanocomposites is clearly demonstrated for rocket propulsion insulation, rocket nozzle ablative materials, carbon/carbon composites, and damage tolerant high performance epoxy fiber-reinforced composite systems. MMT clay, nanosilica, VGCF, and POSS can be easily incorporated into various polymers using high shear processing and appropriate manufacturing techniques to form nanocomposites. The level and uniformity of nanoparticles dispersion in the polymer matrix is essential to achieve the desired properties' enhancement.

Elastomeric materials are used as internal ablative and insulative materials for rocket motor casings. Kevlar®-filled EPDM is the industry standard for this application. Since the elastic modulus of rubbers is low, they also act as absorbers during transportation and as insulators for extreme temperature changes during storage for the solid propellant. Temperature of the solid propellant combustion products often reaches several thousands of degrees. Due to the very short duration of exposure to high temperature on the elastomeric materials, they are adequate as insulation materials for solid rocket motors [15,16]. Elastomers are linear polymers, though most of them form no solid carbonic residue under thermal decomposition and will form a melt film only in the presence of specific additives. Thus, fillers play an important role in providing the necessary erosion resistance, heat shielding properties, and mechanical strength. Introduction of various fillers can change the physical, mechanical, rheological, and other properties of these elastomeric materials [15-17]. Engineered thermoplastic elastomer (ETPE), products like

Santoprene® thermoplastic rubber is already demonstrating their performance capability to replace EPDM in automotive weather seal applications [18]. An excellent cost/performance balance, a potential weight reduction, coloring options and co-extrusion with rigid thermoplastic materials are the key advantages versus classical EPDM thermoset rubber profile systems [18,19].

2. TECHNICAL PROGRAM SUMMARY

2.1 First Year Highlights and Accomplishments

For the first year (June 2006 to Sept. 2007) of this research grant, we made significant progress in the project's two major areas: modeling and experimental [20,21].

Modeling

We focused on understanding the current state-of-the-art of ablation models. Specifically, we have examined polymer degradation kinetics, conduction in an ablating solid, and the continuum equations used by thermochemical ablation codes such as CMA and Hero2D. A particular emphasis had been placed on identifying the dominant mechanisms of ablative performance. The following is a summary of our progress made towards ablation modeling:

- Literature review and critical evaluation of simple ablating solid (Stefan problem) models

- Analysis of ablation from a design perspective including (a) computed failure time for simple 1-D slab of phenolic-based ablative materials such as MXBE-350 and H41N, (b) determined analytical sensitivities of failure time to thermophysical properties of materials, and (c) used optimization to map the material design space for these simple models and identify an "optimal" ablative

- Literature review and critical evaluation of the continuum energy, mass, and momentum equations used by ablation modeling codes such as CMA and Hero2D

- Used CMA to predict temperature profile evolution of ablating carbon phenolic, and studied the sensitivity of the maximum back-wall temperature to various thermophysical properties

- Developed a population balance (meso-scale) model for polymer scission and transport in a slab. This model was developed to improve the kinetic description of polymer degradation under high heat flux loading (high heating rate) conditions.

Experimental

TGA were conducted in both air and nitrogen on all formulations of TPU, TPUN-clay, and TPUN-carbon nanofiber to study their thermal stabilities at low heating rates (5 to 150K/min). TGA in nitrogen experiments were used for kinetic parameter calculations. A thorough literature search was conducted on kinetic parameter derivation, including the differential method, which was developed in the 60's and the isoconversion method, which is a more recent approach. The differential method was verified using TGA data from Henderson *et al.*, on glass-filled phenolic ablatives (MXBE-350 and MXB-360).

The isoconversion method was verified by conducting TGA on pure PMMA. Kinetics calculations for the TPU and TPUNs were completed using the isoconversion method. TPUN materials were prepared for DSC (specific heat and heat of decomposition), laser flash diffusivity (thermal diffusivity and thermal conductivity), and dilatometry (coefficient of thermal expansion). Virgin TPUN materials are ready. Pre-charring of the TPUNs was done using vacuum furnace and argon-purging oven, but none of the methods were successful in duplicating the same state of the material similar to TPUN exposed to solid rocket motor firing. Study on using the simulated solid rocket motor facility for charring the TPUN material is in progress. Designing of an eroding "Self-Renewing" multifunctional senor made of TPUN materials is in progress with NANMAC Corp. Extra fine thermocouples are placed at the surface and at specified distance away from the surface. These sensors allow us to estimate ablation rate and measure thermal data through the TPUN materials for model verification and validation.

In summary, we presented/published 8 papers during this reporting period (June 1 2006 to Sept. 30, 2007).

2.2 Second Year Highlights and Accomplishments

For the second year (Oct. 2007 to Sept. 2008) of this research grant, we made significant progress in the project's two major areas: modeling and experimental [22].

Modeling

We focused on developing population balance equation (PBE) models of thermoplastic degradation. We also simulated carbon phenolic for the atmospheric re-entry problem using thermochemical ablation codes such as CMA87S (finite difference 1-D ablation code) and Chaleur (control volume finite 1-D ablation code). The following list is a summary of the progress made towards modeling of ablation.

- Studied the effect of changing carbon filler composition on total mass loss rate; compared mass loss rate to net heat transfer to surface to determine an effective heat of ablation using CMA87S code

- Developed PBE models of thermoplastic degradation for purely random chain scission and for three-step radical depolymerization mechanism

- Solved random scission model analytically for isothermal degradation

- Solved both PBE models: either directly using modified sectional method *or* an approximate moment method

    - Method is analytically closed for random chain scission model

    - Used quadrature method of moments (QMOM) for radical depolymerization model

- Used optimization to find model parameters for PBE and global Arrhenius models using different algorithms: (a) Nelder-Meade simplex, (b) Genetic, and (c) Sequential quadratic programming

Experimental

A family of new thermoplastic polyurethane elastomer nanocomposites (TPUNs) based on various loadings of nanoclay, carbon nanofiber (CNF), and multiwall carbon nanotube (MWNT) were developed to replace the state-of-the-art solid rocket motor insulation Kevlar-EPDM material. The following summarizes the progress made towards the characterization of this family of TPUNs:

- Conducted TGA experiments using low heating rates (10 to 100°C/min) for neat TPU (Desmopan® 6065A), TPUN-clay, and TPUN-MWNT of various loadings from 2.5 to 10wt%; TPU-CNF TGA experiments of various loadings from 5 to 20 wt% are in progress

- Initiated high heating rate (up to $1,000^{\circ}$C/min) TGA experiments at Sandia using TPUN-5wt% nanoclay to examine if the kinetics will be different from low heating rate TGA data, other TPUN-MWNT and TPUN-CNF composites will be tested; PBE models using optimization techniques will be used to analyze these TGA data

- Performed flammability studies on neat TPU, TPUN-clay, and TPUN-MWNT using UL 94 test method; specimens were burnt at different degrees and were examined under SEM

- Flame tests revealed the neat TPU burns and drips and the TPUN-5 wt% nanoclay specimen formed a tougher char than the TPUN-MWNT specimen

In summary, we presented/published 13 papers during this reporting period (Oct. 1 2007 to Sept. 30, 2008).

3. DISCUSSION OF RESULTS

This final report summarizes last 12 months of our research progress during the period of Oct. 1, 2008 to Sept. 30, 2009. This section will be divided into three sub-sections: (3.1) Experimental progress, (3.2) Numerical progress, and (3.3) Publications and presentations.

3.1 Experimental Progress

In this section, we will discuss the following: (3.1.1) Material systems used, (3.1.2) Measurements used to characterize specific properties of the materials, (3.1.3) Processing and dispersion characterization of polymer nanocomposites (PNCs), (3.1.4) Physical properties, (3.1.5) Thermogravimetric analyses and kinetics calculations, (3.1.6) Flammability testing and analyses, (3.1.7) Flammability and physical property correlation, and (3.1.8) Eroding thermocouple gauges.

3.1.1 Material Systems

A. Polymer Resin

Thermoplastic elastomer (TPE) is a family of rubber-like materials that can be processed and recycled like thermoplastic materials, unlike conventional vulcanized rubbers which can't be recyclable and requires cross-linking. In the first year of this research program, Pellethane$^{\text{TM}}$ 2102-90A [23] was selected for investigation. This is a thermoplastic polyurethane elastomer (TPU) material manufactured by Dow Plastics and

has the following properties: outstanding abrasion resistance, good low temperature flexibility and impact resistance, good resistance to fuels, oils, and most non-polar solvents, good hydrolytic stability, range of hardness, transparency, low compression set, high compressive strength, low gas/vapor permeability, relatively high moisture vapor transmission rates, easy processibility with conventional extrusion and thermoplastic molding techniques, and low extractable levels.

In the second year of this research program a new TPU, Desmopan™ DP 6065A [24] manufactured by Bayer MaterialScience was selected. Desmopan™ DP 6065A is much softer than the previously tested Dow TPU, Pellethane™ 2102-90A. Both materials are compounded into 4" cross section square panels, as shown in Figure 3.1. A type A durometer is used to test the shore hardness on two stacked 1/8" thick panels as specified under ASTM-2240. The measured Pellethane™ shore hardness, 95A, closely matches that listed in the material data sheet, 94A. The measured shore hardness of Desmopan™ which ranges from 67A to 70A is a bit higher than the listed hardness, 65A. The material at the center of the panel was found to be softer than that at the edges.
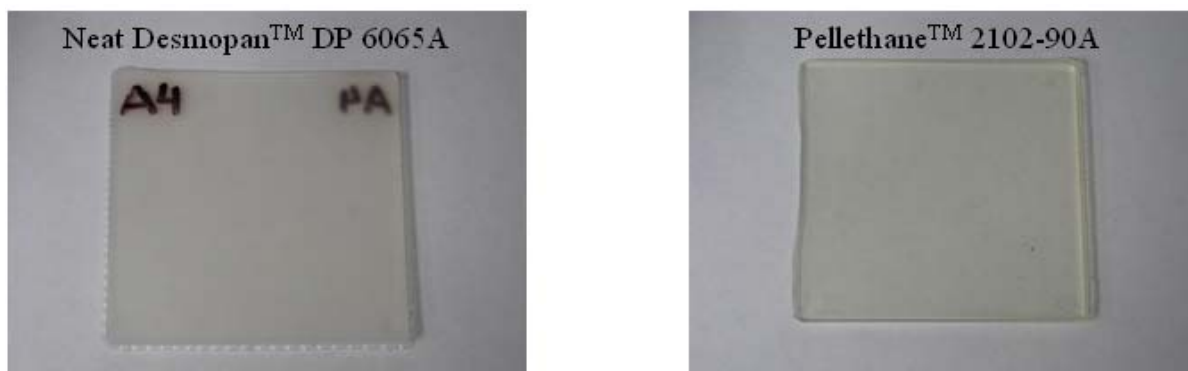
Figure 3.1 Neat thermoplastic polyurethane elastomers – Desmopan™ DP 6065A (left) and Pellethane™ 2101-90A (right).

Desmopan® DP 6065A [24] is an aromatic polyether-based thermoplastic polyurethane elastomer (TPU) manufactured by Bayer MaterialScience. It can be processed by injection molding. It is characterized by good hydrolysis and microbe resistant, short cycle times, and is plasticizer free. Typical applications include rigid/flexible composite systems and sport shoe soles. Material properties of Desmopan® DP 6065A are listed in Table 3.1 [24].

TABLE 3.1 Material Properties of Desmopan® DP 6065A

Typical Properties, (US Units, SI Metric Units)	Values
General	
Specific Gravity	1.09
Hardness (Shore A)	65A
Taber Abrasion, H-18 wheel, 1000-g load, 1000 cycles, mg Loss	76
Bayshore Resilience, %	49
Mold Shrinkage @ 100-mil thickness: Flow direction/Cross-Flow	0.008/0.008

direction, in/in, mm/mm

Mechanical	
Tensile Strength (psi, MPa)	1790, 12.3
Tensile Stress at 100% elongation, (psi, MPa)	380, 2.6
Tensile Stress at 300% elongation, (psi, MPa)	610, 4.2
Ultimate Elongation, %	890
Tear Strength, (Die C), (psi, kN/m)	290, 50.9
Flexural Modulus @ 23°C/@ -30°C, (psi, MPa)	1440, 9.9/2400, 16.6
Compression Set, % (22 hrs. @70°C/22 hrs. @23°C)	34, 12
Thermal	
Vicat Softening Temperature (Rate A), (°F, °C)	133, 56
Glass Transition Temperature (DMA) , (°F, °C)	-49, -45

B. Nanoparticles

Three types of nanoparticles were used in this study. They are Southern Clay Products' Cloisite® 30B nanoclay, Arkema's Graphistrength® C100 multiwall carbon nanotubes, and Applied Sciences' Pyrograf® III PR-19-XT LHT CNF. They will be briefly described in the following.

B.1 Montmorillonite (MMT) Nanoclays

Montmorillonite nanoclay is a widely investigated nanoparticle, most commonly formed by in-situ alteration of volcanic ash. Its sheet structure consists of layers containing the tetrahedral silicate layer and the octahedral alumina layer. Each sheet of MMT nanoclay has thickness of approximately 0.96 nm. MMT nanoclays are able to improve mechanical properties, barrier performance, and application processing when full exfoliation is achieved in a polymeric material. In order to achieve exfoliation in various continuous phases, surface treatment of the nanoclay is needed. The MMT nanoclay of choice in this project is the Cloisite® 30B, which is a surface-treated montmorillonite manufactured by Southern Clay Products [25,26]. Cloisite® additives allow complete dispersibility and miscibility with many different resin systems. Surface treatment is accomplished with ion exchange between inorganic alkali cations on the clay surface with the desired organic cation. In this case, quaternary ammonium ions are chosen, and they act as a compatibilizing agent between the interface of MMT nanoclay and the continuous phase of the TPU. Specific chemical pre-treatment modifier (MT2EtOH: methyl, tallow, bis-2-hydroxyethyl, quaternary ammonium) is used for the preparation of Cloisite® 30B.

B.2 Multiwall Carbon Nanotubes (MWNTs)

Arkema produces multiwall carbon nanotubes (CNTs) under the trade name Graphistrength®. Process is chemical vapor deposition at elevated temperature of ethylene on metal/ceramic catalyst. Arkema produces CNT's (Graphistrength® C100) and CNT-containing products. Plain CNTs exist in bundles with median diameter approximately 10 to 20 μm. Typical dimensions are 10 to 15 nm in diameter corresponding to approximately 5 to 15 concentric tubes, with lengths approximately 1 to 10 μm [25,27]. Graphistrength® C100 is used in this study.

B.3 Carbon Nanofibers (CNFs)

Carbon nanofibers (CNFs) are a form of vapor-grown carbon fiber, which is a discontinuous graphitic filament produced in the gas phase from the pyrolysis of hydrocarbons. CNFs are able to combine many of the advantages of these other forms of carbon for reinforcement in engineered polymers. CNFs also have transport and mechanical properties that approach the theoretical values of single crystal graphite but can be made in high volumes at low cost. The CNFs are manufactured by Applied Sciences Inc./Pyrograf[®] Products by pyrolytic decomposition of methane in the presence of iron-based catalyst particles at temperatures above 900°C. CNFs are produced only in a discontinuous form, where the length of the fiber can be varied from about 100μm to several cm, and the diameter is of the order of 100 nanometers. The CNFs used in the study are PR-19-XT LHT CNF [25,28]. The abbreviation LHT denotes that the carbon nanofibers are low heat treated CNFs. PR-19-PS CNF has fiber diameters of 100 to 200nm and fiber lengths of 30 to 100μm.

3.1.2 Measurements

A. Test Plan for TPUN

A thorough three phases test plan was developed during our 2nd year study. This test plan was aimed toward full characterization of the newly developed TPUN materials. In general the following properties will be characterized for the new TPUN materials using ASTM or industry standard test methods that are grouped in the following properties [22]:

- Ablation
- Flammability
- Mechanical
- Microstructural
- Physical
- Thermal

B. Ablation Test

Five types of tests will be performed on the new TPUN materials to simulate solid rocket motor environment, namely (a) Low heat flux radiant panel, (b) High heat flux Simulated Solid Rocket Motor (SSRM), (c) High heat flux LHMEL, (d) High heat flux Pi-K motor, and (e) High heat flux Bates motor.

B.1 Radiant Panel Test

TPUN samples of 4- by 4- by 1/8-inches will be tested using a radiant panel, Figure 3.2. The samples will be tested at low heat flux between 50 and 90 kW/m^2 and the front and backside temperatures will be measured. These experiments will be able to provide us detailed thermal data on the behavior of these TPUN materials.

Figure 3.2 Radiant panel set up.

B.2 Simulated Solid Rocket Motor Test

The simulated solid rocket motor (SSRM) at Texas State University-San Marcos will be used (Figure 3.3). The SSRM can provide a heat source up to 14 MW/m^2 by using a liquid rocket motor fueled by kerosene. In addition to a higher heat flux, the SSRM has a hopper containing alumina particles when entrained into the rocket exhaust plume will be ejected at 2,000 m/s. These alumina particles simulate those observed in solid rocket motor environments. An IR pyrometer will measure the surface temperature of the test article while a thermocouple will be placed on the back to measure backside heat-soaked temperature. Since the high heat flux as well as impinging Al_2O_3 particles will erode the material significantly, the test will use a 1/2" specimen and the test duration will be set to about 15 seconds. Post-test analyses including peak erosion measurements, surface and backside heat-soaked temperatures, and microstructural analyses of post-test specimens using SEM will be conducted for each TPUN materials to evaluate their performance.

Figure 3.3 Texas State University-San Marcos simulated solid rocket motor.

B.3 Laser Hardened Materials Evaluation Laboratory Test

The third rocket test environment will be performed at the Laser Hardened Materials Evaluation Laboratory (LHMEL) located at the Wright-Patterson AFB. The LHMEL I

facility has a CO_2 laser with a spot size of ½" to 24" (Figure 3.4). It provides between 300 to 10,000 W, a sufficiently high heat flux. The Pellethane[TM] PNCs fitted with the NANMAC gauges will be tested at this facility. The material will ablate, and these gauges can be tested. From the SSRM tests, a number of Desmopan[TM] formulations will also be tested. Additional real time data can be obtained using the facilities X-ray machine which will be fixed above the sample that is exposed to the laser source.
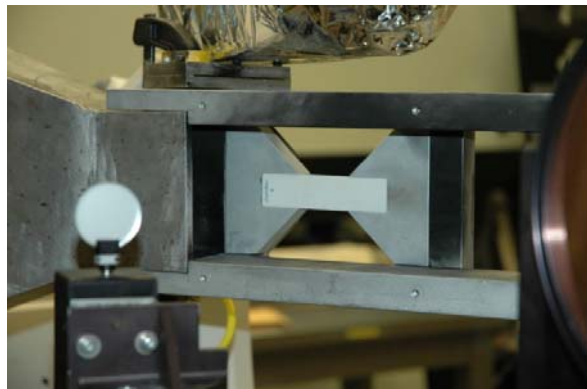
Figure 3.4 Laser Hardened Materials Evaluation Laboratory test setup.

B.4 Pi-K and Bates Motor Firings

In addition to the three mentioned low and high heat flux tests, AFRL-Edwards has set up two small scale SRMs for ablation testing of insulation materials. The two motors are a Pi-K motor (Figure 3.5) and a Bates motor (Figure 3.5). In both test setups, the insulation materials are placed on a cylindrical glass phenolic cone. The cone shape allows different parts of the insulation to see the combustion exhaust products for both aluminized and non-aluminized propellants at different cross-sectional areas. These varying cross-sectional areas relate directly to varying Mach numbers. This allows a range of data to be obtained using one test run. For direct comparison of a candidate material to a reference material can be simultaneously tested. The glass phenolic cone cross-section of the Pi-K and Bates motor is divided into 4 quadrants. The first and third quadrants will hold the test insulation material and the second and fourth quadrants will hold the reference material. The materials are placed along diagonal quadrants in order to avoid any bias in the flow. The reference material used will be the Kevlar-filled EPDM rubber.
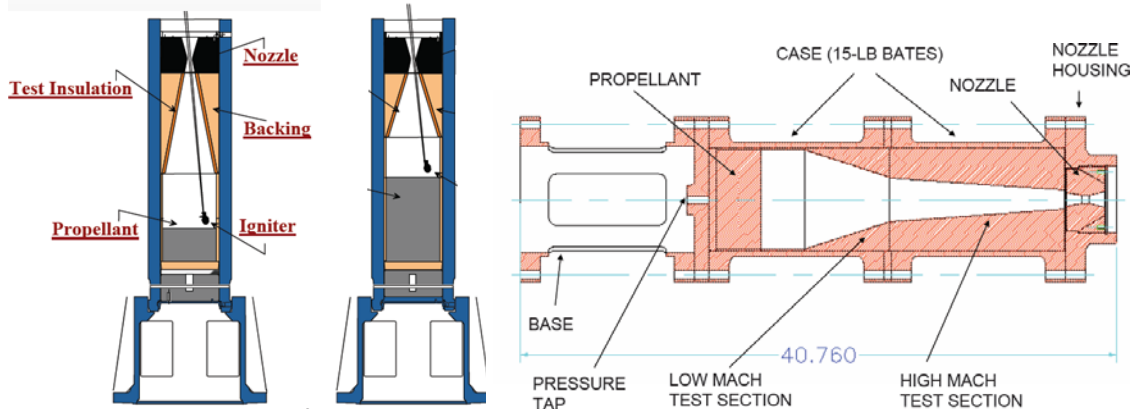
Figure 3.5 AFRL Pi-K motor (left) and Bates motor (right).

C. Flammability Properties Measurements

A standard flammability test performed on polymers is the UL 94 test [29]. Of the three types of UL 94 test setups: surface burn, vertical burn, and horizontal burn tests; the vertical burn test was run on the Desmopan® nanocomposite formulations. A 1" flame is placed at 45° to the bottom of a clamped 5" x 0.5" x 0.125" test specimen, Figure 3.6. After 10 seconds the flame is removed and the time the specimen remains on fire is recorded. A second 10 second flame is introduced and the time of burn after removal is again recorded. The specimen is held 12" above a piece of cotton. The cotton is used to determine the flammability of any drip from the material. Based on these observations the specimen can either pass or fail V0, V1 or V2.
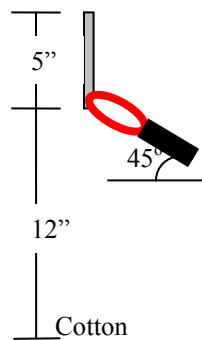
Figure 3.6 Vertical burn UL 94 test setup.

V0 is the most stringent of the three. The specimen must not burn for more than 10 seconds and is not allowed to drip and ignite the cotton. V1 allows up to a 30 second burn but still restricts drip that ignites the cotton. V2 also allows less than 30 second burn time however allows drip that ignites the cotton.

D. Mechanical Properties Measurements

A list of mechanical properties including tensile strength, tensile stress @ 100% elongation, tensile stress @ 300% elongation, ultimate elongation, Young's modulus, flexural modulus, as well as DMA data will be obtained for all TPUN materials.

E. Microstructural Characterization

To characterize nanoparticle dispersion, the cross-sections of the TPUNs were examined by TEM to determine the degree of dispersion of nanoclay/carbon nanofibers within the TPU polymer matrix. Uniform distribution of the nanoparticles within the polymer matrix is essential to yield the best enhancement of material properties of the polymer matrix. Luo and Koo developed a general method to quantify the dispersion of nanoparticles in polymer matrices using TEM analyses [30-32]. A new methodology was developed to determine the dispersion parameter, $D_{0.1}$, based on the measurement of the free-path spacing distance between the single clay sheets and CNFs from the TEM images. This methodology will be adapted in this study. Microstructural analyses of post-test specimens from ablation and fractural tests were examined using SEM to understand the material behavior of these TPUNs.

F. Physical Properties Measurements

Physical properties of TPU and TPUNs such as specific gravity and shore hardness were evaluated.

G. Thermal Properties Measurements

Thermal properties of TPU and TPUNs were evaluated. Heat deflection temperature (HDT) and coefficient of thermal expansion (CTE) were measured. Specific heat capacity measurement was performed using a differential scanning calorimeter (DSC). Thermal diffusivity measurement was performed using a laser flash. Thermal conductivity was calculated using data from density, heat capacity, and thermal diffusivity measurements. TGA data were used to determine the kinetic parameters of selected TPUNs using the isoconversion technique.

3.1.3 Processing and Dispersion Characterization of Polymer Nanocomposites

A. Blending and Characterization of Nanoclay/CNF in Pellethane™ TPU

Twin-screw extrusion technique was used for blending the different types of nanoparticles in the TPUs. In our 1st year study, Pellethane™ 2102-90A TPU with different loading levels of Cloisite® 30B nanoclay and PR-19-PS CNF were compounded. The TPUN formulations, baseline EPDM, and pure TPU are listed in Table 3.2.

TABLE 3.2 Material Matrix for Pellethane™ 2101-90A TPU Nanocomposites

Formulation	Polymer matrix, wt%	Filler, wt%
1	EPDM (88%)	12% Kevlar®
2	2102-90A (100%)	None
3	2102-90A (97.5%)	2.5% Cloisite® 30B nanoclay
4	2102-90A (95%)	5% Cloisite® 30B nanoclay
5	2102-90A (92.5%)	7.5% Cloisite® 30B nanoclay
6	2102-90A (90%)	10% Cloisite® 30B nanoclay
7	2102-90A (95%)	5% PR-19-PS CNF
8	2102-90A (90%)	10% PR-19-PS CNF
9	2102-90A (85%)	15% PR-19-PS CNF

10	2102-90A (80%)	20% PR-19-PS CNF

Selected TPU blends with the baseline Kevlar®-filled EPDM were tested using the AFRL char motor with aluminized propellants for ablation. The 5% Cloisite® 30B and 15% PR-19-PS CNF TPUNs ranked highest in terms of ablation resistance and mechanical properties for their respective family of nanoparticles, thus chosen for detailed thermophysical properties characterizations. Transmission electron microscopy (TEM) analyses were conducted on the 15% PR-19-PS CNF TPUN, and the micrographs show uniform dispersion of CNFs in 2102-90A TPU, as depicted in Figure 3.7, showing magnification from 500 to 100nm scale bar. CNFs of approximately 100nm in diameter were fully dispersed in the polymer, forming TPU nanocomposites. In addition to TEM, the 5% Cloisite® 30B TPUN was also analyzed using wide-angle X-ray diffraction (WAXD) for dispersion, shown in Figure 3.8. No peaks were observed in WAXD, which indicated the nanoclays were exfoliated in the TPU polymer, and TEM micrographs, in Figure 3.9 showing magnification from 500 to 100nm scale bar, confirmed that the Cloisite® 30B nanoclay achieved intercalation/exfoliation in the polymer matrix.
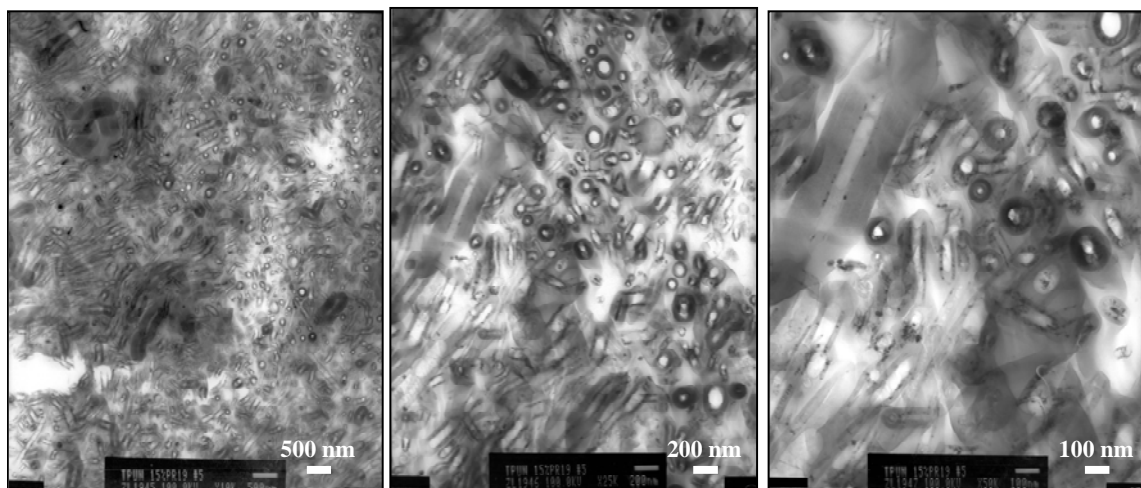
Figure 3.7 Transmission electron micrographs of 15% PR-19-PS CNF TPUN.
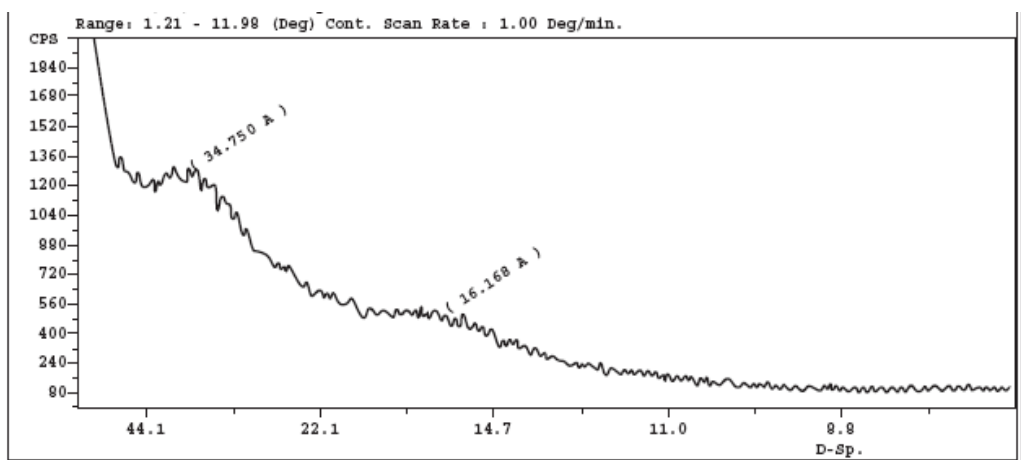
Figure 3.8 Wide-angle X-ray diffraction of 5% Cloisite® 30B nanoclay TPUN.
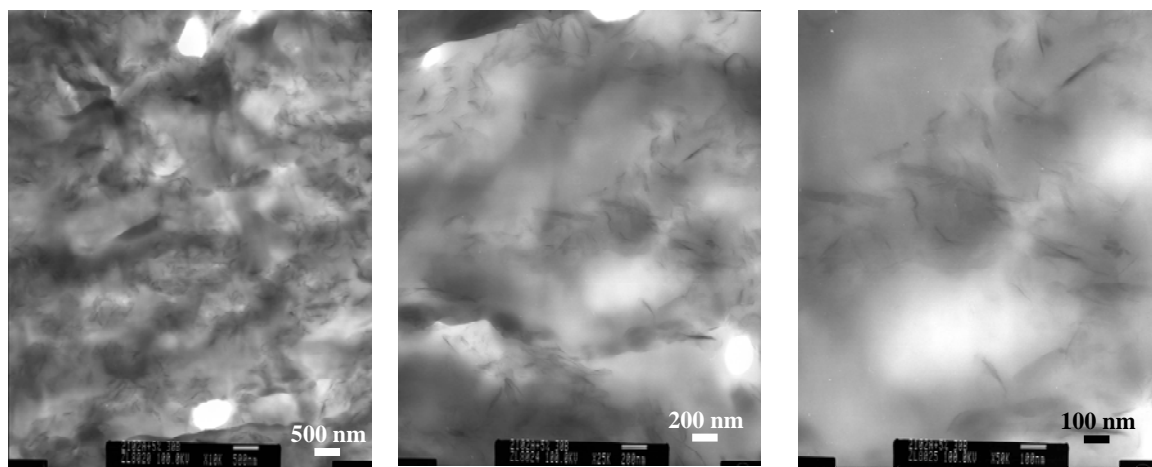
Figure 3.9 Transmission electron micrographs of 5% Cloisite® 30B nanoclay TPUN.

B. Blending and Characterization of Nanoclay/CNF/MWNT in Desmopan™ TPU

In our 2nd year study, Desmopan™ DP 6065A TPU with different loading levels of Cloisite® 30B nanoclay, Graphistrength™ C100 MWNT, and PR-19-XT LHT CNF were compounded. The TPUN formulations, baseline EPDM, and pure TPU are listed in Table 3.3.

TABLE 3.3 Material Matrix for Desmopan^TM DP 6065A TPU Nanocomposites

Formulation	Polymer matrix, wt%	Filler, wt%
1	Desmopan^TM DP 6065A (100%)	None
2	Desmopan^TM DP 6065A (97.5%)	2.5% Cloisite® 30B nanoclay
3	Desmopan^TM DP 6065A (95%)	5% Cloisite® 30B nanoclay
4	Desmopan^TM DP 6065A (92.5%)	7.5% Cloisite® 30B nanoclay
5	Desmopan^TM DP 6065A (90%)	10% Cloisite® 30B nanoclay
6	Desmopan^TM DP 6065A (97.5%)	2.5% C100 MWNT

7	Desmopan^{TM} DP 6065A (95%)	5% C100 MWNT
8	Desmopan^{TM} DP 6065A (92.5%)	7.5% C100 MWNT
9	Desmopan^{TM} DP 6065A (90%)	10% C100 WNT
10	Desmopan^{TM} DP 6065A (95%)	5% PR-19-XT-LHT CNF
11	Desmopan^{TM} DP 6065A (90%)	10% PR-19-XT-LHT CNF
12	Desmopan^{TM} DP 6065A (85%)	15% PR-19-XT-LHT CNF
13	Desmopan^{TM} DP 6065A (80%)	20% PR-19-XT-LHT CNF

Nanoclay is supplied in stacks of platelets between 2-13 μm. When mixed with the polymer the platelets are broken up into nanoparticle size. In our 1st year study, Pellethane^{TM} TPU was also tested with Cloisite$^{®}$ 30B, however a different CNF was used for our 2nd year study. For our 1st year study, we used the PR-19-XT-PS which is a pyrolytically stripped CNF. The production of this CNF will be discontinued shortly, replaced by the PR-19-XT-LHT, a low heat treated, 1,500^{o}C, CNF. The heat treatment is expected to produce better performance CNFs because it removes carbons that were on the CNF surface.

The size of the nanoparticles have a large influence on how they will perform, traditional carbon fibers have diameters between 5-10 μm whereas the CNFs have a diameter of 150 nm. Even smaller are the 5 -15 nm diameter MWNTs. Because of its small size although the MWNTs were not tested with Pellethane^{TM} they are expected to perform as well or better than the CNF samples. The MWNT and Cloisite$^{®}$ 30B Desmopan^{TM} families have been processed and the performed tests are described in this report. The 2.5wt% and 10wt% of both MWNT and Cloisite$^{®}$ 30B Desmopan^{TM} samples are shown in Figure 3.10. Note the increase in opaque pigment as more Cloisite$^{®}$ 30B is added in contrast with the MWNT family, where a small amount of MWNTs gives the polymer a dark black pigment.
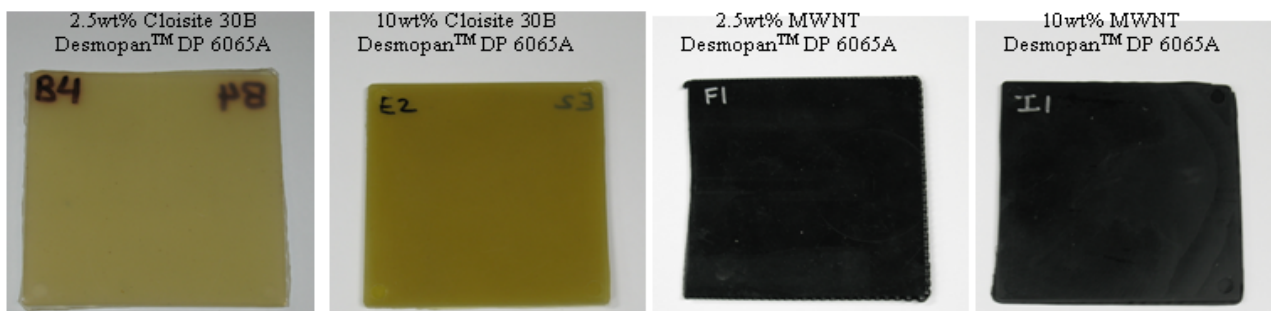
Figure 3.10 Desmopan^{TM} DP 6065A with 2.5wt% and 10wt% Cloisite$^{®}$ 30B and MWNT.

The TPU polymer arrives in pellet form. In order for quality polymer nanocomposite formulations to be created, proper heat treatment and shear of the mixture must be applied. All processing was conducted by 21st Century Polymer. Two steps are involved in processing the material into samples that can be used for testing. First, the neat polymer must be well mixed with the selected nanoparticle and formed into polymer

nanocomposite pellets of the desired formulation. The pellets are then re-melted and injection molded into specimens of specific size and shape.

In the beginning, only the neat material is run through the system to flush the machine out of old samples. A regulator controls the amount of nanoparticle that is released. This precise control is used to dictate which formulation is created since the amount of neat polymer released can also be controlled. As shown in Figure 3.11, the Desmopan™ pellets are dropped into the twin screw extruder and melted before the incorporation of nanoparticles, this allows the nanoparticles to infuse into a melted polymer for better mixing.

Figure 3.11 21st Century Polymer twin screw extruder setup.

Each heating element is independently controlled, allowing the temperature within each individual zone to be set accurately. In addition, the screws on the twin screw extruder are not of one design. Rather, multiple sections of smaller screws are stacked in each heating zone, as shown in Figure 3.12. Each screw has a different design, allowing control of both the mixing and flow rate. Some screws are used to push material through quickly, others are used to hold the material for longer mixing, and some are used for quick mixing in a short period of time. The screw design are pre-determined based on the type of nanoparticles. The quality of these polymer blends is determined by examining the dispersion; the results are shown in the next section.

Figure 3.12 Screw sections of twin screw extruder.

   After the polymer nanocomposite flows through the twin screw extruder, the material is pushed out in the form of 2 spaghetti strips which are pulled through a water bath, Figure 3.13(a). The spaghetti is than sent into a machine which cuts it into pellets, Figures 3.13(b) and 3.13(c). The pellets are injection molded into the desired test shape. Because during injection molding no mixing is performed, a simple set of screws is needed simply to push the material across the heating elements.

Figure 3.13 (a) - (c) (a) Water bath, (b) Machine used to cut polymer spaghetti into pellets, and (c) PNC pellets.

   One of the test samples that is produced from this process are the 4" cross section square panels shown earlier. The specimens that come out of the injection mold are 1/8" thick, however many of tests require specimens to be ½" to 1" thick. Compression molds were attempted to avoid purchasing a larger injection-mold. For very thick samples, stacks of 1/8" panels were placed in a furnace at a temperature just below melt to get a more uniform temperature profile before compression molding the specimen.

   Certain material properties enhancement will not fully be achieved if the nanoparticles are not well dispersed within the polymer. Examination of this is done using transmission electron microscopy (TEM). Figure 3.14 is a 10 kX image of the Desmopan-Cloisite[®] 30B formulations, with a 0.2 µm scale bar. PNCs containing Cloisite[®] 30B are classified under 3 categories: unmixed if the nanoclay platelets are packed tightly together, intercalated if the platelet stacks are open but still grouped, and exfoliated if each nanoclay platelets appears independent of the each other. No stacks are

observed in any of the three 40 kX images in Figure 3.15, scale bar is 100 nm. The lack of platelet stacks indicates that the material is exfoliated and well dispersed.
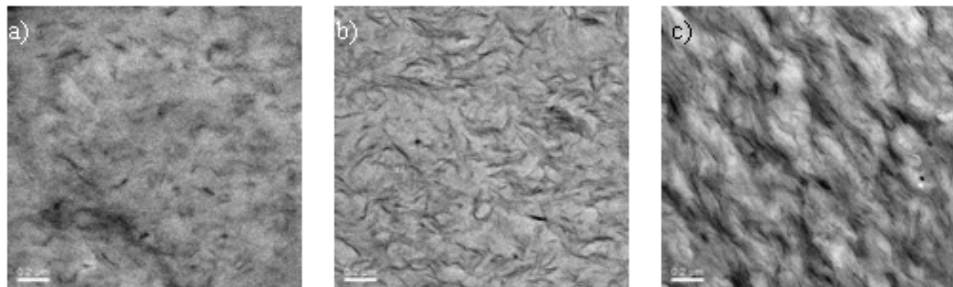
Figure 3.14 TEM at 10 kX of (a) 2.5% (b) 5% (c) 10% Desmopan^{TM} Cloisite$^®$ 30B.
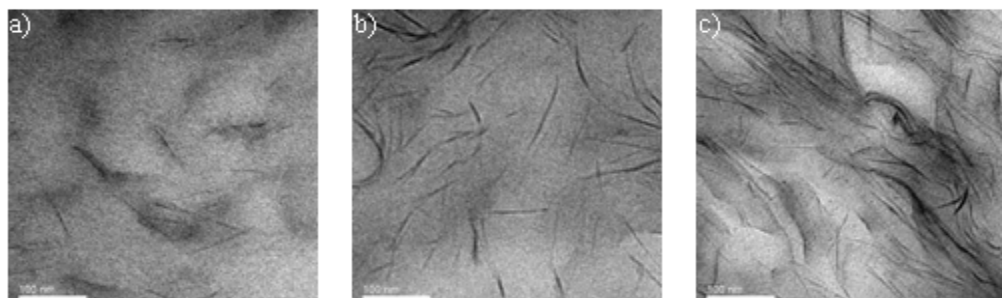
Figure 3.15 TEM at 40 kX of (a) 2.5% (b) 5% (c) 10 % Desmopan^{TM} Cloisite$^®$ 30B.

Identical TEM images were taken for the Desmopan-MWNT formulations. The 10 kX (unit scale is 0.2 μm) and 40 kX (unit scale is 100 nm) images are shown in Figures 3.16 and 3.17, respectively. When the MWNTs are purchased they come in bundle form. Similar to the stacked nanoclay platelets, the MWNT bundles must be unbundled to be considered well dispersed. The 40 kX images in Figure 3.17 clearly show that the MWNTs are unbundled. If bundles were present, there would be areas with no MWNTs and areas with a high density MWNTs. Since this is not observed, the MWNT PNCs are considered well dispersed. The lack of order in both nanoparticle orientation and the uniform dispersion show that these two families of polymer nanocomposites were processed well. The full enhancement to material performance that can be obtained from these nanofillers is expected.
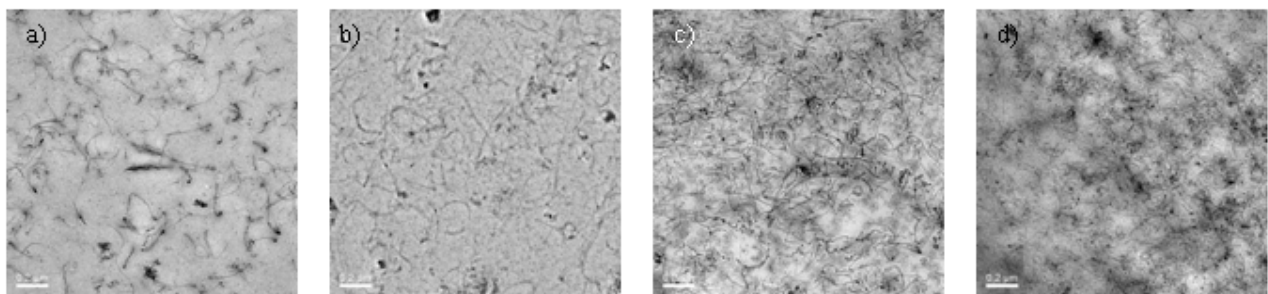
Figure 3.16 TEM at 10 kX of (a) 2.5% (b) 5% (c) 7.5% (d) 10% Desmopan^{TM} MWNT where unit scale is 0.2 μm.
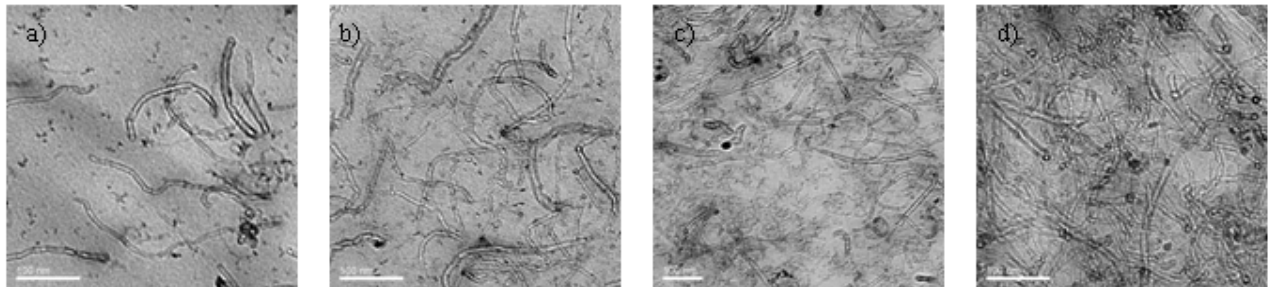
Figure 3.17 TEM at 40 kX of (a) 2.5% (b) 5% (c) 7.5% (d) 10% Desmopan^{TM} MWNT where unit scale is 100nm.

3.1.4 Physical Properties

The specific gravity of the Desmopan 6065A-clay and Desmopan 6065A-MWNT nanocomposites are shown in Figure 3.18. Desmopan 6065A-clay nanocomposites have high specific gravity than the Desmopan 6065A-MWNT nanocomposites at the same wt% loading for nanoparticles. The nanocomposite specific gravity also increases with the wt% loading.
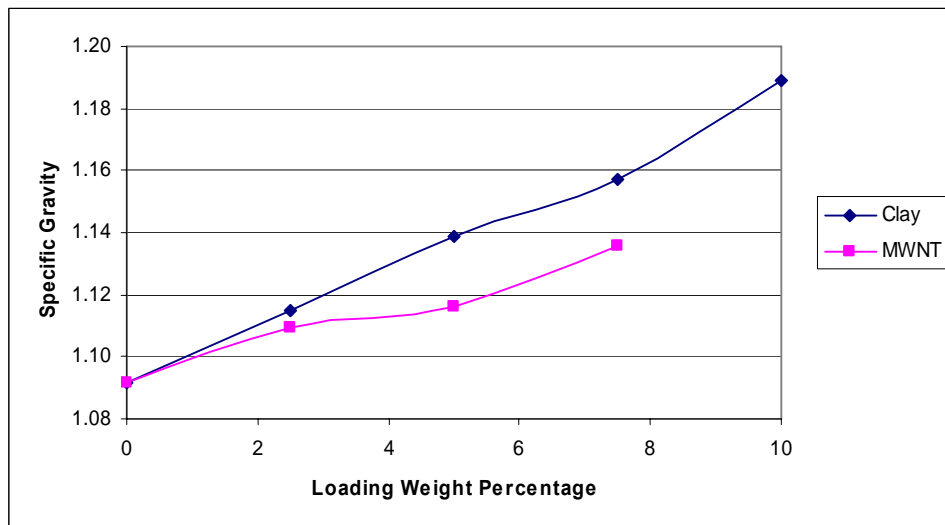
Figure 3.18 Desmopan^{TM} 6065A nanocomposite specific gravity.

The addition of nanoparticles stiffens the polymer. The observed hardness changes are shown in Figure 3.19. Cloisite$^{®}$ 30B increases the polymer stiffness more dramatically than the MWNT. CNF data will be reported later in section 3.1.6.

Shore Hardness A of Desmopan 6065A Nanocomposite
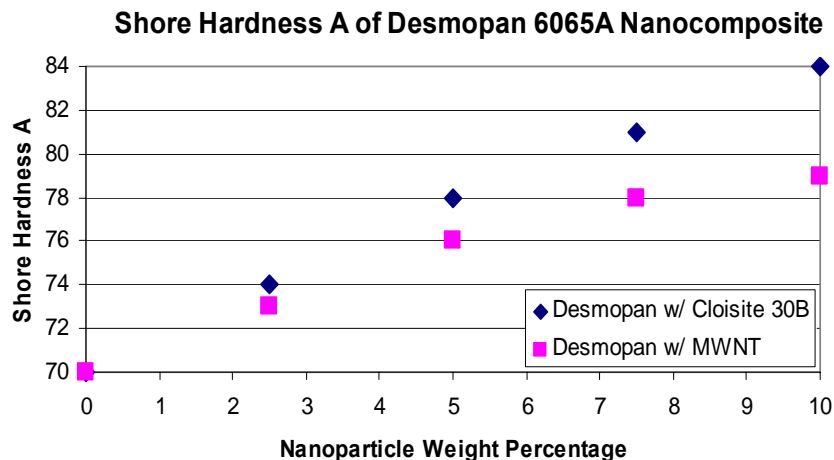
Figure 3.19 Desmopan™ 6065A nanocomposite hardness.

3.1.5 Thermogravimetric Analyses and Kinetics Calculations

A. Experimental Method

The required data for calculating the kinetic parameters by TGA are temperature, weight loss, and the rate of weight loss. These data are obtained with a Perkin Elmer Model TGA7 thermogravimetric analyzer, shown in Figure 3.20. It has a vertical design with a high sensitivity microbalance and electric platinum wound furnace, which is capable of heating rates up to 180°C/min to a maximum temperature of 1,000°C. The microbalance is located above the furnace and is thermally isolated from it. A hang-down wire is suspended from the balance down into the furnace. At end of the hang-down wire is the platinum sample pan. The sample temperature is measured with a chromel-alumel thermocouple located inside the furnace. The purging gas flow rate is regulated by a mass flow controller and is kept at 20 ml/min.
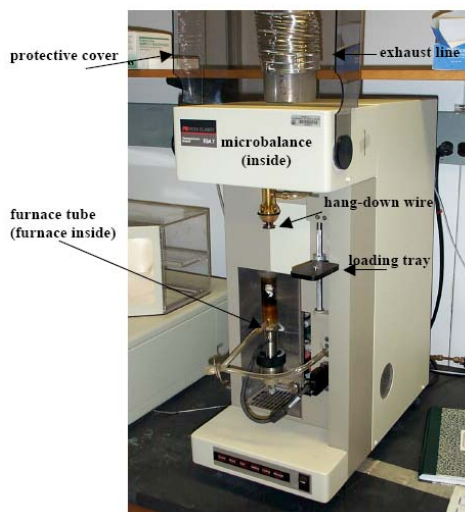
Figure 3.20 Perkin-Elmer TGA7 thermogravimetric analyzer and its components.

B. Calibration

Because the thermocouple and sample pan are physically separated, the indicated and actual sample temperatures differ. Temperature calibration as well as baseline run is required each time when the heating rate is changed. The temperature calibration is performed according to the Curie point of magnetic materials. Curie point is the temperature at which a ferromagnetic material becomes paramagnetic; due to thermal energy, the dipoles cannot line up as they can in the ferromagnetic state. Four reference materials such as alumel, nickel, perkalloy, and iron are used to perform a calibration across the usable temperature range (100-900°C). A magnet is placed beneath the tared samples to create weight. The material is heated and as it loses magnetism at its Curie point, the weight disappears since it no longer responds to the magnet. If the temperature correction at any Curie point is more than ±2°C, the limits on the temperature control unit is changed, and this Curie calibration is repeated. Furnace calibration is also performed in accordance to the user manual. A baseline run will be the same procedure as a sample run except with an empty sample pan.

C. General Description of Kinetic Rate Equation

The rate of decomposition of a material can be modeled by the kinetic rate equation,

$$-\frac{1}{w_0}\frac{dw}{dt} = Af\left(\frac{w}{w_0}\right)^n \exp\left(-\frac{E}{RT}\right), \tag{1}$$

where A is the pre-exponential factor, E is the activation energy, n is the order of reaction, and $f(w/w_0)$ is an arbitrary function of instantaneous weight fraction. To predict the thermal response of a material, accurate values of these kinetic parameters over the range of decomposition are required in a thermal model. In the literature, there are several methods to determine the kinetic parameters from experimental data. One of the most widely used methods is multiple heating rate technique, proposed by Friedman [33] in 1965, through the use of thermogravimetric analysis (TGA). TGA is a common polymer characterization technique to determine the thermal stability of a sample material by recording the weight change of the material as a function of increasing temperature or time at a constant rate. A furnace heats the sample while a sensitive microbalance monitors loss or gain of sample weight due to chemical reactions, decomposition, solvent or water evaporation, and oxidation. Normally, the measurement is carried out in air or in an inert environment, such as nitrogen or argon, at a constant purging rate. The multiple heating rate technique will provide the pre-exponential factor, activation energy, and order of reaction over a wide a range of heating rates.

Henderson [34,35] proposed a method for calculating the kinetic parameters from the Arrhenius kinetic rate equation. Taking the natural logarithm of both sides will result,

$$\ln\left(-\frac{1}{w_0}\frac{dw}{dt}\right) = \ln\left[Af\left(\frac{w}{w_0}\right)\right] - \frac{E}{RT} \tag{2}$$

When plotting $ln[(-1/w_0)(dw/dt)]$ as a function of $1/T$ for all heating rates, linear equations may be fit for each parametric value of w/w_0. These linear equations will have slopes of $-E/R$, and each equation will have y-intercept of $ln[Af(w/w_0)]$ for each

34

parametric value of w/w_0. Then, an average activation energy, E_{avg}, from all of the linear curve fits can be calculated and is used to obtain $ln[Af(w/w_0)]$ for each parametric value of w/w_0. Calculate an average $ln[Af(w/w_0)]$ for each parametric value of w/w_0 for all heating rates. Next, the arbitrary function of weight fraction can be defined as,

$$f\left(\frac{w}{w_0}\right) = \left[\frac{(w-w_f)}{w_0}\right]^n \tag{3}$$

where w_f is the final weight of the material at the end of a reaction in the TGA run. Multiplying both sides by A and taking the natural logarithm will yield,

$$\ln\left[Af\left(\frac{w}{w_0}\right)\right] = \ln(A) + n\left\{\ln\left[\frac{(w-w_f)}{w_0}\right]\right\} \tag{4}$$

When plotting $ln[Af(w/w_0)]$ as a function of $ln[(w-w_f)/w_0]$, linear equation(s) may be used to fit and obtain both A and n.

Another method that is widely used to describe kinetics is the isoconversion method [36]. Since the mechanisms of material thermal degradation are often unknown and too complicated to be characterized by a simple kinetic model. Processes can occur in multiple steps having different rates. The basic idea of the method can be summarized as follows. The rate of degradation is a function of temperature and solid conversion, X_s,

$$\frac{dX_s}{dt} = f(T, X_s) = k(A_s - X_s)^n \tag{5}$$

where X_s is defined as

$$X_s = \frac{w_0 - w}{w_0 - w_f} \tag{6}$$

A_s is the maximum weight loss attainable at each temperature (value has been taken as 1.0), and k is the kinetic constant, which corresponds to the Arrhenius equation:

$$k = A\exp\left(-\frac{E}{RT}\right) \tag{7}$$

A single-order reaction is used ($n = 1$), and the Ozawa-Flynn-Wall method is considered, for obtaining the value of activation energy [37]:

$$\ln\beta = \ln\left(\frac{AE}{R}\right) - 5.33 - \ln(1-X_s) - 1.05\frac{E}{RT} \tag{8}$$

where β is heating rate. Plotting $ln\,\beta$ as a function of $1/T$, linear equations may be used to fit for each parametric value of X_s to obtain the values of activation energy and pre-exponential factor. These kinetic parameters imply that the thermal decomposition of the material can be expressed by a simple kinetic equation, with single effective values of A and E. By adjusting the order of reaction, a separate set of kinetic parameters can be obtained, but when plotting $log\,A$ as function of E, a linear curve fit can be observed using different values of n, which is result of the kinetic compensation effect.

D. Experimental Protocol

Small pieces of sample materials are cut from the twin-screw extruded pellets. The purging gas of interest, either nitrogen or air, must be turned on 30 minutes before the experiment. First, the empty sample pan must be tared while the furnace is at raised position. Then, lower the furnace and load sample material with tweezers into the sample pan with weight of approximately 5 to 10 mg. Next, raise the furnace and seal the system, hold at 25°C, and purge gas for at least 10 minutes prior to initiating the run. The programmed method will then hold the system at 25°C for one minute, then run temperature scan at the desired heating rate to 900°C, and lastly hold the temperature at 900°C for one minute. At the end of the run, if there is any remaining resin, the sample pan must be heated in air at 900°C for 15 minutes to oxidize and completely burn off the resin before the next run. If the weight of the sample is below zero during the run, the data are discarded and a new sample is run.

E. Experimental Results of Pellethane™ Nanocomposites

Thermogravimetric data of the materials are obtained at six different heating rates of 5, 10, 20, 50, 100, and 150°C/min for the Pellethane™ nanocomposites. Four formulations are tested in a nitrogen atmosphere: Kevlar®-filled EPDM, pure TPU, 5% Cloisite® 30B TPUN, and 15% PR-19-PS TPUN. Weight loss, rate of weight loss, and kinetic parameters using the isoconversion method for all four formulations are presented in details in references [38,39]. Representative examples are included in this section.

E.1 Kevlar®-filled EPDM

The fraction of weight remaining (weight loss) and rate of weight loss versus temperature are shown in Figures 3.21 and 3.22, respectively, for different heating rates. Fraction of weight remaining is plotted until 13% remained mass because no additional mass is lost as the temperature increases. As can be observed from the curve of weight loss, the onset temperature of decomposition shifted to higher temperatures, increased from approximately 430°C, with increasing the heating rates. This means that the increased heating rate delayed the solid conversion.

Fraction of Weight Remaining for Six Heating Rates for Kevlar-filled EPDM
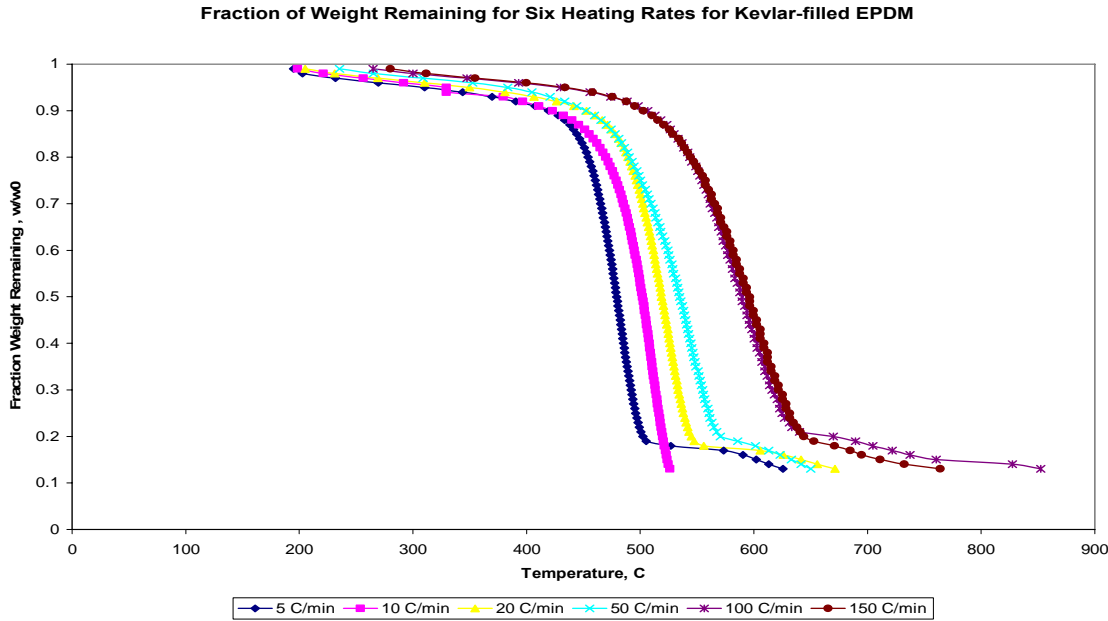
Figure 3.21 Fraction weight remaining for six heating rates for Kevlar®-filled EPDM.

Derivatives of Weight Loss for Six Heating Rates for Kevlar-filled EPDM
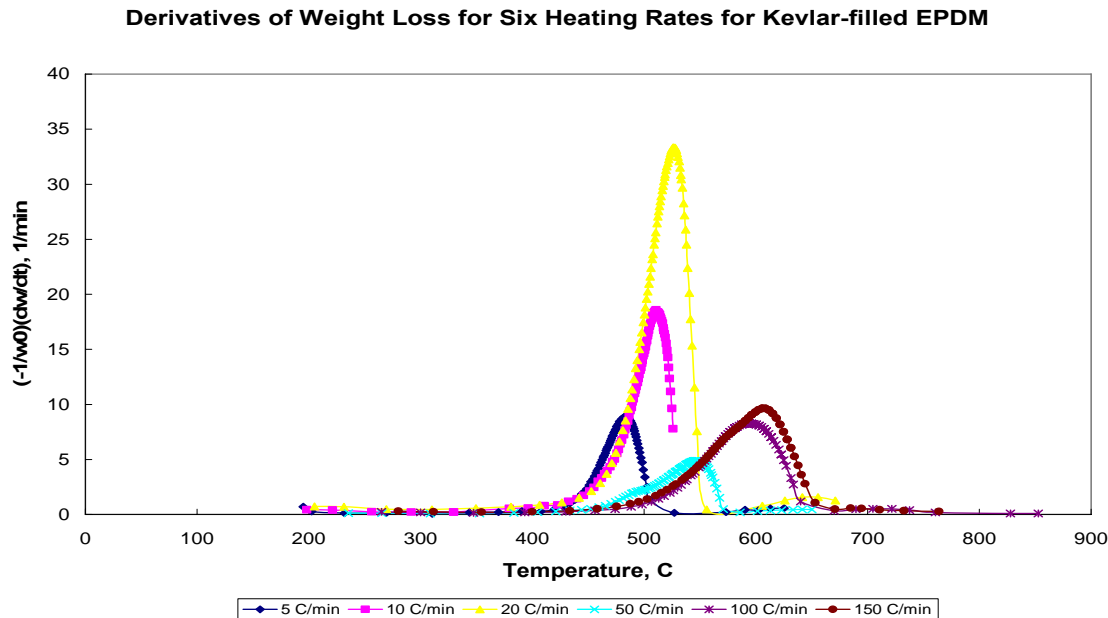
Figure 3.22 Rate of weight loss for six heating rates for Kevlar®-filled EPDM.

At low heating rate (5°C/min), the peak weight loss rate occurs at a lower temperature, at approximately 484°C (757K), and if the heating rate is 30 times (150°C/min), the peak weight loss rate occurs at approximately 612°C (885K), a 16.9% increase.   This quantitative measurement comparison of peak weight loss rates is called thermal stability. Thermal stability provides information about the degradation resistance of a material to thermal load. The activation energy, calculated from isoconversion method, as a function of solid conversion of Kevlar®-filled EPDM is depicted in Figure 3.23.   Until solid

37

conversion of about 0.13, activation energy values are increasing with decreasing solid conversion, dictating the slow weight loss regime. When pyrolysis occurs, the activation energy reached a peak value and slowly decayed up to conversion of 0.90, and then it decreased further upon reaching complete conversion. The apparent average activation energy is 141.4±16kJ/mol, and the apparent pre-exponential factor is calculated to be $4.502 \times 10^{13} min^{-1}$.
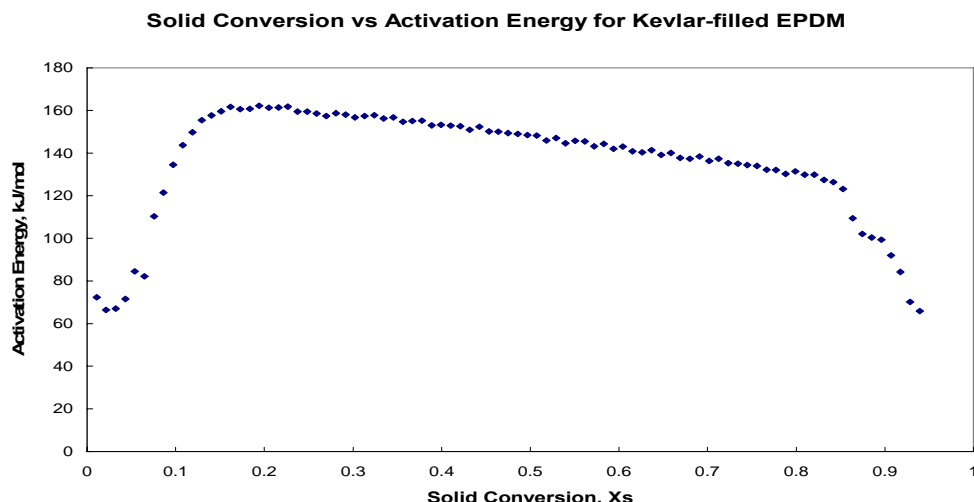
Figure 3.23 Activation energy as a function of solid conversion of Kevlar®-filled EPDM calculated by isoconversion method.

E.2 Pure Pellethane™ TPU

The fraction of weight remaining and rate of weight loss versus temperature are shown in Figures 3.24 and 3.25, respectively, for different heating rates.
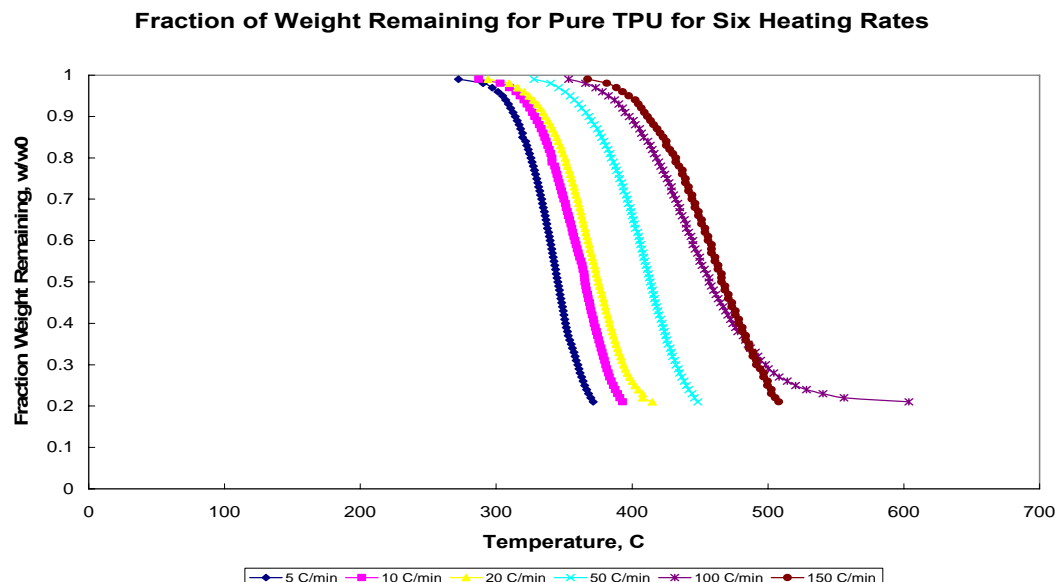
Figure 3.24 Fraction weight remaining for six heating rates for pure TPU.

Derivative of Weight Loss for Six Heating Rates of Pure TPU
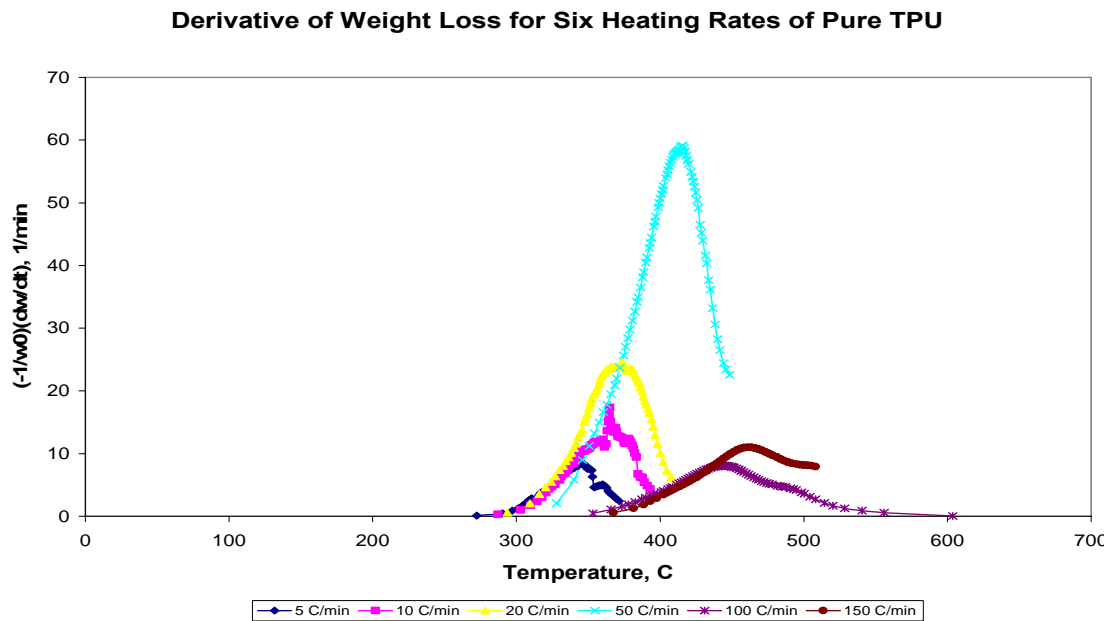
Figure 3.25 Rate of weight loss for six heating rates for pure TPU.

The pyrolysis reaction initiates at approximately 300°C (573K). At low heating rate (5°C/min), the peak weight loss rate occurs at a lower temperature, at approximately 343°C (616K), and if the heating rate is 30 times (150°C/min), the peak weight loss rate occurs at approximately 461°C (734K), a 19.1% increase. The calculated activation energy by isoconversion method as a function of solid conversion of pure TPU is depicted in Figure 3.26. Unlike Kevlar®-filled EPDM, pure TPU degrades at lower conversions. Activation energy value peaks at conversion of 0.04 at approximately 108kJ/mol and decreases slowly. The apparent average activation energy is 96.74±7.9kJ/mol, and the apparent pre-exponential factor is calculated to be 4.292 x 10^7min^{-1}.

Solid Conversion vs Activation Energy for Pure TPU
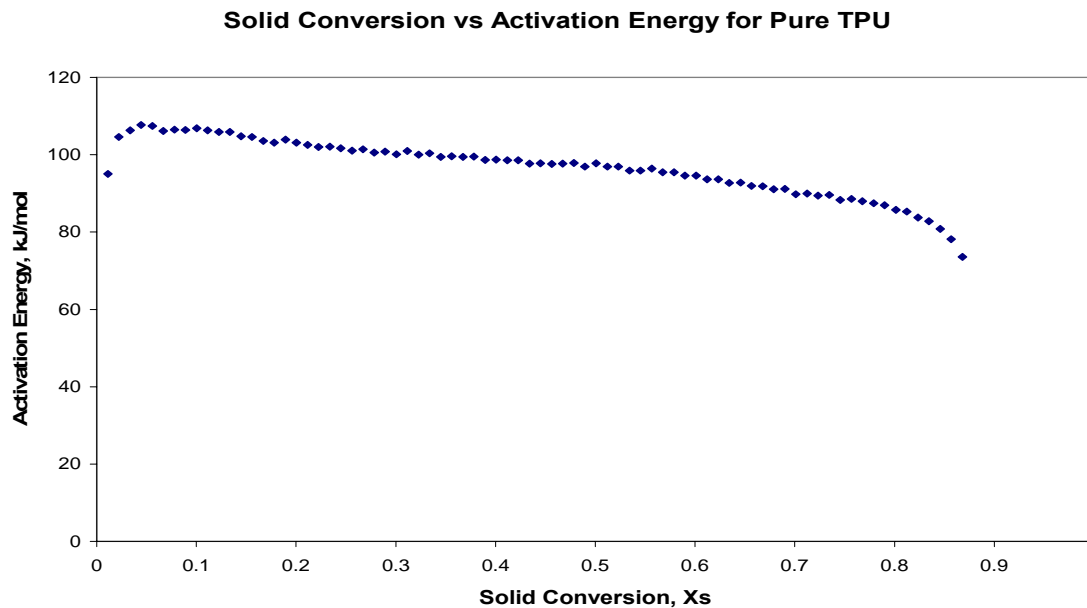
Figure 3.26 Activation energy as a function of solid conversion of pure TPU calculated by isoconversion method.

E.3 Summary of Kinetic Parameters

The results of all kinetic parameters calculations are summarized in Table 3.4. Based on temperatures at peak weight loss rates, Kevlar®-filled EPDM outranked the proposed formulations at all heating rates. However, the percentage of temperature increased of peak weight loss rate from low heating rate (5°C/min) to high heating rate (150°C/min), or the thermal stability from 5°C/min to 150°C/min, showed that the proposed TPUN formulations were more advantageous. The thermal stability from low heating rate to high heating rate increase are 19.6% for 5% Cloisite® 30B TPUN and 20.1% for 15% PR-19-PS TPUN, they are both higher than the 16.9% observed for Kevlar®-filled EPDM. The heating rate for SRM environment is about 180,000°C/min which will be even higher thermal stability extrapolation. TPUN formulations show better stability improvement than Kevlar-filled EPDM [38,39].

TABLE 3.4 Effective Kinetic Parameters Results of Thermogravimetric Data

Formulation	E [kJ/mol]	A [min^{-1}]
Kevlar®-filled EPDM	141.4±16.6	4.502x10^{13}
Pure TPU	96.7±7.9	4.292x10^{7}
5% Cloisite® 30B TPUN	104.5±7.7	3.801x10^{8}
15% PR-19-PS TPUN	104.4±6.2	1.761x10^{8}

F. TGA Analyses of New TPUN (Desmopan™ Nanocomposites)

The Desmopan^{TM} Cloisite® 30B and MWNT samples are tested at 10°C/min, 20°C/min, 40°C/min, and 100°C/min [40]. Samples were made by cutting the lengths of pellets to samples between 13 to 16 mg. Tests show that TGA results are sensitive to

specimen size and shape. By using pellets of the same diameter and cutting them to the specified weight, the shape and size of the samples were kept consistent. Each formulation was tested at the 4 heating rates from $100^{o}C$ to $900^{o}C$.

The results from the 20 cpm heating rate tests are presented as representative of the other 3 heating rates, since the trend of each are similar. Figure 3.27 shows the weight percentage versus temperature data of the neat Desmopan[TM] as well as the 4 Cloisite[®] 30B formulations. The neat Desmopan[TM] degrades rapidly at a lower temperature than the Cloisite[®] 30B formulations. This indicates the addition of Cloisite[®] 30B enhances the thermal stability of the polymer. Thermal stability increases as more nanoclay is added to the Desmopan[TM]. The 2.5% Cloisite[®] 30B formulation clearly is much more stable than the neat Desmopan[TM], and the 5% Cloisite[®] 30B formulation is much more stable than the 2.5% Cloisite[®] 30B formulation. However the 5%, 7.5% and 10% Cloisite[®] 30B profiles appear to be very close. Similar results were observed in the UL 94 test (see Section 3.1.5) where the neat material melted but did not burn, the 2.5% Cloisite[®] 30B material burned but fell apart, and the 5%, 7.5%, and 10% Cloisite[®] 30B materials burned for roughly the same amount of time but did not fall apart.
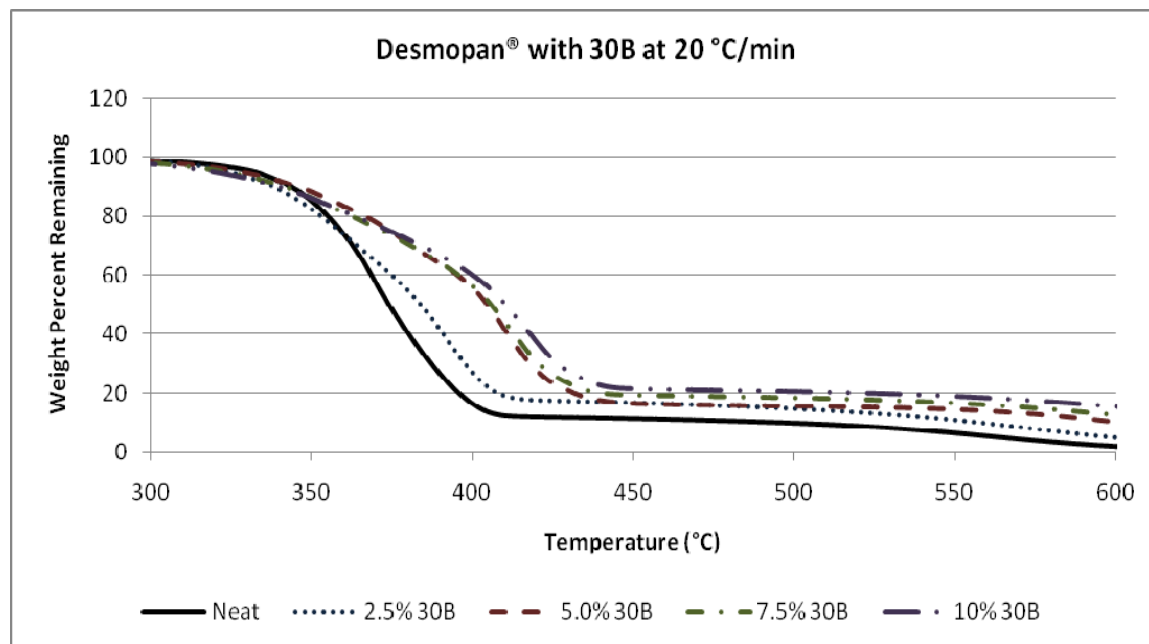
Figure 3.27 Thermogravimetric analysis of Desmopan[TM] Cloisite[®] 30B formulations at 20 CPM.

The onset, 10 weight loss, and 50% weight loss temperatures shown in Figure 3.28 also show the trend that there is drastic increase in thermal stability up to the 5 weight percent formulation. Formulations with a higher weight loading are found to have roughly the same onset and 50% weight loss temperatures. The 10% weight loss temperature is found to be constant throughout all formulations; this means that the enhancements of the Cloisite[®] 30B are not noticed until a higher temperature is reached. Since the Cloisite[®] 30B degrades at a higher temperature then the Desmopan[TM], as the Desmopan[TM] degrades, a larger percentage of the remaining material is Cloisite[®] 30B.

The nanoclay begins to build a larger protective layer preventing more of the Desmopan™ from decomposing.
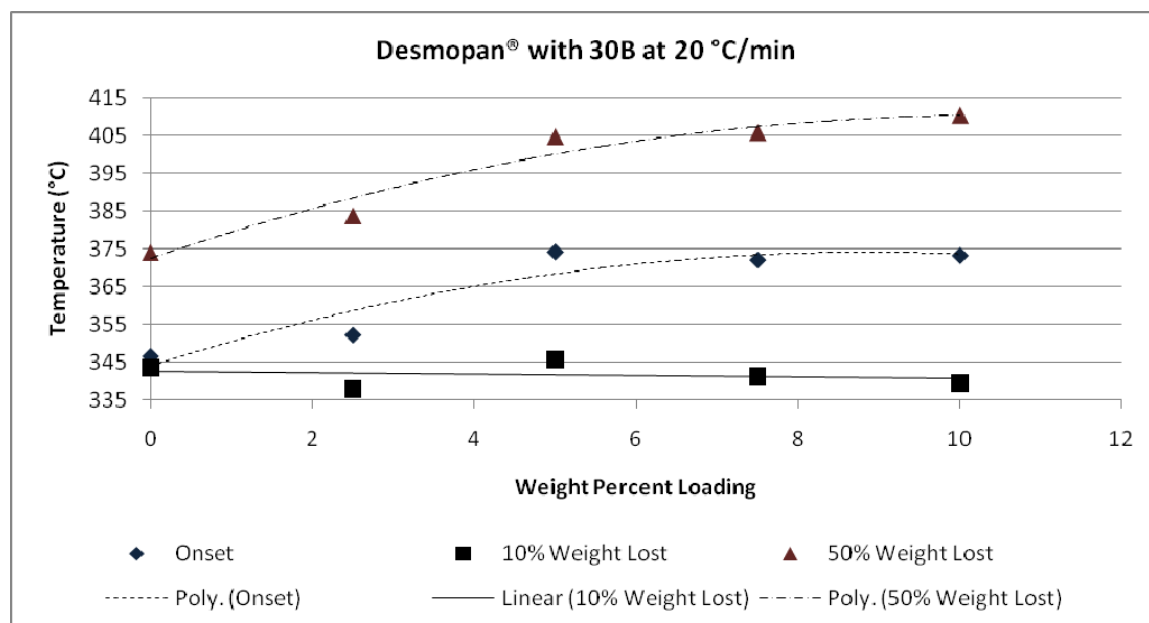
Figure 3.28 Onset and weight loss temperatures of Desmopan™ Cloisite® 30B formulations at 20 CPM.

The rate of weight loss graph, Figure 3.29, shows that one reaction is taking place during this experiment. Increasing the nanoclay loading decreases the peak rate of weight loss as well as increases the temperature at which these peaks occur. This can be observed in the TGA graph which shows that the increase in nanoclay loading stretches the area of largest degradation rather than simply shifts the graph.
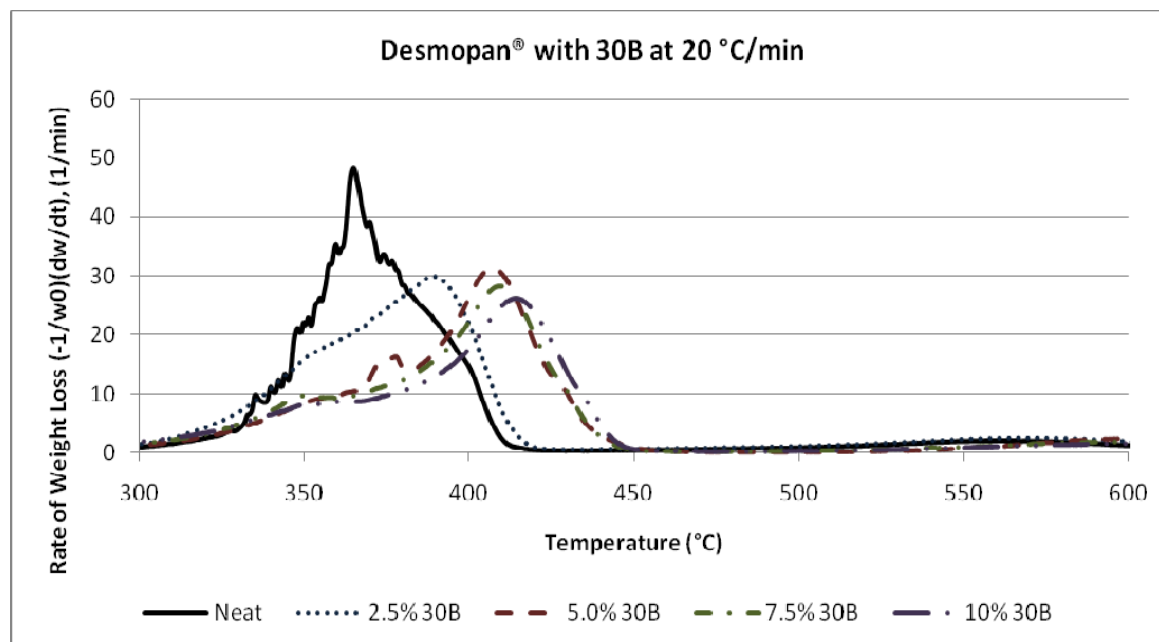
Figure 3.29 Thermogravimetric derivatives of Desmopan^{TM} Cloisite$^®$ 30B formulations at 20 CPM.

Identical test were performed on the MWNT samples. The increase in thermal stability with increase of MWNT loading is observed (Figure 3.30). The addition of 2.5% MWNT is drastically more stable than the neat Desmopan^{TM}. However, unlike Cloisite$^®$ 30B additional loading does not significantly increase the thermal stability. This too was observed in the UL 94 tests (Section 3.1.5), as the formulations were all mechanically weak when burned, and the portion that remained burned for roughly the same duration.
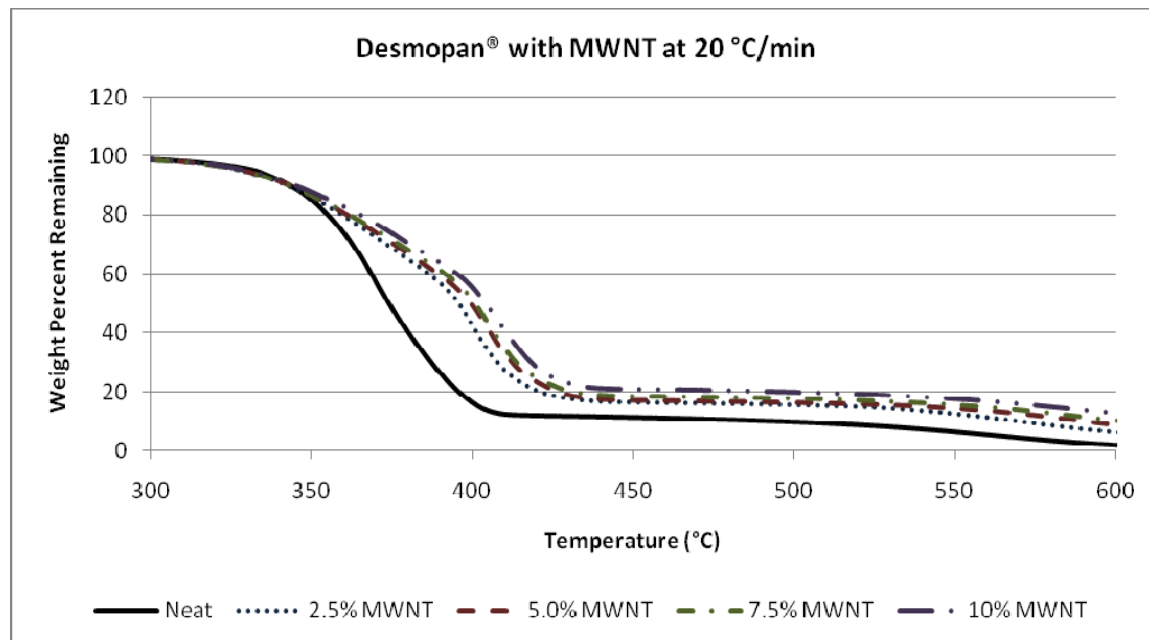
Figure 3.30 Thermogravimetric analysis of MWNT Desmopan^{TM} formulations at 20 CPM.

This is further shown in the onset and 50% weight loss temperature graphs, Figure 3.31. The 10% weight loss temperatures similar to the Cloisite$^®$ 30B results are constant throughout each formulation.
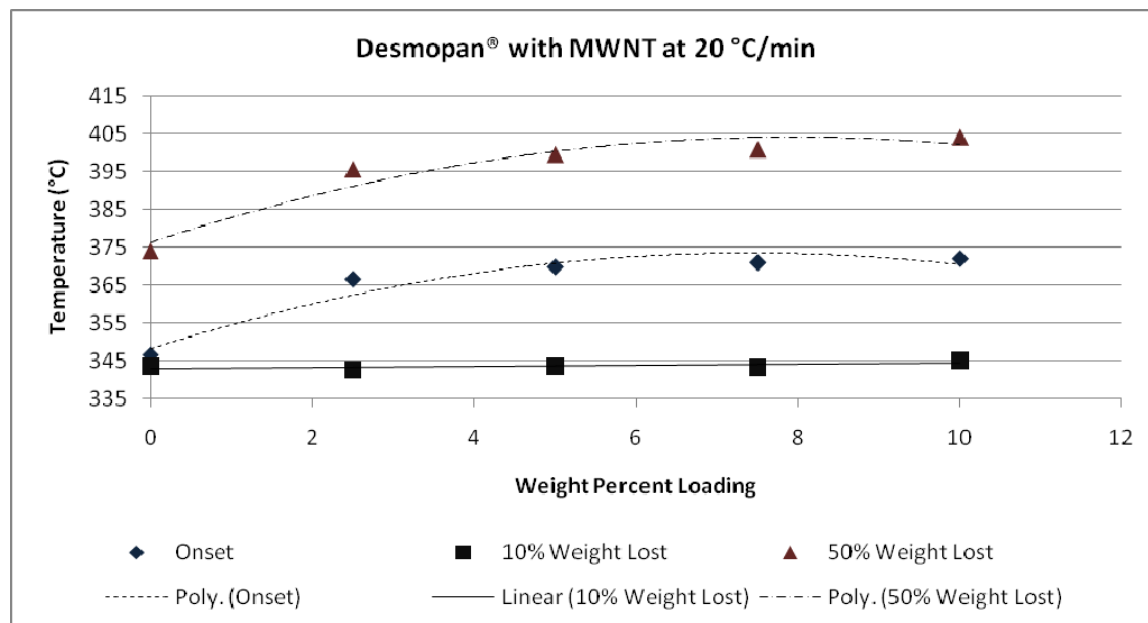
Figure 3.31 Onset and weight loss temperatures of MWNT Desmopan[TM] formulations at 20 CPM.

Similar to the derivative graphs of the Cloisite[®] 30B formulations, as the loading of MWNT increases the peak rate of weight loss decreases and the temperature at these peaks increase (Figure 3.32). These results show that a smaller loading of MWNT will be needed to enhance the material compared to Cloisite[®] 30B. From experience with Pellethane[TM] PNCs, the amount of CNFs needed for enhancement will be more than the necessary Cloisite[®] 30B loading, since the best performing Pellethane[TM] PNCs were found to be 5% Cloisite[®] 30B and 15% CNF.
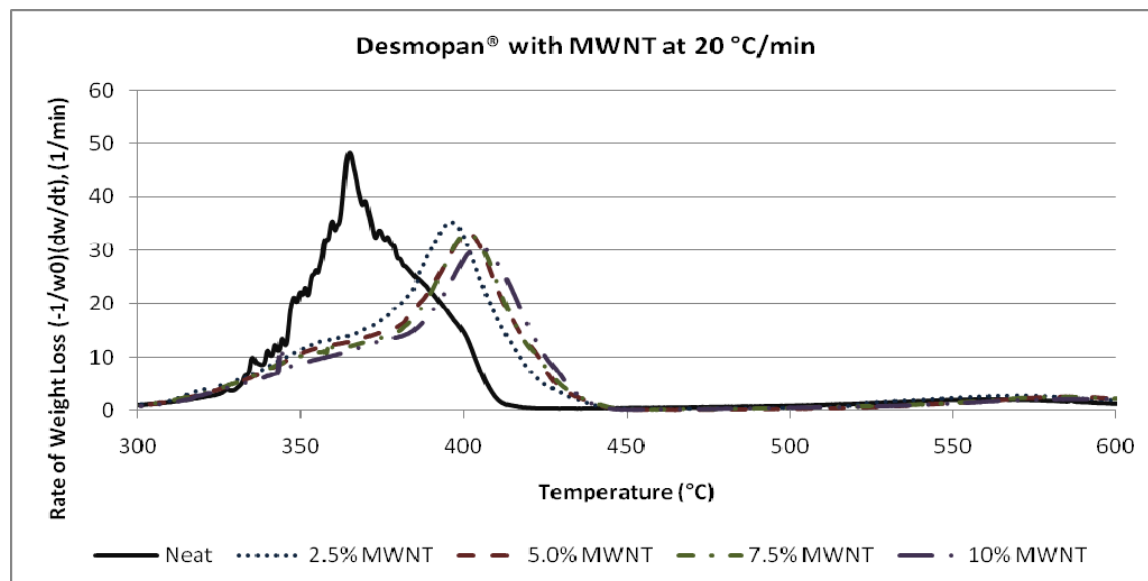
Figure 3.32 Thermogravimetric derivatives of MWNT Desmopan[TM] formulations at 20 CPM.

G. High Heating Rate TGA Analyses of New TPUN (Desmopan™ Nanocomposites)

The thermal degradation of a material is analyzed by examining the kinetics calculated from thermogravimetric analysis (TGA) experiments. In a TGA experiment, the material is placed on a scale within a furnace. As the material is heated the weight loss is measured. These experiments are conducted for materials with different nanoparticle loadings. A shift in the weight loss versus sample temperature graph can be observed as more nanoparticles are added. In addition derivative versus sample temperature graphs are also analyzed to determine changes in material behavior.

TGA experiments are conducted either as isothermal or dynamic. The furnace is raised and held at a specified temperature in isothermal TGA experiments. The furnace in a dynamic TGA experiment on the other hand heats the sample at a constant rise in temperature.   The TGA experiments presented in this study are dynamic TGA experiments. Traditionally heating rates between 5 to 20°C/min (CPM) are used to find kinetic parameters. The kinetic parameters found at these heating rates may not be valid for higher heating rates (up to 500 CPM) if the mechanism of polymer degradation is different.   We will examine if this is true for our set of thermoplastic polyurethane elastomer nanocomposites.

Three formulations of the TPU were studied using a Q5000™ IR TGA machine from TA Instruments: Neat Desmopan®, Desmopan® w/ 5wt% Cloisite® 30B, and Desmopan® w/ 5wt% MWNT [41]. This TGA machine uses an infrared heating mechanism such that the sample can be dynamically heated from 0.1 to 500 CPM with a weighing accuracy and precision of ±0.1% and ±0.01%, respectively, and an isothermal temperature accuracy of ±1%. At each heating rate the machine is Curie point calibrated. Calibration must be performed at each heating rate since different heating rates will affect how closely the thermocouple readings will match the true temperature of the sample. The calibration method along with the settings of the linear heating of the sample is performed in accordance to TA Instruments' manual of the Q5000™ IR TGA machine. Note that the TGA experiments as well as analysis assume that the bulk material temperature and the temperature obtained by the machine are the same.

G.1 Sample Size Effect

The Desmopan® w/ 5wt% Cloisite® 30B formulation was used to determine the effects of sample size on TGA results. The first set of tests was performed on samples cut from the cylindrical pellets produced from the twin screw extrusion process, approximately 3 mm in diameter. Three different sizes were tested at a heating rate of 20 CPM: 2.2mg, 4.4mg, and 14.5mg. The results of these samples are shown in Figures 3.33 and 3.34. The data from the 2.2 and 4.4mg samples closely match each other. However the heavier 14.5mg sample appears to have a slower reaction time. This is due to the fact that the entire sample of the heavier sample reaches the temperature at a longer time than the lighter samples do.
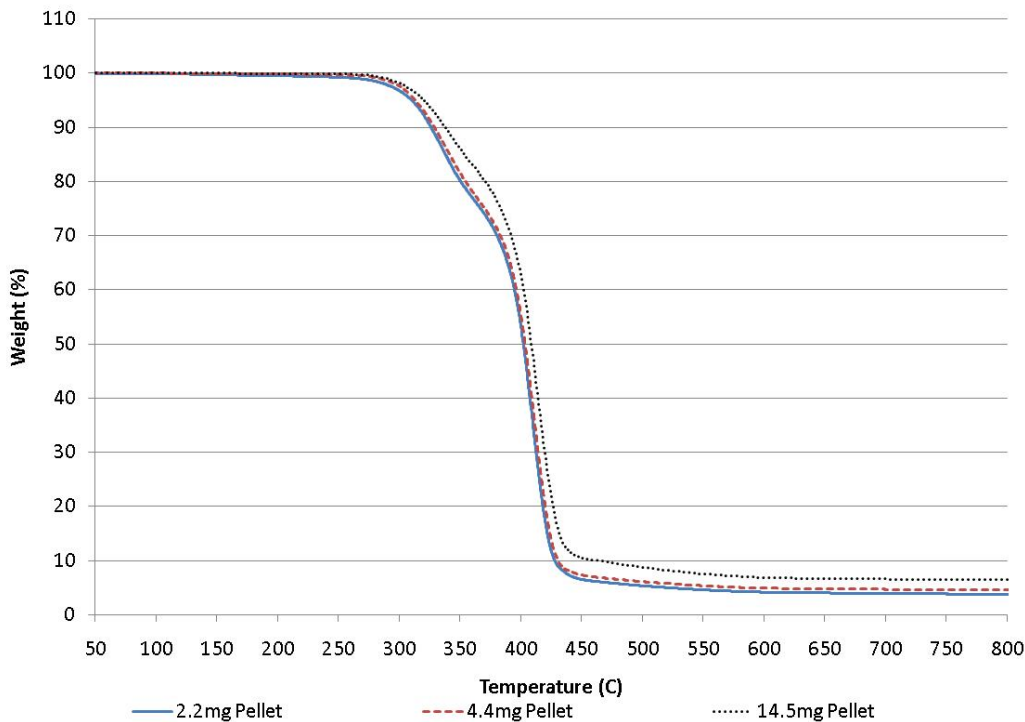
Figure 3.33 Wt.% remaining of Desmopan® 5wt% Cloisite® 30B @ 20 CPM using 3 pellet sizes.
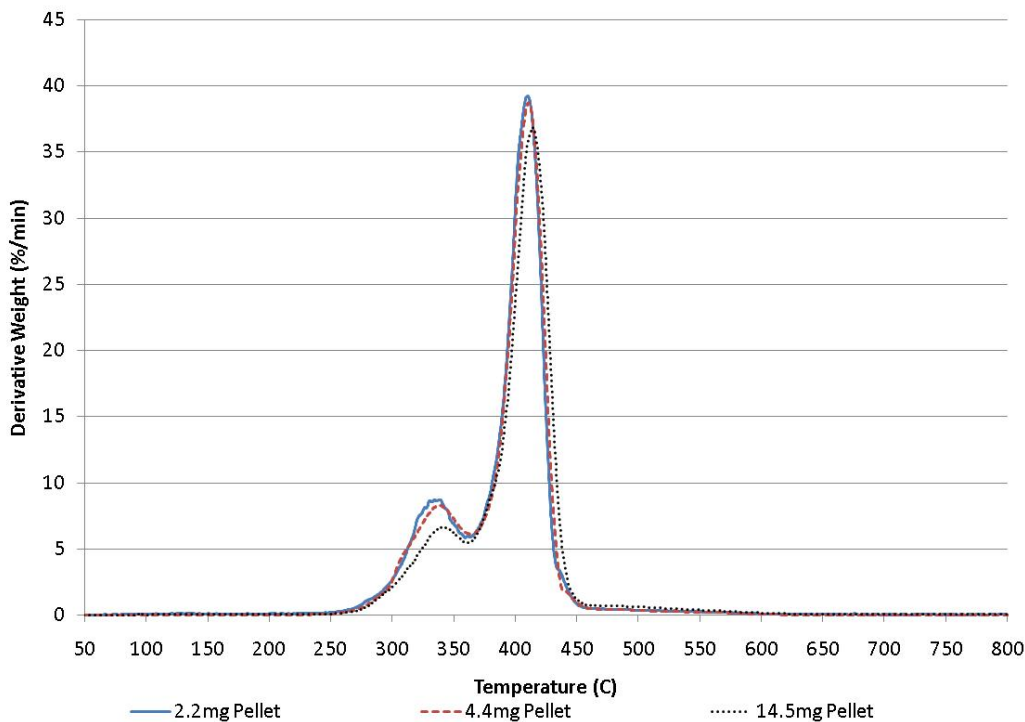
Figure 3.34 Derivative wt.% of Desmopan® 5wt% Cloisite® 30B @ 20 CPM using 3 pellet sizes.

G.2 Heating Rate Effect and Sample Preparation

Further study of Desmopan® 5wt% Cloisite® 30B pellets, less than 4mg, were made at higher heating rates: 250 and 500 CPM. Curie point calibrations were not made for these experiments so kinetic comparisons between tests cannot be made.   However comparisons between samples at a certain heating rate are acceptable. The results show that although the remaining weight % vs. temperature curve is shifted to the right from the 20 to the 250 CPM samples (Figure 3.35) little difference is found between the 250 and 500 CPM. The effects are attributed to the fact that although the samples are small in weight, 2.711 and 1.487 mg for the 250 and 500 CPM experiments, respectively, the heating rate is such that the material response time is slow in comparison.

To improve the response time of the sample, the ratio between the surface area and volume must be increased. This is achieved by using thinner samples. The material is compression molded into thin films about 0.2mm thick. Discs are punched out of these samples at about 1cm in diameter and are tested under the same 3 heating rates (Figure 3.36). The results show that there is a clear distinction between the results found at each of the heating rates.   From these observations, the neat Desmopan® as well as the Desmopan® w/ 5wt% MWNT samples are tested using samples punched out from these films.
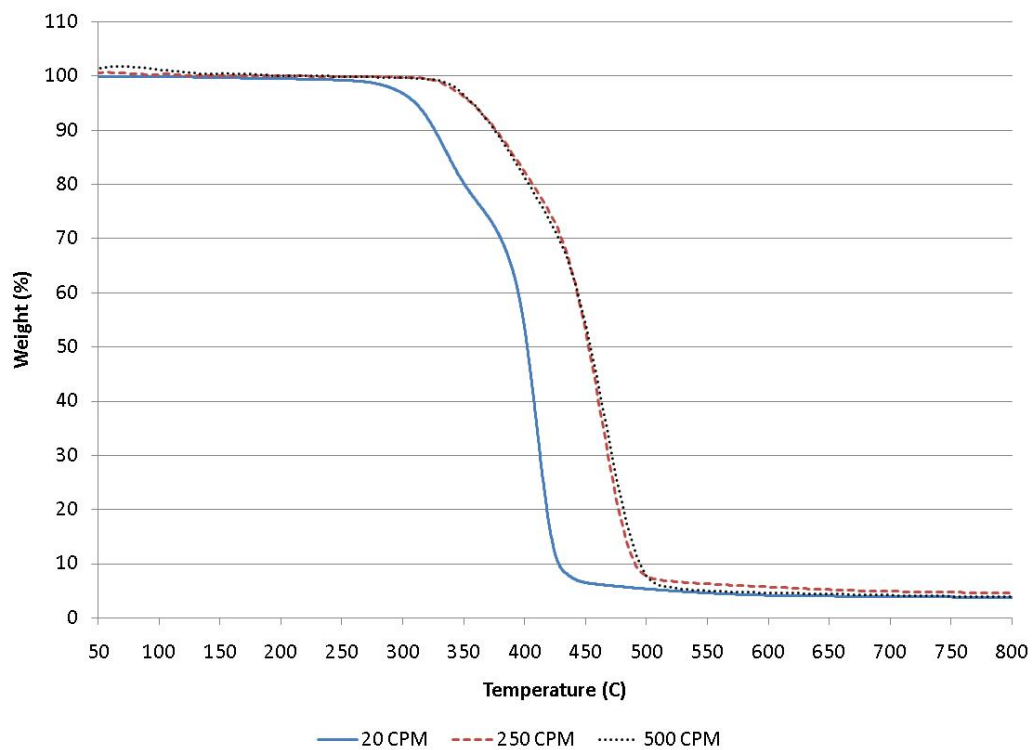
Figure 3.35 Wt.% remaining of Desmopan® 5wt% Cloisite® 30B pellet for 3 heating rates.
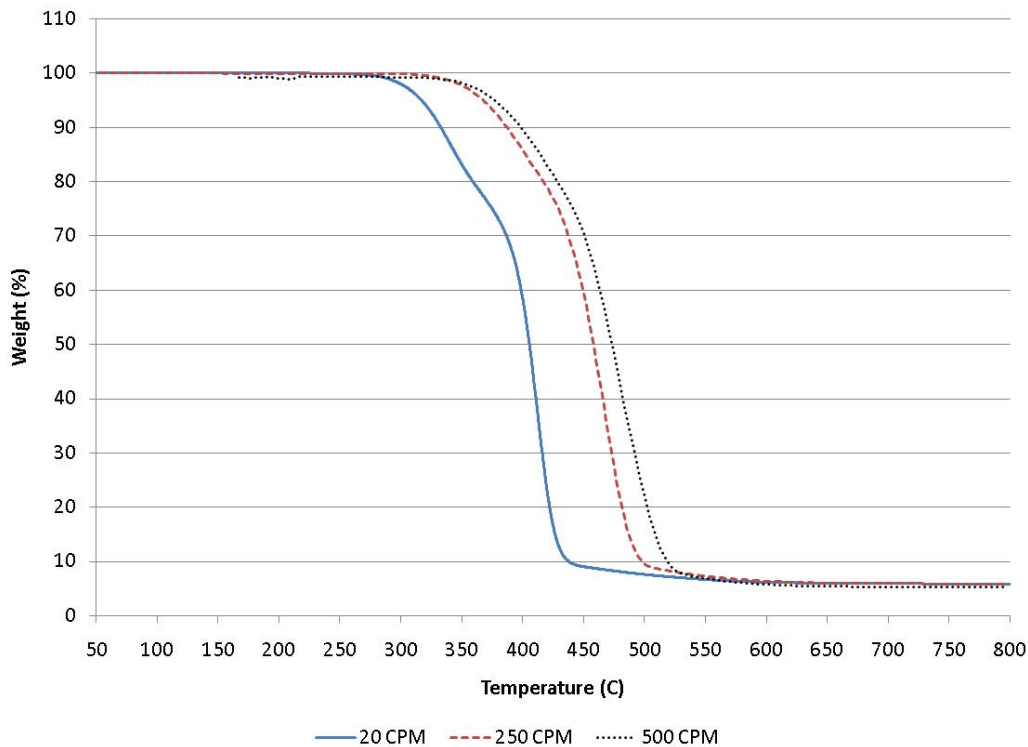
Figure 3.36 Wt.% remaining of Desmopan® 5wt% Cloisite® 30B film for 3 heating rates.

G.3 Neat Desmopan®

The neat Desmopan® film samples are tested for 5 different heating rates: 20, 50, 100, 250, and 500 CPM. Before each experiment, a Curie point test is performed. As the heating rate increases, unsurprisingly the temperature at which a certain weight percentage is observed also increases. Two tests were performed at each heating rate in order to ensure that the data is repeatable. The data were observed to be very repeatable. Therefore, to avoid cluttering the graph, only one set of data is shown here in Figure 3.37. Please note however that both sets of data are used in the kinetic analysis which follows.
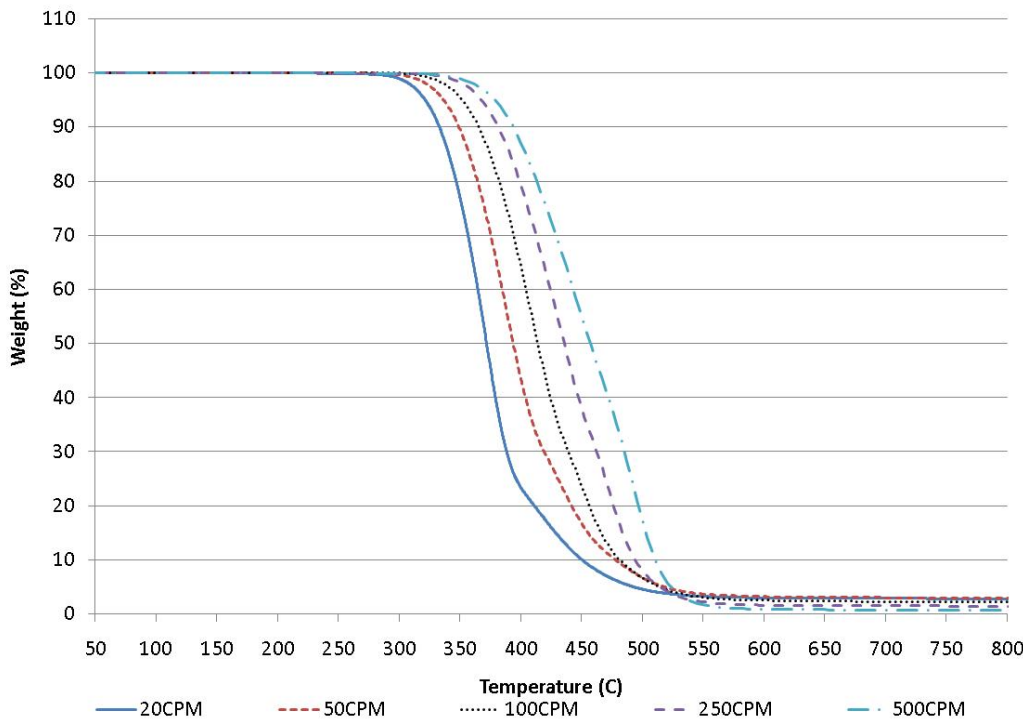
Figure 3.37 Wt.% remaining of neat Desmopan® for 5 heating rates.

It is clear from the derivative weight percentage graph (Figure 3.38) that 2 reactions are occurring. This means that the soft and hard segments of the TPU decompose at different temperatures as well as at different rates. These two reactions are most easily observed at the lowest heating rate, 20 CPM. As the heating rate increases the temperature at which peak reaction takes place also increases. It appears that the range of temperatures over which these reactions take place also broadens, however the temperature at which the first reaction is initiated does not change as heating rate increases. The amplitude as well as the breadth of the two reactions increase with heating rate in such a way that the two reactions are indistinguishable at higher heating rates.
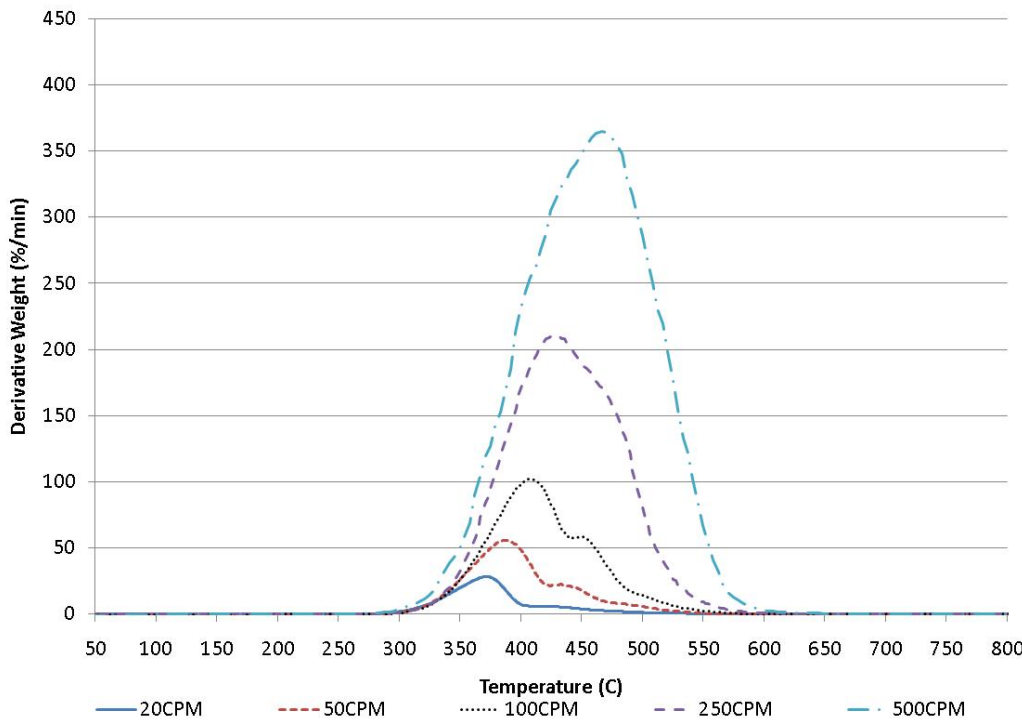
Figure 3.38 Derivative wt.% of neat Desmopan® for 5 heating rates.

G.4 Desmopan® w/ 5wt% MWNT

The experiments performed on the neat Desmopan® were also performed on the Desmopan® w/ 5wt% MWNT samples, Figures 3.39 and 3.40. In contrast with the neat Desmopan®, the rate of the first reaction is slower than that of the second reaction. This means that the small amount of MWNT additive added to the TPU aids in delaying the thermal degradation of the first reaction, however it appears that the degradation that is delayed from the first reaction is initiated at slightly higher temperatures, as the amplitude of the derivative weight percentage of the second reaction is considerably higher. The upper limit of the second reaction shifts dramatically in the MWNT formulations as compared to the neat Desmopan® samples.
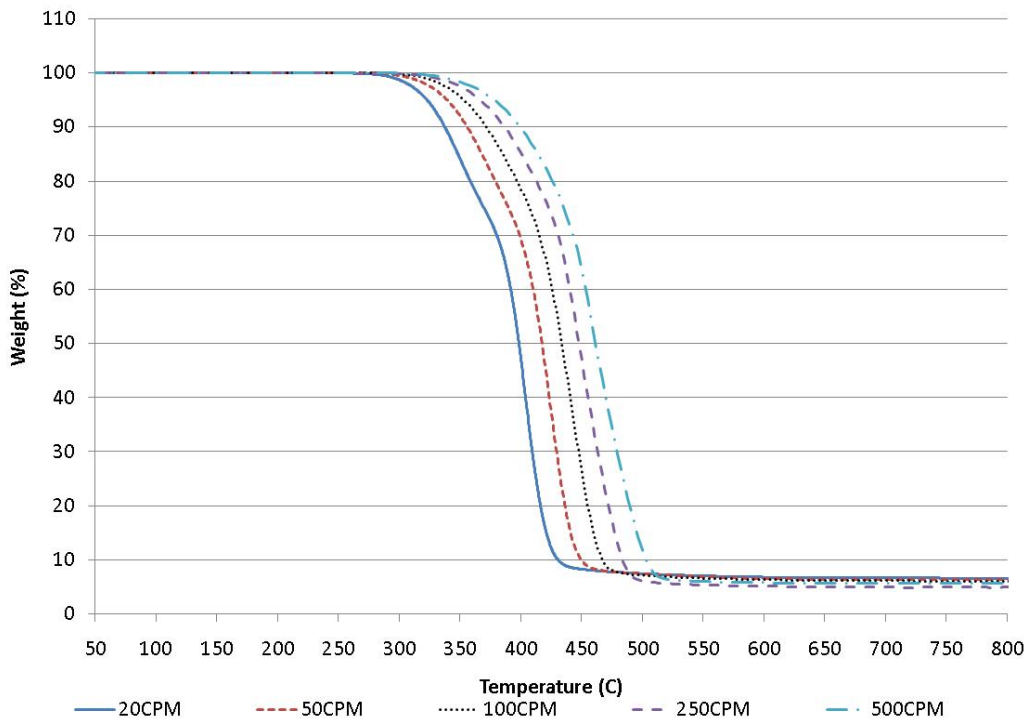
Figure 3.39 Wt.% remaining of Desmopan® w/ 5wt% MWNT for 5 heating rates.
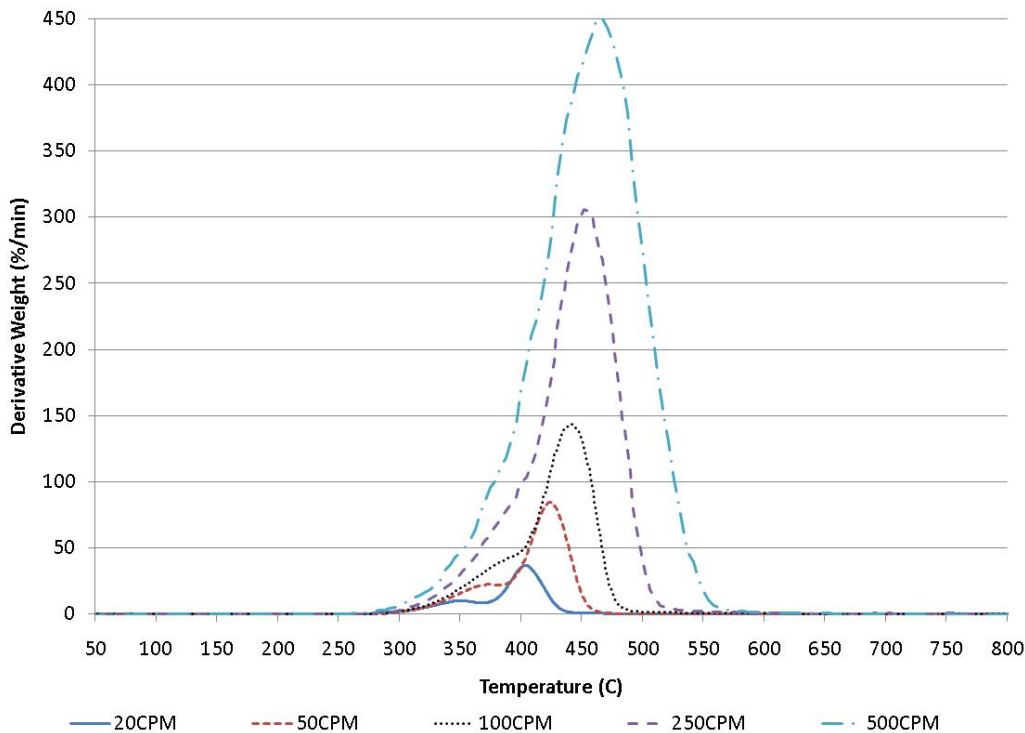
Figure 3.40 Derivative wt.% of Desmopan® w/ 5wt% for 5 heating rates.

51

G.5 Neat and 5wt% MWNT Desmopan® Comparison

As heating rate increases across the different experiments, the rate of material degradation also increases. The rate of material degradation is directly correlated to the amplitude of derivative weight loss percentage. The amplitude of derivative weight loss percentages increases tremendously with increasing heating rate. For this reason the low and high heating rate derivative graphs are shown here separately. Figure 3.41 shows the lower heating rate derivative weight curves for both the neat and 5wt% MWNT Desmopan® samples. The neat Desmopan® derivative weight is greater than 0.5 %/min between 289 and 528°C for the 20 CPM experiment and between 289 and 563°C for the 50 CPM experiment. In comparison the Desmopan® 5wt% MWNT derivative weight is greater than 0.5 %/min between 283 and 453°C for the 20 CPM experiment and between 285 and 530°C for the 50 CPM experiment. As mentioned earlier, increasing the heating rate does not affect the point at which the reactions begin. However the end temperature of the reaction is increased quite a bit. The end of the second reaction in the 50 CPM experiment occurs 35°C and 77°C after it does in the 20 CPM case for the neat and 5wt% MWNT Desmopan® samples, respectively.
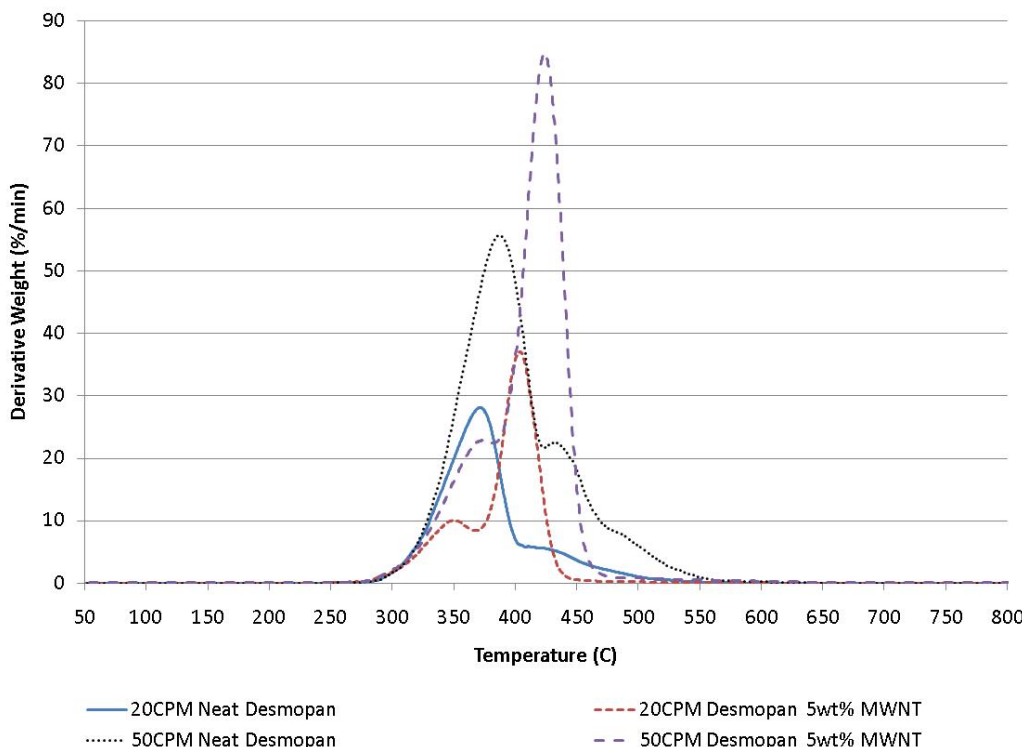
Figure 3.41 Derivative wt.% of Desmopan® neat and w/ 5wt% MWNT @ low heating rates.

In the higher heating rate curves of the derivative weight percentage curves, Figure 3.42, the two reactions are difficult to distinguish. As is observed in the lower heating rates, the amplitudes of the derivative weights are higher in the nanocomposite samples at higher temperatures. The neat Desmopan® derivative weight is greater than 0.5 %/min between 294 and 615°C for the 250 CPM experiment and between 262 and 683°C for the 500 CPM experiment. The Desmopan® 5wt% MWNT derivative weight is greater than

0.5 %/min between 281 and 610°C for the 250 CPM experiment and between 267 and 638°C for the 500 CPM experiment. The initiating temperature of the first reaction is lower in the 500 CPM experiments compared to the experiments from the other heating rates and the end of the second reaction in the 500 CPM experiment occurs 68°C and 28°C after it does in the 250 CPM case for the neat and 5wt% MWNT Desmopan® samples, respectively.
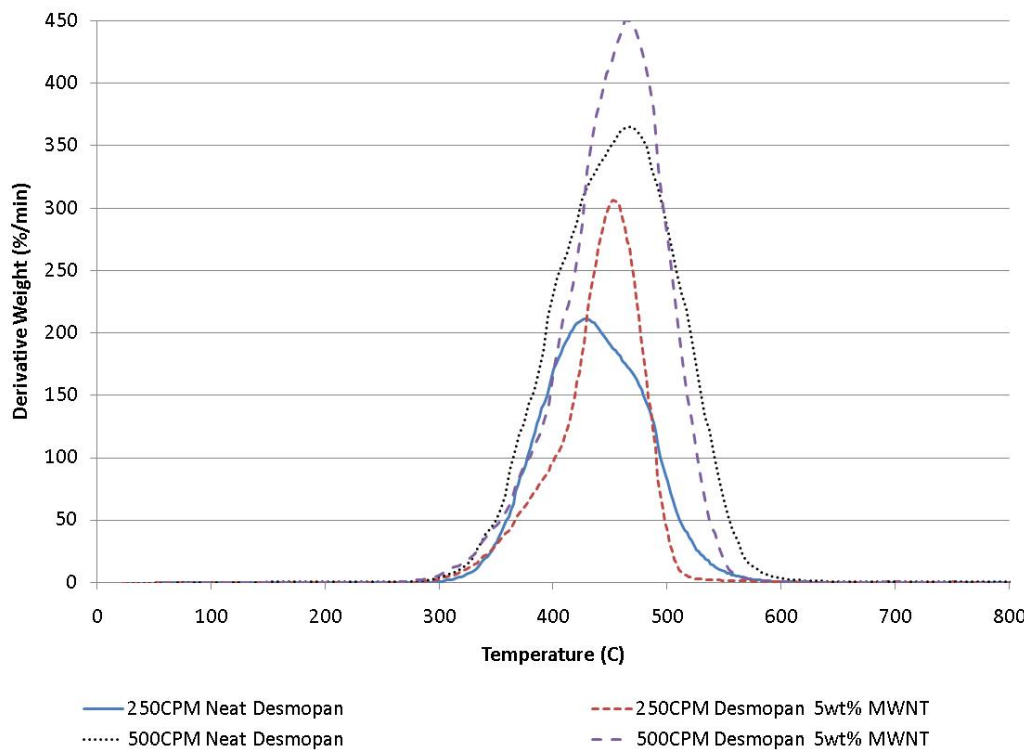
Figure 3.42 Derivative wt.% of Desmopan® neat and w/ 5wt% MWNT @ high heating rates.

After the second reaction, some material residue remains. The remaining weight percentages of the highest and lowest heating rates for both the neat and 5wt% MWNT Desmopan® samples at 800°C are shown in Table 3.5. At the higher heating rate, it appears that a lower amount of material remains. In addition the MWNT samples create a larger char. This remnant is apparent as a larger weight percentage remaining in the nanocomposite samples. The temperatures at which 10, 50, and 90 wt% remains are also shown in Table 3.5. Since the first reaction is slower in the nanocomposite material, the temperature at which 90wt% and 50wt% of material remains is higher in the nanocomposite material compared to the neat material. By the time reaction reaches a point where only 10wt% remains, the temperature is higher in the neat material sample.

TABLE 3.5 **Experimental Results of Desmopan® Neat and w/ 5wt% MWNT @ 20 and 500 CPM**

	20 CPM		500 CPM	
	Neat TPU	**TPU w/ 5wt% MWNT**	**Neat TPU**	**TPU w/ 5wt% MWNT**
Wt. % @ 800ºC	2.8	6.6	0.7	5.8
Temp. (C) @ 10wt%	450	430	510	503
Temp. (C) @ 50wt%	372	398	457	462
Temp. (C) @ 90wt%	333	337	394	400

G.6 Kinetics Calculations

The isoconversion method was performed for the neat and 5wt% MWNT Desmopan® samples. Activation energy and pre-exponential graphs for these two experiments are shown in Figures 3.43 to 3.46. For each material, two experiments were done for five different heating rates. Each of the kinetic parameter figures show results for three sets of data: all five heating rates, lower heating rates, and higher heating rates. Both kinetic parameters found using all five heating rates were higher than when only the lower heating rates were used, which were higher than the values found when only the higher heating rates were used.
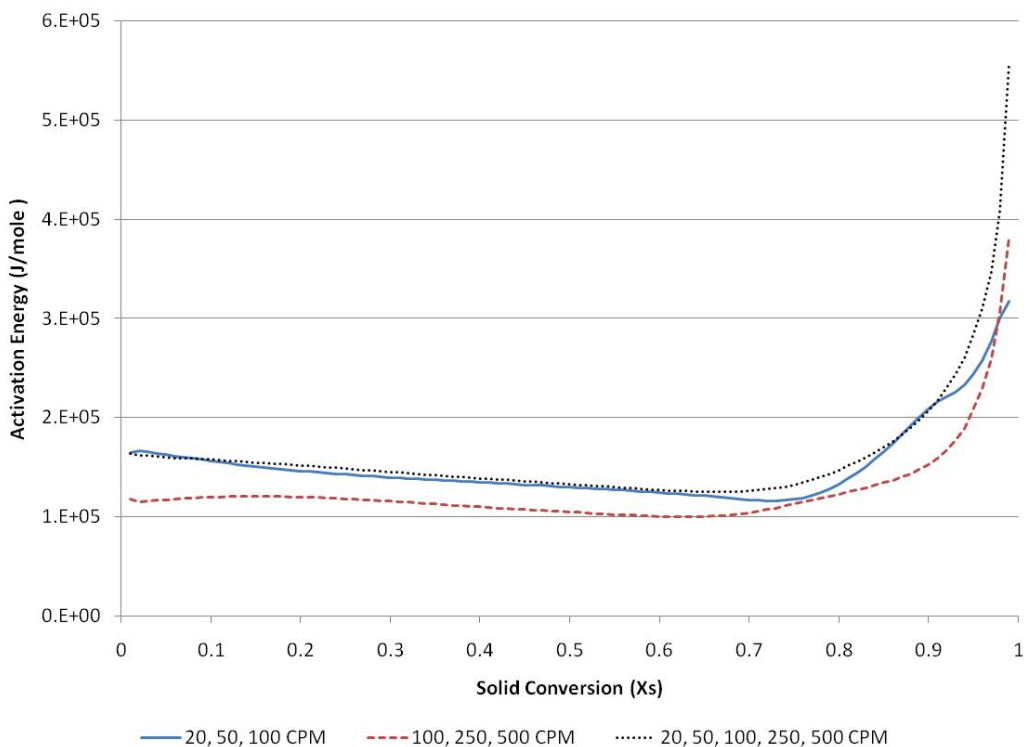
Figure 3.43 Activation energy of neat Desmopan® using isoconversion method, n=1.
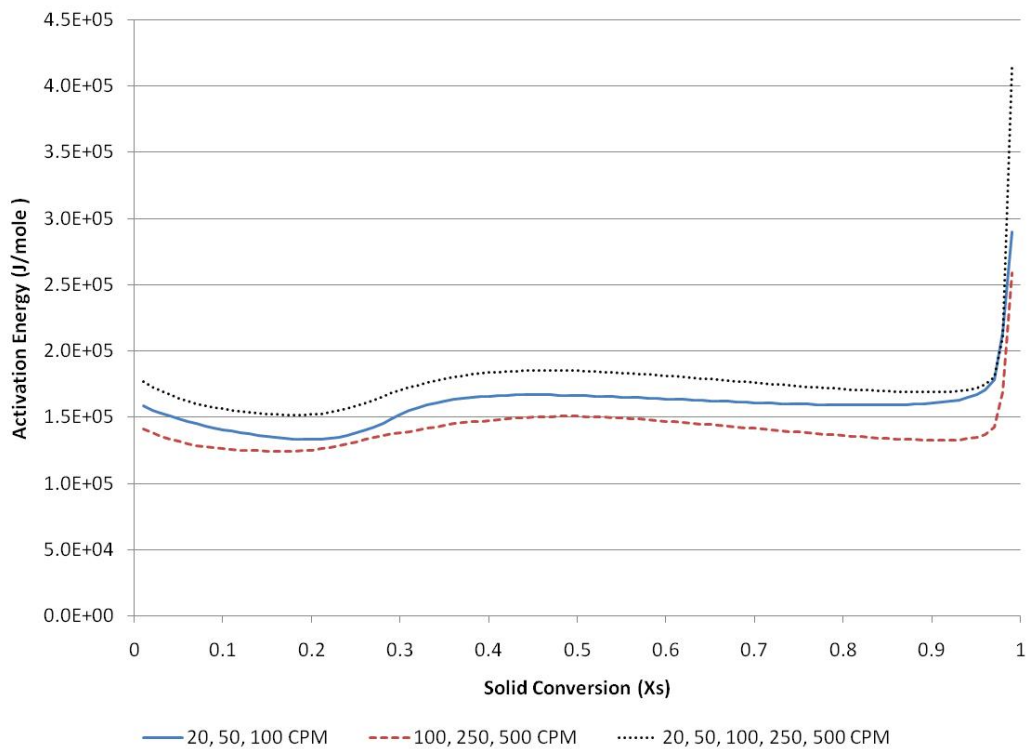
Figure 3.44 Activation energy of Desmopan® 5wt% MWNT using isoconversion method, n=1.
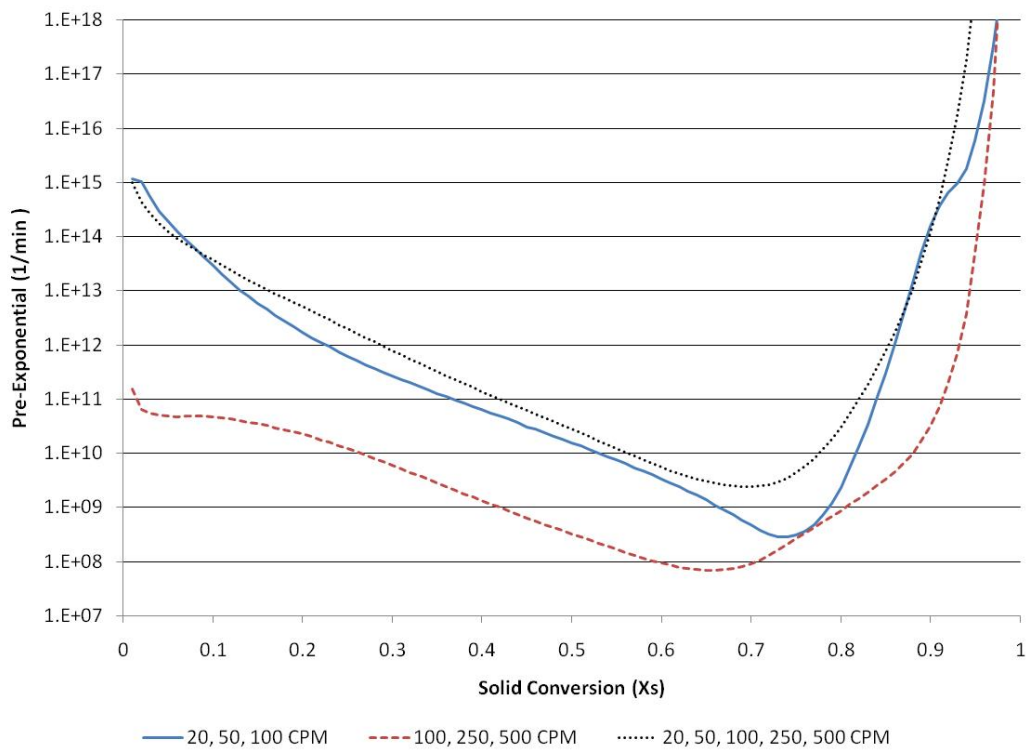
Figure 3.45 Pre-exponential of neat Desmopan® using isoconversion method, n=1.
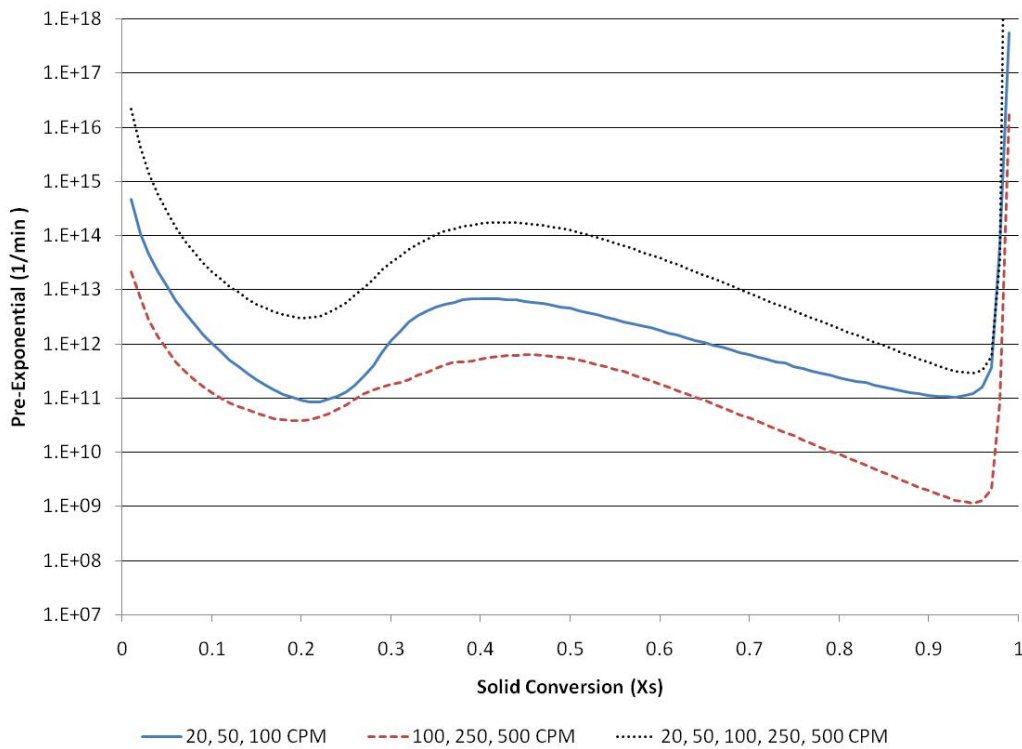
Figure 3.46 Pre-exponential of Desmopan® 5wt% MWNT using isoconversion method, n=1.

As the solid conversion increases past 0.9, the activation energy grows explosively. Table 3.6 shows the average activation energy of these three sets of data when the data are averaged up to Xs=0.9. The differences in activation energies when the different sets of heating rates are used to calculate it shows that using one set of kinetic models is insufficient. This does not necessarily mean that the mechanism of decomposition at these different heating rates is different; it may mean a more sophisticated kinetic study is necessary. A kinetic study of isoconversion with a different order of reaction may be needed. In the kinetic study performed, the Desmopan® 5wt% MWNT sample has higher activation energy than the neat Desmopan® for the total, lower, and higher heating rate experiments used.

TABLE 3.6 Average Activation Energy of Desmopan® Neat and w/ 5wt% MWNT (Xs = 0.01-0.9)

| | Activation Energy (kJ/mole) | |
Heating Rates	Neat Desmopan®	Desmopan® 5wt% MWNT
20, 50, 100 CPM	140.1	155.5
100, 250, 500 CPM	114.8	139.0
All Heating Rates	145.2	171.7

G.7 Summary

The thermal degradation of Desmopan® DP 6065A is studied. Two nanoadditives are added to the TPU: Cloisite® 30B montmorillonite nanoclay and Graphistrength® C100 multiwall carbon nanotubes. A sample of Desmopan® w/ 5wt% Cloisite® 30B is used to study the effects of the sample shape and size. A thin film was found to give results that have the least variability. The effect of sample size increases as heating rate increases.

Two decomposition reactions are observed in the neat material. The first reaction occurs at a slower rate. In comparison, the MWNT loaded nanocomposite has a faster second reaction. The MWNT additive delays the first reaction. The end of the second reaction however occurs at a lower temperature in the nanocomposite material when compared to the neat material.

Kinetic parameters are determined using an isoconversion method. Multiple heating rates are used to determine the activation energy. The calculations show that when lower heating rate data are used in the model, the activation energy comes out higher than when calculated for higher heating rate data. Since the activation energy is obtained by the slope of the heating rate versus temperature graph this signifies that the shift of the weight loss versus temperature curves decreases at higher heating rates. The kinetic parameters found using these two sets of heating rate experimental data are significant enough to suggest that models which use kinetic parameters should not use kinetic parameters found from low heat rate experiments to describe a material that is exposed to a higher heating rate. Additional high heating rate TGA experiments are planned in the next few months in Sandia National Lab.

3.1.6 Flammability Testing and Analyses

A. Test Plan for UL 94

A first set of 5 test specimens were burned above a piece of cotton. The specimens of formulations which dripped consistently burned the cotton piece below. As the specimen fell onto the cotton piece and burned the cotton, the remnants of the fallen piece were difficult to characterize. To better understand and predict the drip, 7 tests of each material formulation were performed without the cotton piece below. The results of these tests are described in the following sections. Note that all descriptions of events at a certain time are in reference to when the flame is first introduced.

B. Neat Desmopan® UL 94 Results

The neat Desmopan® is a V2 polymer since it does drip. The material before and after the UL 94 tests are shown in Figure 3.47. After a flame was introduced to the specimen for 10 seconds, none of the bulk material burned. However, 4 of the 7 specimens did drip. The drip is very liquid like, this can be observed in the fourth burnt test sample shown in Figure 3.47b. When the flame was introduced for an additional 10 seconds, all 7 test specimens dripped. And the bulk material of each of the 7 samples burned for less than 1 second.

<p align="center">(a)   (b)</p>
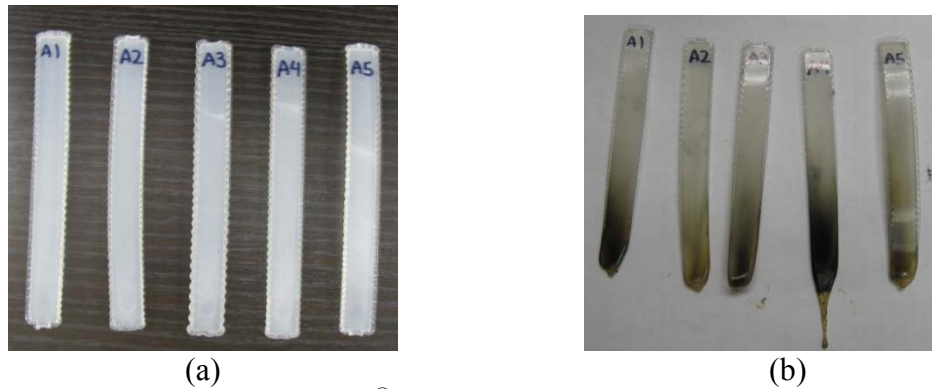
Figure 3.47 Neat Desmopan® (a) before and (b) after vertical UL 94 test.

To understand how the material self extinguishes, a neat Desmopan® specimen was clamped in the same setup as the vertical burn UL 94 setup. Instead of removing the flame after 10 seconds, the flame was held for an extended period of time. A stream of melted material dripped. This drip was on, shown in Figure 3.48. The bulk material however burned in the same way that the pervious tests had shown. The presence of the flame is sufficient to melt the TPU and the conditions of the melt are sufficient for it to burn. Since the presence of a flame for an extended period of time does not cause the bulk material to burn for any longer, this means that a significant amount of the heat is transferred into melting the material. And as the burning material drips additional heat is removed from the bulk material.
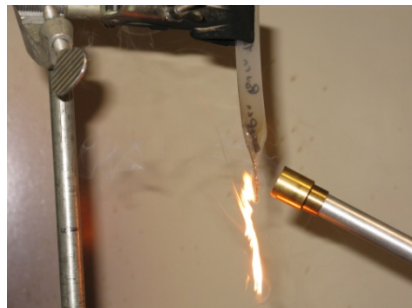
Figure 3.48 Neat Desmopan® extended burn time.

The viscosity of the material plays a large role. A much stiffer TPU elastomer, Pellethane™, was also tested. The most significant difference between the two TPU's is that Pellethane™ is a much stiffer material, with a shore hardness of 94A as compared to the shore hardness of Desmopan®, 65A. When the neat Pellethane™ was tested, it burned for a short time and began dripping. A much larger portion dripped away due to the extended burn, the Pellethane™ specimens after the test are shown in Figure 3.49. The reason that it burned for a couple of seconds is that the material's melt is more viscous than that of Desmopan® and flows slow enough that the ignited melt ignites material around it. The Desmopan® melt flows fast enough that there is not enough heat kept near the specimen to burn it for an extended period of time. After the second flame is removed in specimens 3 and 4, Table 3.7, the neat Pellethane™ burned for over 40 seconds whereas the other 3 specimens burned for less than 10 seconds. This shows that Pellethane™ is sensitive to this set of test parameters, and that there is a critical burn time.

<p align="center">58</p>

TABLE 3.7 Neat Pellethane™ Burn Times After 1st and 2nd Flame

	Burn Time (sec) After 1st Flame Removed	Burn Time (sec) After 2nd Flame Removed
Specimen 1	3	6
Specimen 2	2	1
Specimen 3	4	44
Specimen 4	6	57
Specimen 5	3	3

Figure 3.49 Neat Pellethane™ specimens after UL94 test.

C. Desmopan® Clay Formulation UL 94 Results

The next test involves Desmopan® with 2.5wt% nanoclay formulation, Figure 3.50. Note that the addition of nanoclay to the transparent neat material gives the material a tan pigment. This formulation behaved significantly different from the neat Desmopan® under UL 94 testing. The specimen began to burn after the flame was removed and no melting at the bottom of the burning piece was evident as it was in the neat Desmopan®. However as the specimens burned, it became structurally weak and began to fall apart. This under UL 94 still classifies as a drip. Each of the 7 specimens tested, had between 4 and 8 pieces fall during the test. The first drop occurred at an average of 39 seconds, and the last drop occurred at an average of 85 seconds. The first piece that fell ranged between 0.5" and 1.5" long. Smaller pieces were observed to fall afterwards as well. The size of the subsequent drops is a factor to the loss of material structure after the first drop. After the last piece dropped, about a quarter inch of material remained held in the clamp. This specimen continued to burn for an average of 185 seconds. After that time a second 10 second flame was introduced, but the specimen did not burn or drip. This signifies that all combustible material was burned during the first 10 second of flame exposure.
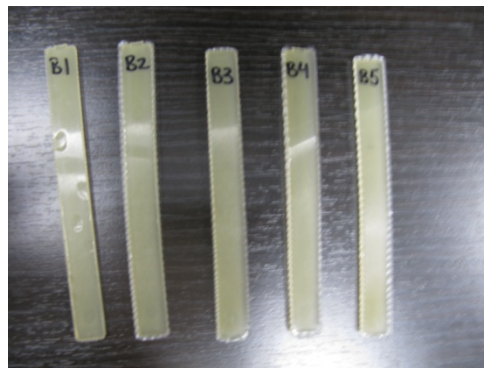
Figure 3.50 Desmopan$^{®}$ + 2.5 wt% Cloisite 30B before vertical UL 94 test.

The nanoclay prevents the specimen from dripping like the neat material. It provides both a thermal boundary as well as increases the melt viscosity. The surface of the first dropped piece has a solid burn structure. However, the center is melt-like and elongates slowly as it falls. The melt-like properties are visible at this location and the increase in viscosity from the neat material is clear. After the first drop subsequent drops do not have a consistent shape or size because of the melt elongation.

A higher loading of nanoclay, 5wt%, decreases the number of drops to just one. This drop occurs on average at 76 seconds, about twice as long as in the 2.5wt% nanoclay specimens. The specimens that drop are also much longer, between 4" and 4.625". The specimens have a burn time of 177 seconds, slightly shorter than the burn time of the 2.5wt% nanoclay samples. In both the 2.5wt% and 5wt% nanoclay Desmopan$^{®}$ formulations, cracks appear in the specimen while it burns. These cracks are associated with thermal stress and out-gassing of the polymer. The locations that these cracks appear are not predictable, however depending on the specimen formulation, a crack occurring at a specific location may or may not lead to a piece falling. Pieces of the 2.5wt% specimen fall almost immediately with each crack. The first piece of 5wt% nanoclay specimen that dropped had cracks occurring as high as 4.125" from the bottom of the specimen was observed. This signifies that there is an increase in mechanical strength of the specimen with increased nanoclay loading. Mechanical properties of these PNCs will be measured in our later studies.

This trend of increasing mechanical strength is also observed in the higher nanoclay loadings since none of the 7.5 or 10wt% nanoclay specimens' fall. During the burning of 7.5wt% and 10wt% nanoclay, cracks were not observed. The 10wt% samples before and after UL94 testing are shown in Figure 3.51. The burn time of these specimens were longer than the nanoclay formulations that did drop. The 7.5wt% and 10wt% nanoclay specimens burned for an average of 228 and 237 seconds, respectively. After the specimen burned it was weighed, the original mass of the 7.5wt% and 10wt% nanoclay specimens was 6.1 to 6.2g and after completely burned was 0.9 to 1.1g, about 5/6 of the sample in weight had gassed off.

(a)   (b)

Figure 3.51 Desmopan® + 10 wt% Cloisite® 30B (a) before and (b) after vertical UL 94 test.

The range of drop times as well as the burn times of each formulation of the nanoclay family is shown in Table 3.8. As more nanoclay is added, the number of drops decreases. In addition, since the strength of the charred material is increased a longer specimen is required to induce a drop leading to a longer time before the first drop occurs. Since each of the nanoclay formulations did not burn on the second introduction of the 10 second flame, all combustible material is assumed to have been consumed. Specimens which had sections that dropped have shorter burn times than that of specimens that did not drop. This may be due to the fact that because specimens that dropped had not been completely consumed the time required to burn that section has been eliminated or shortened.

TABLE 3.8 Nanoclay Drop and Burn Times

	# of Drops	1st Drop Time (sec)	1st Drop Length (in)	Last Drop Time (sec)	Burn Time (sec)
2.5wt% Nanoclay	4 to 8	39	0.5" – 1.5"	85	185
5wt% Nanoclay	1	76	4" – 4.625"	---	177
7.5wt% Nanoclay	0	---	---	---	228
10wt% Nanoclay	0	---	---	---	237

D. Desmopan® MWNT Formulation UL 94 Results

The percentage of nanoclay added to the neat Desmopan® significantly affected the pigmentation. Adding even a small amount of MWNTs to the neat Desmopan® made the material completely black so that visually the different weight percentages of MWNT are indiscernible, Figure 3.52.

| (a) | (b) | (c) |
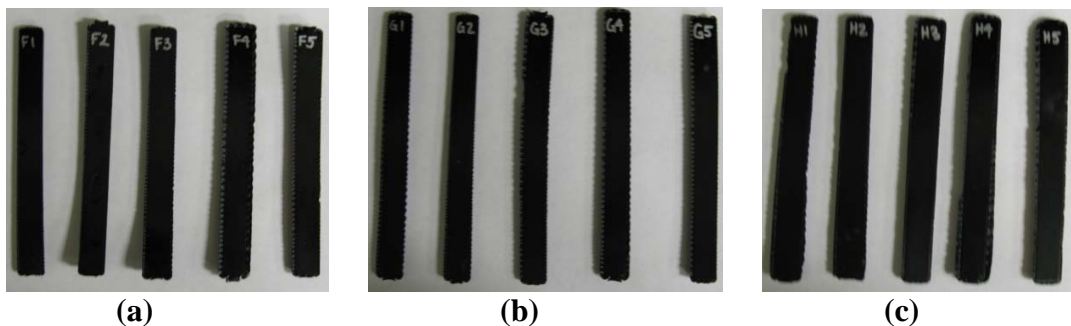
Figure 3.52 Desmopan® + (a) 2.5wt%, (b) 5wt%, and (c) 7.5wt% MWNT before UL 94 test.

The 2.5wt% MWNT samples took on average 33 seconds before the first piece dropped, about the same time the 2.5wt% nanoclay samples dropped, 39 seconds. This drop however is of much smaller samples, approximately 0.1 g. The difference may be due to the type of char formation each creates and the shape of the nanoclay is platelets and a larger surface area remains at the surface after the polymer is melted and burned. The MWNT specimen cracks everywhere and continuously drops small pieces until about 119 seconds after the flame is first introduced. A small section remains clamped and continues to burn. The burn time for the 2.5wt% formulation is 175 seconds.

The 5 wt% MWNT specimens holds together better. Initially the specimen elongates without visible cracking. After about 30 seconds cracks occur and cause the specimen to fall at 63 seconds. This is twice the time it takes for the 2.5wt% MWNT specimens to begin falling. The first specimen that falls is between 2" and 2.625" long. The burnt specimens are extremely brittle. Increasing the loading to 7.5wt% and 10wt% MWNT decreased the number of drops to no more than 1. In fact 2 of the 7.5wt% MWNT specimens and 5 of the 10wt% MWNT specimens did not have pieces drop. Of the specimens that did drop, the drop occurred at 106 and 109 seconds for the 7.5 wt% and 10 wt% MWNT formulations, respectively. As shown in Table 3.9, the length of the 1st drop specimen increases with MWNT loading up to 7.5wt%. The length of the dropped specimen at 10wt% MWNT does not follow this trend. This is due to the unpredictable location of the cracks. In each of the MWNT formulations, cracks occur everywhere, the amount of cracking is significantly more than that observed in even the 2.5wt% nanoclay samples. In the 10wt% MWNT samples which dropped, cracks occurred at both sides of the specimen and met at the center. If the cracks were offset vertically, a drop would not have occurred.

TABLE 3.9 MWNT Drop and Burn Times

	# of Drops	1st Drop Time (sec)	Length 1st Drop (in)	Last Drop Time (sec)	Burn Time (sec)
2.5wt% MWNT	Continuous	33	~0.1 grams	119	175
5wt% MWNT	2 to 4	63	2"-2.625"	85	171
7.5wt%	0 to 1	106	3.5"-4.375"	---	200

MWNT 10wt% MWNT	0 to 1	109	2.875" – 3.875"	---	230

E. Desmopan® CNF Formulation UL 94 Results

The last nanoadditive formulation tested was of CNF. The samples in the virgin form look identical to MWNT samples, however burn very differently. Bubbling on the surface is observed, whereas the change in topography of the MWNT and nanoclay formulation surfaces is less dramatic. The 5wt% CNF sample elongates quite a bit even at the surface. This is very different from the nanoclay and MWNT drops, where the surface shape remained and the melt at the center of the specimen elongates. The elongating portion drips as a viscous liquid. Small solid pieces not fully melted, flow through the elongating portion and speed up the drip process.

The bulk material is only on fire in the area which is elongated, ½". As the flame begins to propagate into the section that has not elongated that section also deforms. It then begins to drip, flame propagation is slowed. The first drip occurs at 20 seconds, faster than any of the other nanomodified formulations. The sample continues to drip until it has all dripped at 152 seconds.

Increasing the loading to 10wt% makes the drop have more surface structure. However once these specimens fall and hit the table the shape deforms. These drop sections are not brittle, but mush-like. After these specimens which have fallen and cooled, they become brittle as do the char of the other TPUNs. The flame propagates faster in this formulation because the added CNFs slow dripping. However the propagation of the flame is still much less than that observed in the MWNT and nanoclay tests. The 10wt% CNF samples drip from 34 to 117 seconds, when all material has dripped.

The pieces of 15wt% and 20wt% CNF specimens that drop can be distinguished however do deform due to its liquid like properties. As Table 3.10 shows, increasing the loading lengthens the time before the 1st drop occurs as well as shortens the time in which the last drop occurs. This however does not mean that the speed of drip increases with increased loading. As loading increases, the number of drops decreases, as does the time between drops. The flame propagation is a factor of the amount of flammable portion held with the specimen. The longer 1st drop time, allows the flame to propagate through a larger volume of the bulk material.

TABLE 3.10 CNF Drop and Burn Times

	# of Drops	1st Drop Time (sec)	Last Drop Time (sec)	Burn Time (sec)
5wt% CNF	Continuous	20	152	152
10wt% CNF	Continuous	34	117	117
15wt% CNF	8	39	109	109
20wt% CNF	1-2	63	82	161

F. Microstructural Analyses of Post-test TPUNs

Additional studies on quantifying the strength of the burnt samples are being conducted. As specified, the Desmopan™ 2.5% Cloisite® 30B samples fell apart during test while the Desmopan™ 5%, 7.5%, and 10% Cloisite® 30B samples did not. However when the burnt samples were handled, it was clear that samples with less Cloisite® 30B were more fragile. The center of mechanical bar specimens will be burned for a specified amount of time in all formulations and tested in an Instron machine. When the samples are being burnt at the middle, the specimen must be held horizontally. Both ends must be fixed, because the material quickly weakens when heated. The shape of the mechanical bar must remain straight, and the tapered ends must not be burned in order for an accurate tensile test to be performed. Some specimens have mechanically failed while the fixtures, which were used to hold the specimen during burning, were removed. A shorter burn time or different grip mechanism must be applied in order to conduct further studies.

In addition, a scanning electron microscope (SEM) will be used to examine UL 94 samples. Four different stages will be examined: virgin material, heated unburned material, partially burned material, and fully burned material. The purpose of examining each portion is to determine how the fire changes the material and how the nanofillers change material properties during heating and flaming. A first attempt at this test was performed on Desmopan™ 10% Cloisite® 30B. A flame was introduced to a UL 94 bar for 10 seconds. When the flame was removed the specimen was allowed to burn. After 60 seconds the flame was put out, about half of the top portion of the material is unburned, this is taken as the heated unburned material. Another UL 94 bar was burned and allowed to burn for 30 seconds after the flame was removed before the flame was put out. The bottom burned section is taken as the partially burned material. A final UL 94 bar is allowed to burn until it self extinguishes which lasted over 200 seconds; this was taken as the fully burned material.

Cross section as well surface SEM images of these 3 differently heat treated materials are shown in Figures 3.53 and 3.54, respectively. The most noticeable changes are not surprisingly observed in the cross section SEM images. Although the differences between the heated and burned samples are easily observed in these images, the partially and fully burned images are difficult to distinguish. Taking SEM images of samples burnt for shorter 30 seconds may show the expected progression. When images of other formulations are also taken the fully burned images will likely be the same. However, the partially burned images are expected to differ based on how well additional nanofillers provide a thermal boundary for short instances of burning or heating.

(a)   (b)   (c)
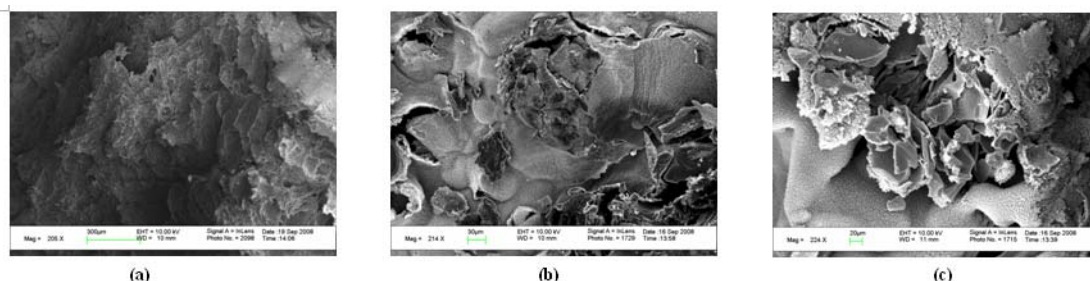
Figure 3.53 Cross section SEM micrographs of (a) heated, (b) partially burned, and (c) fully burned Desmopan^{TM} 10% Cloisite$^{®}$ 30B.

(a)   (b)   (c)
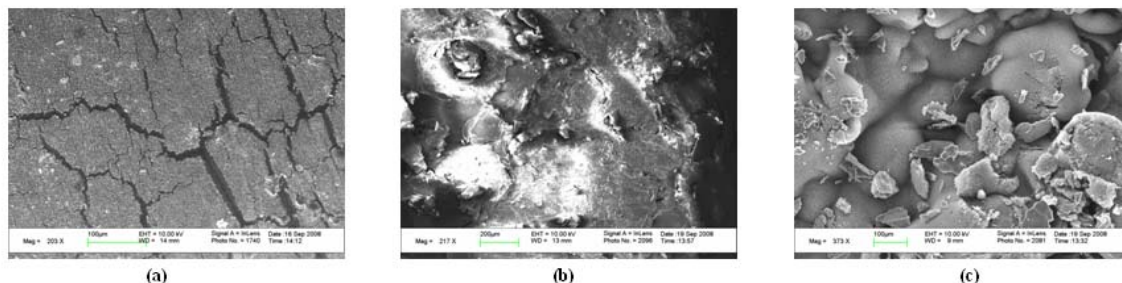
Figure 3.54 Surface SEM micrographs of (a) heated, (b) partially burned, and (c) fully burned Desmopan^{TM} 10% Cloisite$^{®}$ 30B.

G. Summary

The UL 94 tests have shown the behavior of these TPUNs under fire conditions. The neat Desmopan$^{®}$ formulations melt and burn for less than one second. The low viscosity allows the flammable section to quickly drip from the bulk material. Comparison with Pellethane^{TM} samples also shows that the melt burns. However due to the differences in melt viscosity, the neat Pellethane^{TM} specimen burned for a longer period of time. The neat Desmopan passes V1, whereas all formulations of nanoclay, MWNT, and nanoclay fail V2 regardless if drip occurred or not since each burns for well over 30 seconds.

In each family of nanoadditives, an increase in nanoadditive loading increases mechanical stability during and after the flame test. A number of factors show this increase in mechanical stability. The time it takes for a piece of a specimen to fall increases as nanoadditive loading increases. The size of this dropped piece also increases with increased loading. This is significant because it means that a larger weight is required for the structure at a specific point to fail. This shows the increase in the strength of the char and the melt.

The failure mechanism of each TPUN is different. Cracks appear in the nanoclay and MWNT specimens. The location of these cracks are not predictable, however the effects of a crack in a certain region may or may not be significant, depending on the TPUN formulation. In the case of nanoclay loadings above 7.5wt%, no cracking is observed and none of the specimens drop. In the case of MWNT loadings above 7.5wt% all of the specimens show that cracks appear, and some of the specimens had drip. Whether or not these specimens dripped depends on both the location of the crack relative to the bottom of the specimen as well as if two cracks on opposite sides of the specimen appear at the same distance from the bottom of the specimen.

3.1.7 Flammability and Physical Properties Correlation

Flammability properties of the TPUNs have been discussed in details in the above section. A brief summary of the test and results are included in section. The amount of nanoadditives added while processing the material is determined by a weight fraction. Knowing the density of both the polymer and nanoadditive as well as the weight fraction

of the desired formulation is not sufficient to determine the final nanocomposite density. The processing procedures have an effect on the final density and hardness. These physical properties will be studied to examine if there is a correlation across the different TPUN families.

A. Flammability, Density, and Shore Hardness Tests

More detailed flammability test results can be found in Lee *et al.* [40,42] and flammability test results are summarized in this study. Each formulation was tested with a vertical UL 94 test [29]. Seven (7) tests of each formulation are conducted for repeatability of experiments. 5" x 0.5" x 0.125" samples are hung lengthwise and exposed to a 1" flame for two 10 second duration. The time that each sample burned after the flame is removed as well as the properties of how the material broke apart during the burning process was analyzed. Density measurements were conducted using the pellets obtained from the twin screw extruder and studied in a picnometer. While the hardness measurements were measured per ASTM D2240-05 [43] using a type A durometer with a 4" x 4" x 0.5" specimen. Measurements were taken at 5 different locations of the plate and averaged to avoid sectional discrepancies.

B. Flammability Results

Some of the neat material dripped after the first 10 second flame was introduced. After the second 10 second flame was introduced all 7 samples dripped. The drip is very fluid-like and because of the low viscosity of the material the burning section dripped and less than 1 second of the bulk material burned after the flame was removed. As increasing weight loading of nanoadditives are tested, the number of times a specimen that falls decreases. In addition, the length of the specimen that drops also increases. In Table 3.11, the range of the number of drops for each of the 7 specimens of each formulation is shown. In addition, the time at which the first and last piece drop is shown. The time it takes for the entire specimen to extinguish is also shown.

TABLE 3.11 TPUN Drop and Burn Times

	# of Drops	1st Drop Time (sec)	1st Drop Length (in)	Last Drop Time (sec)	Burn Time (sec)
2.5wt% Nanoclay	4 to 8	39	0.5" – 1.5"	85	185
5wt% Nanoclay	1	76	4" – 4.625"	---	177
7.5wt% Nanoclay	0	---	---	---	228
10wt% Nanoclay	0	---	---	---	237
2.5wt% MWNT	Continuous	33	~0.1 grams	119	175
5wt% MWNT	2 to 4	63	2"-2.625"	85	171
7.5wt% MWNT	0 to 1	106	3.5"-4.375"	---	200
10wt% MWNT	0 to 1	109	2.875" – 3.875"	---	230
5wt% CNF	Continuous	20	---	152	152
10wt% CNF	Continuous	34	---	117	117
15wt% CNF	8	39	---	109	109
20wt% CNF	1-2	63	1.75"-3"	82	161

The above results show that for each specific formulation, an increase in weight loading of nanoadditives would enhance the mechanical strength of the burned material. This is observed as the length of the 1st drop increases. In addition, the time at which the first drop is observed also increases. This means that more of the material is burned before it drops. The surface of the 2.5wt% nanoclay sample burns and chars while the center elongates and is melt-like. As the weight loading increases, the amount of the center melt structure decreases preventing drops from occurring at the 7.5 and 10wt% nanoclay samples. The MWNT samples dropped small pieces continuously in the lowest weight fraction formulation, 2.5wt%. The higher weight loading of MWNT samples show significant crack formation along the edges of the specimen. In contrast, the CNF samples show bubbling of the surface while it burned. The CNF samples elongate significantly more than the nanoclay and MWNT samples do.

C. Density and Shore Hardness Results

The density as well as shore hardness is expected to contribute to how well the material withstands flame environments. The measured density of the neat material during the experiment of the nanoclay and MWNT samples was 1.10 g/cc and was 1.09 g/cc during the CNF samples experiment, which is about a 1% difference. In addition, the neat Desmopan® was found to have a shore hardness of 60.7A. The neat density and shore hardness of Desmopan® provided by the manufacturer are 1.09 g/cc and 65A, respectively. The density (Figure 3.55) and shore hardness of the nanocomposite materials are shown in Table 3.12.
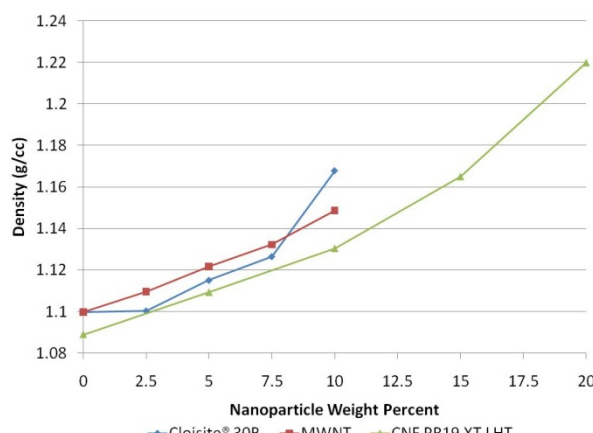
Figure 3.55 Density of PNC with respect to nanoparticles loading.

TABLE 3.12 TPUN Density and Shore Hardness

	Density (g/cc)	Shore Hardness A
2.5wt% Nanoclay	1.10	69.8
5wt% Nanoclay	1.12	75.8
7.5wt% Nanoclay	1.13	80.6
10wt% Nanoclay	1.17	84.6
2.5wt% MWNT	1.11	67.8
5wt% MWNT	1.12	72.2
7.5wt% MWNT	1.13	76.6

10wt% MWNT	1.15	78.8
5wt% CNF	1.11	66.4
10wt% CNF	1.13	76.8
15wt% CNF	1.17	81.4
20wt% CNF	1.22	89.8

The correlation with flammability performance to these two properties is based on the fact that the failure of a specimen during testing is a relationship between the strength of the specimen compared to the hanging weight of the specimen at a specific location. For this reason, a sample with higher density would require more strength in order for the sample to be held. The hardness of a sample gives some indication of strength as it is the stiffness of the material that prevents the material from acting as a viscous melt. The problem with this approach however is that the density measured as well as the strength that is derived from the hardness shown here are for a virgin material. After the material is burned it is not clear what the density is since the polymer is continuously degassing.

However, the strength of the material increasing with relation to the weight loading is supported by the fact that as increased nanoadditive loading the density increases at a slower rate than the shore hardness does. The 7.5 and 10wt% nanoclay formulations had no drops, so is for this purpose the best performing formulation in the flammability test. As shown in Table 3.12, the 7.5wt% nanoclay sample has a shore hardness of over 80A with a density of less than 1.13 g/cc. In comparison, the highest weight percentage of MWNT has a density of close to 1.15 g/cc, but the shore hardness is less than 80A. In addition, the CNF sample shows that a density of 1.13 g/cc is related to a hardness of less than 77A, as shown in the 10wt% CNF sample data.

The correlation however cannot be completely generalized across different nanoadditives as mentioned earlier. This is observed by comparing the 10wt% CNF and the 7.5wt% MWNT samples. These two samples have roughly the same density and shore hardness, about 1.13 g/cc and 76.7A, respectively. In fact, the 10wt% CNF sample has a lower density and higher hardness rating. However, the flammability tests showed that the 7.5wt% MWNT behaved well, whereas the CNF sample dropped very fluid-like. As the 10wt% CNF samples dropped, the dropped portions turned into mush. So the fact that a strong char was not created greatly affects the performance.

D. Summary

The flammability tests show that the nanoclay formulations behave very well as none of the samples dropped when over 7.5wt% is added. The corresponding weight percentage of MWNT showed slightly worse performance as a couple of the samples over 7.5wt% MWNT added had 1 drop. This drop was a large portion of the initial sample. The CNF samples behaved the worse, a significantly larger weight percentage was necessary in order for the samples to have only one drop, 20wt% CNF.

A correlation was attempted between the density and hardness properties of the virgin materials with respect to their flammability performance. The flammability performance was gauged on how many drops the sample formulations had. The main argument for this process is that the hanging weight of the burning sample compared to the strength of the sample determines if a portion of the material will drop. This correlation was able to justify the superior performance of the nanoclay samples. The density at the 7.5wt%

nanoclay sample was less than that of the CNF and MWNT samples in order to obtain a specific hardness. However, a comparison between the 7.5wt% MWNT and 10wt% CNF samples showed that although the density and hardness were the same, the flammability behavior and thus performance were drastically different.

This shows that the density and hardness of a material are significant but insufficient properties that would be needed in order to predict the flammability performance of a specimen. The main property that is lacking is char strength. In addition, because the melt of each nanocomposite family behaves differently, the extent at which the virgin strength of the material is maintained cannot be simply extended. Rather than predicting the flammability performance, using the flammability performance as well as the density and shore hardness of the virgin material, melt behavior of the samples may be able to be predicted.

3.1.8 Eroding Thermocouple Gauges

NANMAC Corporation makes one type of thermocouples known as self renewing thermocouples. The purpose of these thermocouples is that they erode at the same rate as the material they are used in because they are housed in the test material. As the thermocouple erodes, a new junction is created, thus the surface temperature of an ablating material can be measured continuously.

The thermocouple is composed of 2 thermocouple ribbons, 50 µm thick, separated by a 5 µm thick dielectric. The thermocouples are then sandwiched between two dielectrics, Figure 3.56. The thermocouple ribbon and dielectrics are then sandwiched in a test material. The geometry of the test material is a circular cone frustum with a large diameter of 0.19" and a small diameter of 0.08". Each thermocouple is 3/8" long, and 3 are placed in a 0.5" diameter 1" long gauge. The first thermocouple will be placed at the surface and the remaining thermocouples placed 1/8" and ¼" deep to measure the heat soak temperatures. To house and manufacture these gauges, 1" thick 4" cross sectional panels are needed. These NANMAC gauges will be made with the Pellethane[TM] samples proven to be the best formulations, Pellethane[TM] 5% Cloisite® 30B and Pellethane[TM] 15% PR-19-PS. If the tests show that these gauges give valuable data, these gauges will be made for the Desmopan[TM] formulations found to perform the best in ablation tests.
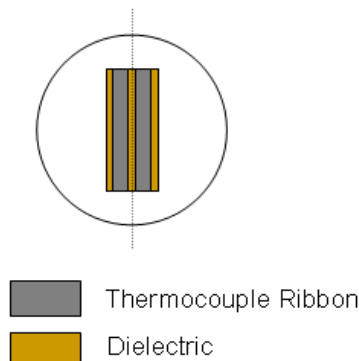
Figure 3.56 NANMAC Corporation self-renewing thermocouples.

We ran into a manufacturing problem of fabricating a void-free block of TPUN-clay and TPUN-CNF materials that are required by NANMAC in order to fabricate self-

renewing thermocouples using our TPUNs. As a result, we were not able to complete this technical task.

3.2 Numerical Progress

As previously noted, the overall goal of this project has been to develop a modeling framework that can be used to design superior ablative materials. The goal was challenging, but the scientific and technological implications of achieving it were significant. The extantiation of the framework is a code whose properties can be readily tied to those easily measured for a particular material system. In the first two years of the project we found that the internal dynamics of the ablator system (namely the chemistry) are extremely important in defining the overall performance of the system. As such, we mostly worked with existing top level (macro-scale) codes such as Chaleur and CMA in exercising the physics of ablation. At the same time, in year 3, we recognized the need to look at lower scale modeling (MD simulations) to test assumptions in our meso-scale model. A challenge for the 3rd year was on which level of modeling top level (essentially modifications to Chaleur) or small scale (more detailed MD simulations) would prove most useful in building out the overall framework.

We chose to expand the work on explicitly tying the small scale to the meso-scale since this had not been done in the literature and represented a much more scientifically important step. At the same time, we were aware of some of the importance of putting forth an ablation code for testing ablation physics for our AFRL colleagues. Fortuitously, in the course of exercising Chaleur (an ITAR code), we recognized that very quickly the ablation rate for fixed external conditions, goes to a steady state. The implication slowly became apparent that we could formulate a significantly simpler quasi-steady state ablation code to use for the top level evaluation process. In the following section, we will discuss the development of these parallel objectives: connection of meso-scale model to atomistic simulations and construction of quasi-steady modeling framework for prediction of steady state recession rates.

3.2.1 Discussion of Top Level Modeling of Ablator

When we have previously presented the conservation laws for ablation, we have generally prescribed the equations in a differential formulation. This is consistent with the presentation in CMA and HERO2D. An alternative presentation uses integral or control volume representations. Chaleur, the SANDIA National Laboratories code, formulates the problem using a control volume representation. For a control volume representation, the choice of the size of the control volume has a major effect on the level of resolution one desires when issuing a prediction. A long tradition of use of so-called integral methods exists in the thermal fluid sciences. Integral methods allow the prediction of engineering level predictions using control volumes that are defined on the largest length scales of the physical problem. In this problem, the engineering level prediction would be of the recession rate. For the ablator problem, the control volume definitions for mass, species, and energy take the form:

$$\frac{d}{dt}\iiint\limits_{CV} \rho\, dV + \iint\limits_{CS} \rho\vec{v}\cdot\vec{n}\, dA = 0$$

$$\frac{d}{dt}\iiint\limits_{CV} \rho Y_i\, dV + \iint\limits_{CS} \rho Y_i \vec{v_i}\cdot\vec{n}\, dA = \iiint\limits_{CV} w_i'''\, dV$$

$$\frac{d}{dt}\iiint\limits_{CV} \sum_{i=1}^{N} \rho Y_i h_i\, dV + \iint\limits_{CS} \sum_{i=1}^{N} \rho Y_i h_i \vec{v}\cdot\vec{n}\, dA = -\iint\limits_{CS} \left(\vec{q}'' + \sum_{i=1}^{N} \rho Y_i h_i \vec{V_i}\right)\cdot\vec{n}\, dA$$

For a control volume that encompasses the ablating surface and that extends far into the virgin material, relatively simple statements can be extracted that yield useful information about the rate of ablation. Further, in the limit of quasi-steady ablation, the unsteady terms become negligible and simple algebraic equations remain to determine the recession rate. For a case in which there are kinetic parameters that are used for the surface ablation processes, we get for the species energy equation:

$$\rho v Y_i + J_i = \dot{m}'' Y_i + \dot{N}_i''$$

Similarly, we arrive at an energy equation of form:

$$q_{conv}'' + \alpha q_{rad}'' + \dot{m}'' h_s^o = s\sigma T_w^4 + \sum_{i=1}^{N} h_i \left(\dot{m}'' Y_i + \dot{N}_i''\right)$$

The global mass balance can be expressed in terms of the char loss rate and the gas blowing rate:

$$\dot{m}'' = \dot{m}_c'' + \dot{m}_g''$$

An alternative formulation of the above equation that shows that details of the virgin and char material must be known is:

$$\dot{m}_g'' = (\rho_v - \rho_c) v$$

Kinetic equations for the char reaction rates and a model for the gas mass evolution process close the system. Possible approaches to dealing with the gas mass evolution include equilibrium approximations. The possibility exists to have the char removal mechanism include a model for mechanical erosion. One might imagine that the aerodynamic shear on the surface and the rate of aluminized particles impacting the surface would provide a loss rate at the interface. The strength of the interface would likely be specified to depend on the elemental composition of the char and a sintering factor that would depend on the temperature rise rate of the char. Simple analytical treatments are available for limiting cases in which, for example, an effective heat of

ablation is defined. For the above formulation, an essential ingredient to predicting meaningful recession rates is the inclusion of reasonably accurate pyrolysis decomposition products. This can be made clearer by considering that the decomposition products provide carbonaceous species that add to the solid carbon at the gas-solid interface. It is also well known that for varying heating rates, the decomposition products differ. These facts again point to the need for better in-depth pyrolysis gas estimation.

3.2.2 Overview of Pyrolysis Modeling Efforts

Traditionally, in ablation modeling, the thermal degradation process has been modeled as a sum of Arrhenius terms [44,45]. When the number or parameters is large, such a model can be easily tuned to fit experimental thermogravimetric (TG) data. However, because this approach is not rooted in the underlying physics of the system, these models are not necessarily reliable in heating regimes outside of the experimental conditions [46]. For many applications, it is necessary to make predictions for heating conditions that are much more extreme (e.g. rocket engine conditions) than are attainable in the laboratory. In order to make reliable predictions in such extreme conditions, we believe that models based on real physical mechanisms should be used.

The widely accepted mechanism for the thermal degradation of thermoplastics is *radical depolymerization* [47]. This mechanism can be modeled mathematically in terms of a system of population balance equations (PBEs) describing the evolution of populations of the various species in the degrading system. A PBE is an integro-differential equation that describes the evolution of a population [48]. In the case of polymer degradation, the relevant population is composed of polymeric chains—alkanes, alkenes, oligomers, radicals, etc. These populations are distributed, in terms of number density, over the chain molecular weights (MWs) or any other relevant *internal variables*. An appropriate PBE for describing the evolution of degrading polymeric MW distributions must account for the various mechanisms by which the number of the various species of a given MW can evolve.

The appropriateness of PBEs in modeling polymer degradation has been recognized since at least the 1950s. Simha, Wall, and Bram [49] present a discrete population-based solution to the problem of determining the number-averaged chain length in a population of polymers that is undergoing free-radical degradation by random initiation. In order to solve the resultant system of equations, the authors linearize the system by assuming a constant radical concentration. In a series of papers, Boyd and Lin present a thorough analysis of theoretical depolymerization kinetics using PBEs under assumptions that the MW distribution is constant with time [50-52]. Using the same PBE model form, Inaba and Kashiwagi [53] find two solutions assuming a steady-state radical concentration. The first solution is an approximate analytical solution that improves on Boyd's work by including the effects of polydispersity in the population. The second solution is a numerical integration of the PBEs discretized into 7000 bins. It was found that under the assumption of a steady-state radical concentration that their approximate approach agreed with the numerical results reasonably well under a variety of conditions.

Recently, several authors have studied a simpler model of degradation in which only a single population of non-radical polymer chains degrades by random chain scission. McCoy and Madras used a continuous PBE model of chain scission to predict the

degradation of polymers in solution [54,55]. Solutions were obtained by transforming the PBE into its moment form. Staggs derived a similar discrete form and solved for special cases of random scission and large initial MW [56-58], for random scission and recombination [59], and for radical depropagation [60]. An even more detailed approach has considered the evolution of populations of alkane, alkene and dialkene species in the degradation of polyethylene and polypropylene [61].

Although PBE modeling of polymer degradation has been studied for quite some time, two difficulties remain. First, the equations are difficult to solve. Second, the model parameters are not easy to determine. We have attempted to address these problems by (1) solving the appropriate PBEs with the quadrature method of moments (QMOM) [62,63] and (2) using optimization (and TG data) and reactive molecular dynamics to estimate the kinetic parameters.

In the next section, we discuss three different models for thermoplastic degradation: (a) first-order Arrhenius model, (b) single-step random chain scission reaction model, and (c) three-step radical depropagation mechanism model. The radical depolymerization mechanism is widely proposed as the mechanism of thermoplastic degradation [48,51-54]. One of our three models is derived directly from chemical equations that describe the radical depropagation mechanism. Our second model (random scission) is based on the possibility that the first step of radical depolymerization (random initiation) described in is the limiting step (i.e. depropagation and termination have much larger time scales). In fact, this is believed to be the case for some thermoplastics such as polyethylene. Two of our models are derived directly from a widely accepted mechanistic description of thermoplastic degradation. The third model, the Arrhenius model, is considered as a control because it is so widely used in the TGA literature. Finally, we discuss incorporating loss (or volatilization) models into a random scission degradation framework.

Solution methods are discussed in Section 3.2.4. Sectional methods use direct numerical integration to evaluate the integral terms in the degradation PBEs. Accurate solution requires fine-grained integration. As a result, sectional methods are computationally expensive but provide the most information of any of the alternative solution methods. Since it is desirable to couple our detailed PBE models of degradation to continuum transport equations, faster methods are required. A second, faster, solution approach is to transform the PBEs into their moment forms. Information is lost in this transformation as the population density functions are represented by a finite number of moments. Section 3.2.4 is concluded with an application of the quadrature method of moments to the solution of a coupled random scission/loss PBE.

The goal of Sections 3.2.7 to 3.2.8 is to estimate the kinetic parameters appearing in the PBEs presented in previous sections. Section 3.2.7 takes the more conventional approach of fitting the model equations to experimental TG data. In contrast to the standard isoconversion methods such as Ozawa-Flynn-Wall, we use sequential quadratic programming (SQP) in an attempt to identify the minimum sum of squared errors (SSE) between the model and the experimental data. In Section 3.2.8, we take a more fundamental approach—using molecular scale simulations to calculate the kinetic parameters for random scission reactions. This approach is more firmly grounded in

underlying physics, but it still involves assumptions that make the analysis computationally tractable.

3.2.3 Models of Polymer Degradation

Polymer degradation due to high incident heat flux is a complex, inhomogeneous physical phenomenon involving interactions between degradation kinetics and transport processes. The degradation process can be complicated by the addition of effectively non-degrading filler fibers or particles that act to alter the diffusion physics. These complexities mean that a detailed understanding of the reaction steps is often unavailable.

For continuum scale problems such as ablation or fire, it is necessary to have an accurate model of the rate at which a thermally decomposing solid loses mass as a function of temperature and relative mass (or density),

$$\frac{dw}{dt} = f(w,T),$$

(1)

where $w(t) = m(t)/m(t=0)$ is the relative mass of the sample. The model f is conventionally determined from a series of thermogravimetric (TG) experiments. In this section, we present three model forms for f. The first of these is the *global Arrhenius* model that has been traditionally used in continuum scale models of polymer degradation. The second two models are PBE-based and are attempts to model the underlying physical mechanism of thermoplastic degradation. It will be seen that the second model presented, *random scission*, is in fact a special case of the more general third model, *radical depolymerization*.

A. Global Arrhenius Model

As mentioned previously, the most commonly applied model of degradation takes the form of a sum of Arrhenius terms. Polymer degradation is fundamentally a chemical reaction in which a polymer chain reacts to form a set of smaller molecules. The Arrhenius equation is accurate in the prediction of the rate constant for a broad range of chemical reactions, it is therefore reasonable, as a first approximation, to use an Arrhenius equation model to predict the mass loss rate of a thermally degrading polymer:

$$\frac{dw}{dt} = -Ag(w)\exp\left(\frac{-E}{RT}\right)$$

(2)

The kinetics are typically characterized by at least three terms: (a) the conversion function, $g(w)$, (b) the pre-exponential term, A, and (c) the activation energy, E. Typically, the conversion function assumes a reaction-order form, $g(w) = w^{\psi}$, where ψ is the order of reaction. For homogeneous reactions, ψ should be a positive integer, but

it is common to let ψ assume fractional forms in order to better approximate data for heterogeneous reactions such as thermal degradation.

Although isoconversion [64,65], or model-free, methods allow for the prediction of a heating rate independent value of activation energy, the value of the pre-exponential is dependent on the assumed conversion function. In short, this model form is arbitrary for complex reactions, and it is therefore unjustified to extrapolate to different degradation environments (e.g. higher heating rates such as experienced in ablation).

B. Random Scission Model

An alternative to the global Arrhenius model is to derive PBEs from physical descriptions of the kinetic degradation mechanism. One simple mechanism is a chain scission that reduces a polymer chain of MW v into two polymer chains with MWs v' and $v\text{-}v'$ [55,56]. Recombination (or polymerization) reactions will be neglected in this description. The random scission model encompasses a family of competing chemical reactions of the form

$$P(v) \xrightarrow{\ K(v,T)\ } P(v') + P(v - v'), \quad v > v' > 0 \tag{3}$$
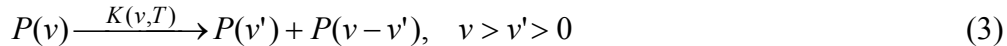
where $P(v)$ denotes a polymer chain of MW v, and $K(v,T)$ is the rate of chain scission for a polymer chain of MW v at temperature T. It is assumed that the rate is independent of the product MWs. The number density of polymer chains of MW v at time t is $p(v,t)$. If chain scission is the only means by which this number density can change, then the time rate of change of $p(v,t)$ is equal to the sum of the rate at which chains of size v are broken and the rate at which chains of size $v'>v$ are divided in such a way that one of the products has MW v. This can be stated mathematically as

$$\frac{\partial p(v,t)}{\partial t} = -K(v,T)p(v,t) + 2\int_{v}^{\infty} K(v',T)p(v',t)\Omega(v,v')dv' \tag{4}$$

where $\Omega(v,v')$ is the scission kernel that accounts for the probability of a chain of MW v' fragmenting into two chains of sizes v and $v'\text{-}v$. McCoy and Wang [66] suggest a functional form of this *normalized stoichiometric kernel* as

$$\Omega(v,v') = \frac{v^{n}(v'-v)^{n}\Gamma(2n+2)}{\Gamma(n+1)^{2}(v')^{2n+1}} \tag{5}$$

where Γ is the gamma function and n is a parameter describing the shape of the scission fragment distribution. For the case of random scission, $n = 0$, and $\Omega(v,v') = 1/v'$. Ziff [67] suggests using $K(v,T) = k(T)v^{\lambda}$ to account for the influence of chain length on scission rate. Under these assumptions, the PBE (equation 4) becomes

$$\frac{\partial p(v,t)}{\partial t} = -k(T)v^\lambda p(v,t) + 2\int_v^\infty k(T)v'^{\lambda-1} p(v',t)dv' . \tag{6}$$

In order to account for the mass loss of the population, some model of volatilization must be included. One simple approach is to assume that all chains with MW less than some critical threshold, v_c, are immediately volatized [57]. This is the model of volatilization that will be used throughout this section. Therefore, the model used is that $p(v,t)$ is the solution to equation 6 for $v > v_c$, and $p(v,t) = 0$ for $v \leq v_c$.

Solutions of equation 6 are related to the number and mass of the population by the zeroth and first moments of the distribution $p(v,t)$. The nth moment of a distribution will be denoted as

$$M_n(t) \equiv \int_0^\infty v^n p(v,t)dv .$$

Frequent use will be made of the normalized moments, $M_n^*(t) \equiv M_n(t)/M_n(t=0)$. Given a solution, $p(v,t)$, to equation 6, the weight fraction can be computed as $w(t) = M_1^*(t)$. In Section 3.2.4, two approaches for solving equation 6 will be discussed. In the next section, a more general model will be presented.

C. Radical Depolymerization Model

The random scission model for polymer degradation given in equation 6 is a special case of the depolymerization mechanism described by Grassie and Scott [47]. It has been observed from experiments (i.e. thermogravimetry (TG), differential scanning calorimetry (DSC), and thermal volatilization analysis (TVA)) that many polymers thermally degrade into smaller molecules of similar structure to the parent molecule. Although the volatile products are similar in chemical structure to the un-degraded polymer, significant differences are observed in volatile fragment sizes. For instance, PMMA degrades to produce the monomer methyl methacrylate and PE degrades into volatile alkanes and alkenes. So while PE seems to produce fragments in a random scission manner, PMMA tends produce mostly monomer products.

Despite this observed difference in volatile products, the thermal degradation of many thermoplastics can be described in terms of a single three-step depolymerization reaction mechanism. The three steps are called *initiation*, *depropagation*, and *termination*. The chemical description of this mechanism is summarized as follows:

1. Initiation

$$P(v) \xrightarrow{K_I} R(v-v') + R(v') \tag{7}$$

2. Depropagation

$$R(v) \xrightarrow{K_D} R(v_1) + R(v-v_1) \tag{8}$$

3. Termination

i) first-order

$$R(v) + X \xrightarrow{K_{t1}} P(v) + X*$$ (9a)

ii) second-order disproportionation

$$R(v) + R(v') \xrightarrow{K_{t2,d}} P(v) + P(v')$$ (9b)

iii) second-order recombination

$$R(v-v') + R(v') \xrightarrow{K_{t2,r}} P(v)$$ (9c)

In the preceding reactions, $R(v)$ denotes a radical chain of MW v, $X*$ is a non-polymeric radical, and v_1 is the MW of a monomer.

Mathematically modeling the depolymerization process requires two PBEs, one for the population of non-radical polymer chains and one for the population of radical chain molecules. For the case of only first-order termination, the two PBEs are

$$\frac{dp_v}{dt} = K_{t1} r_v - K_I p_v, \quad v > v_c$$ (10a)

$$\frac{dr_v}{dt} = 2 \int_v^\infty K_I p_{v'} \Omega dv' + \int_v^\infty K_D r_{v'} \delta[v - (v' - v_1)] dv'$$
$$- K_D r_v - K_{t1} r_v, \quad v > v_c$$ (10b)

where the explicit dependence on time has been dropped and the notation p_v is shorthand for $p(v)$. Equation 10a states that the rate of change of the number of polymer chains is equal to the sum of creation due to termination and loss due to initiation. Equation 10b states that the rate of change of the number of radical chains is equal to the sum of (1) creation due to initiation, (2) creation due to depropagation, (3) loss due to depropagation, and (4) loss due to termination. Again, it is assumed that all molecules smaller than v_c are volatized.

As with the case of random scission, several assumptions can be made about the forms of the rate constants as well as the scission kernel. In particular, it is again assumed that $K_I(v,T) = k_I(T)v^\lambda$ and $\Omega(v', v - v') = 1/v'$. Additionally, it is reasonable to assume that the depropagation and termination rates are independent of MW. That is, $K_{t1}(v,T) = k_{t1}(T)$ and $K_D(v,T) = k_D(T)$. Under these assumptions, the PBEs for radical depropagation are

$$\frac{dp_v}{dt} = k_{t1} r_v - k_I p_v, \quad v > v_c$$ (11a)

77

$$\frac{dr_v}{dt} = 2\int_v^\infty k_I v'^{\lambda-1} p_{v'} dv' + \int_v^\infty k_D r_{v'} \delta[v - (v'-v_1)] dv'$$
$$- k_D r_v - k_{t1} r_v, \quad v > v_c \tag{11b}$$

The solution of equations 11 is related to the mass loss problem through the first moments of the distributions p_v and r_v—these moments will be denoted $M_{p,1}$ and $M_{r,1}$, respectively. Therefore, the non-dimensional mass of interest is

$$w(t) = M_1^*(t) \equiv \frac{M_{p,1}(t) + M_{r,1}(t)}{m(t=0)} . \tag{12}$$

D. Improved Loss Models

For some polymers, such as polyethylene, it is observed that the first step is rate limiting. In this section, we introduce more sophisticated loss models into the random scission population balance, equation 4. Additionally, the scission kernel and random scission term are studied in greater detail. The resultant governing equation depends upon three parameters: the rate at which bonds are broken, the relative proportions of the resultant chain products, and the rate at which the chains are volatilized. We discuss models for these three parameters, and then explore the consequences of varying the parameters of these sub-models.

As a first step towards predicting the thermal degradation of a thermoplastic it is useful to study a spatially lumped problem such as typically occurs thermogravimetry (TG). In TG, a furnace heats a small sample (~10 mg) of thermally degradable material at a controlled heating rate—usually a constant heating rate or isothermal. As the molecules of the sample decompose chemically, some of the products become small enough to volatilize thus decreasing the total mass of the sample. The sample is contained in an open metallic pan attached to a scale so that mass can be measured as a function of time. Since the purpose of TG is to better understand pyrolysis kinetics, the experiment is usually conducted in an inert environment.

The goal of this study is to develop a modeling framework for predicting the results of TG experiments. This requires computing the normalized mass loss curve, $w(t) = m(t)/m(t=0)$.

Because of the small sample size, the degrading system has a small Biot number and can be considered thermally lumped. Although less justifiable, the model developed below will also assume that the TG system is lumped with regards to mass transfer. That is, the molecular distribution is the same at any location within the pan. Under these assumptions, the only relevant physical processes are *chemical decomposition* and *volatilization*.

Polymer molecules can be thought of as notional chains of continuously varying molecular weight (MW). Chemical decomposition will be modeled as a single-step scission reaction as in equation 7. Volatilization can be thought of as a reaction like

$$P_c(v) \xrightarrow{\quad L(v,T) \quad} P_g(v) \tag{13}$$

where P_c is a molecule in the condensed phase and P_g is a molecule in the gas phase. For our purposes, it is not important to trace the evolution of the gas phase molecules. We shall derive a governing equation for TGA experiments, in the form of a PBE, under the assumption that all relevant physics are described by equations 7 and 13.

A population balance approach allows one to predict the evolution of a large number of entities (in our case, polymer chains) based upon assumptions about the microscale physics of the individual entities. For our problem, the population of interest is of polymer chains of MW v. This population is fully characterized by the chain number density function, $p(v;t) = p_v$ with units mol^2/kg. The number of chains in the population with MWs in the infinitesimal interval $[v, v + dv]$ equals $p_v dv$. The number density function can be related to quantities of interest through its moments. The mass of the sample, for instance, is $m(t) = M_1(t)$.

A population balance is constructed by equating the rate of change in p_v with the sum of the rates at which chains of MW v are lost or gained. From equations 7 and 13, chains of MW v are lost through scission and volatilization. Additionally, chains of MW v are created through the scission of larger chains. It can be shown that the appropriate PBE for our zeroth-order TG problem is

$$\frac{\partial p_v}{\partial t} = -[K(v) + L(v)]p_v + 2\int_v^\infty K(v')p_{v'}\Omega(v,v')dv', \tag{14}$$
$$\forall v > 0,$$

The first term of equation 4 accounts for the loss of chains of MW v due to scission and volatilization. The second term is the summation of the rates at which larger chains produce chains of MW v. Solutions of equation 14 require the specification of an initial number density function, $p_v(t=0)$.

Most real models of K, L, and Ω make analytical solutions of equation 4 impossible. It is often necessary to transform the PBE into its equivalent moment form by applying the moment operator. The moment form will be a system of unclosed ordinary differential equations. The system of equations is closed using the quadrature method of moments (QMOM). The closed system is then used to predict the time evolution of the first moment of the chain number density function, and this is all that is needed to predict the desired TG curve, $w(t) = M_1(t)/M_1(t=0)$. Before this process can be completed we must first describe models for K, L, and Ω.

E. Submodels

Several scission models have been suggested in the literature. A general approach is a polynomial form [71],

$$K(v,T) = \sum_{j=0}^{m} k_j(T)v^j .$$ (15)

The temperature dependent terms are assumed to have Arrhenius forms.

A special case of equation 15 that has been used frequently in polymer degradation [68] is the power law,

$$K(v,T) = k(T)v^{\kappa} = A_k v^{\kappa} \exp\left(\frac{-E_k}{RT}\right)$$ (16)

Typically, κ is taken to be one—implying that all bonds break at the same rate. That is, since longer chains have more bonds, longer chains will break more frequently than smaller chains.

Recent work in reactive molecular dynamics (RMD) suggests that bonds in long molecules actually break faster than bonds in shorter molecules [74]. It seems that the most appropriate model would be a rate that rapidly increases for chains smaller than around 10 monomers and then increases linearly with v as in equation 16 with $\kappa = 1$. The appropriate model form would be like

$$K(v,T) = k(T)v + K_0(T)\left[1 - \exp(-Cv)\right].$$ (17)

In the previous section, the scission kernel was modeled as a symmetric beta distribution scaled to the interval [0,v']

$$\Omega(v,v';\alpha) = \frac{\Gamma(2\alpha)}{\Gamma^2(\alpha)} \frac{v^{\alpha-1}(v'-v)^{\alpha-1}}{(v')^{2\alpha-1}}$$ (18)

where Γ is the gamma function. The justification for this assumption is two-fold. First, the stoichiometric kernel should be symmetric since the linear polymer chains are physically symmetric. Second, the beta distribution is very versatile—varying α from 1 to ∞ corresponds to a family of distributions from the uniform to the Dirac delta. This versatility is demonstrated in Figure 3.57 where $v^* = v/v'$ and the kernel has been normalized accordingly.

Using a model based on transition state theory (TST), it has been suggested [68] that $\alpha = 3/2$ corresponding to a semicircular distribution. We will use this as a nominal value in following sections.
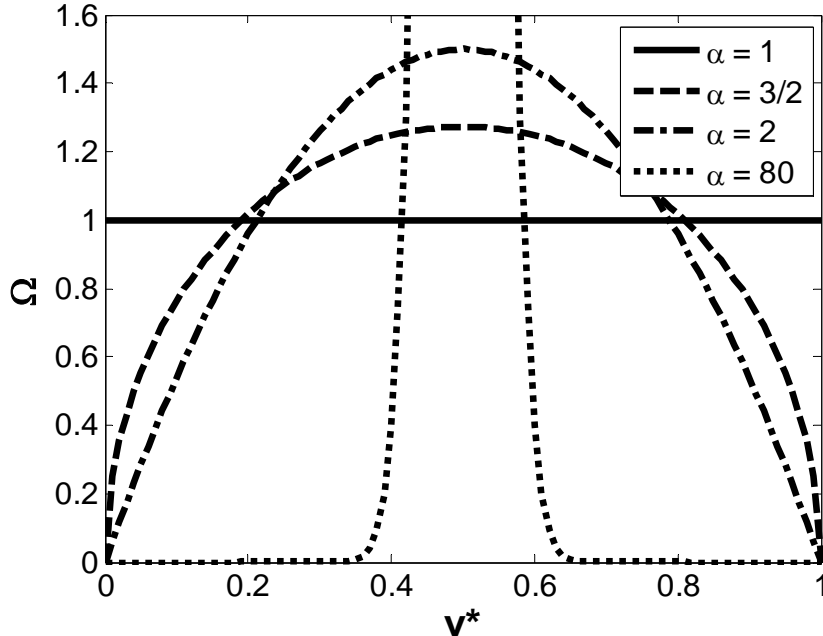
Figure 3.57 Various stoichiometric kernels.

Finally, in order to produce predictions from equation 14, it is necessary to choose a model for $L(v,T)$. The PBE is zeroth-order meaning that the population of chains is identically distributed at the surface as in-depth. This is likely not a valid assumption, since the time scales for polymer diffusion are relatively small. However, this assumption allows us to treat mass loss as a purely convective process, where $\dot{m} = h_m A_S (C_S - C_\infty)$. First, for inert gas phase environments such as are found in typical TG experiments, it can be assumed that $C_\infty \to 0$. Thus, $\dot{m}(v,T) \propto h_m(v,T)p_v$. Second, the mass transfer coefficient will increase with temperature and decrease with MW. Assuming an Arrhenius type dependence on temperature, we propose,

$$L(v,T) = \frac{l(T)}{v^\lambda} = \frac{A_l}{v^\lambda} \exp\left(\frac{-E_l}{RT}\right). \tag{19}$$

where equation 16 is an improvement over past approaches in which mass loss was accounted for by simply truncating the number density function below some critical MW of volatilization, v_c [57,69]. That is, $p_v = 0$ for $v \le v_c$.

The moment equations show that the mass loss rate is dependent on the shape of the scission kernel only implicitly through its dependence on higher order moments. In fact, it turns out that any influence that α might have on w is in fact very small.

In the next section, we will assume that the degradation physics can be described by equation 14 and the sub-models of equations 16, 18, and 19. An exact solution of this system of equations is not known. Two broad categories of numerical approaches are sectional methods [70] and moment methods. Because of the high computational cost of sectional methods, we will follow the second approach. In the next section, we will discuss solution methods for the various modeling equations presented in this section.

3.2.4 Solution Methods

Three models of polymer degradation were presented in the previous section. The solution of the global Arrhenius model (equation 2) is relatively straightforward; it requires the numerical integration of a single ODE with the initial condition $w(t = 0) = 1$. This integration becomes increasingly slow for fast kinetics, but most materials have sufficiently slow kinetics that simulation is not difficult. All integration in this study has been performed using Gear's method.

The solution of the population balance equations (PBEs) is significantly more difficult than the integration of the Arrhenius equation. In this section, we present two approaches for solving equations 6 and 11. The first approach is generally classified under the name *sectional methods*. Sectional methods allow for the simulation of the evolution of the *entire* population density profile(s) over time. This high degree of information is obtained at high computational cost, however. The second approach presented in this section is a means of circumventing large computational expenditures by restricting the simulation to a finite number of moments describing the population density profile. So-called *moment methods* are, at present, necessary if the PBE models of degradation are to be coupled with continuum scale models of ablation or fire.

A. Sectional Methods

An obvious sectional approach for solving the PBEs is to simply use a finite-difference expression for the derivative terms, and a midpoint rule integration to compute the integral terms. For example, the PBE for a simple random scission model with constant rate K is

$$\frac{dp_v}{dt} = -kvp_v + 2\int_v^\infty kp_{v'}dv' .$$

(20)

Using this straightforward approach, the discretized form of the equation is

$$p_{j+1,i} = p_{j,i} + \Delta t\left[-kp_{j,i}v_i + 2k\sum_{k=i}^{N-1}p_{j,k}\Delta v\right].$$

(21)

Experience shows that such an approach is insufficient and produces a solution in which mass is not conserved. This indicates that the midpoint quadrature is not sufficiently accurate to fully resolve the integral term it approximates.

In order to overcome this difficulty, many integration schemes have been proposed. We implement the approach suggested by Hu, Rohani, and Jutan [70]. This approach uses a Gauss-Legendre quadrature rule to evaluate the integral terms in the PBE. Specifically, the equation above would be evaluated as

$$p_{j+1,i} = p_{j,i} + \Delta t \left[-kp_{j,i} v_{j,i} + 2k \sum_{k=i}^{N-1} \int_{v_k}^{v_{k+1}} p(v') dv' \right] \tag{22}$$

where the integral term in each bin is evaluated as

$$\int_{v_k}^{v_{k+1}} p(v') dv' \approx \frac{v_{k+1} - v_k}{2} \sum_{i=1}^{N} w_{N,i} \widetilde{p} \left(\frac{v_{k+1} + v_k}{2} + \frac{v_{k+1} - v_k}{2} z_{N,i} \right). \tag{23}$$

The number $z_{N,i}$ is the ith Gaussian abscissa for an N-point quadrature. Hu et al. [70] suggest using a cubic spline interpolation on the points $(p_{j,i}, v_{j,i})$ to find $\widetilde{p}$.

B. Moment Methods

Any density distribution function can be modeled in terms of its moments. Although it is impossible to compute the infinite number of moments necessary to fully characterize a distribution, a small number of moments is often sufficient for modeling many systems of interest. The problem of computing $w(t)$ for a thermally degrading polymer requires knowledge of the first moment(s) of the chain distribution(s).

C. Random Scission

The moment form of equation 6 is derived by applying the mathematical definition of a moment of order n to the system. For our analysis, we make the simplifying assumption that there is some critical MW, v_c, below which the molecules are instantaneously volatized and mass is lost from the system. This approach has been applied previously by Staggs [56], and is a reasonable approximation to reality in the case of a small sample in which transport (or spatial) effects are negligible. Under this assumption, the MW distribution is truncated such that $p(v \leq v_C) = 0$. As a result, the moment equations are obtained by integrating from v_c to infinity rather than zero to infinity. The final form of these equations is

$$\frac{dM_n}{dt} = k \left[\left(\frac{2}{n+1} - 1 \right) M_{n+\lambda} - \frac{2v_C^{n+1}}{n+1} M_{\lambda-1} \right] \tag{24}$$

Madras, Chung, Smith, and McCoy [71] argue that the dependence of scission rate on MW is a linear function for a broad range of v for many polymers. Therefore, it is reasonable to assume $\lambda = 1$. The first two moments are thus

$$\frac{dM_0}{dt} = k(M_1 - 2v_C M_0) \tag{25a}$$

$$\frac{dM_1}{dt} = -kv_C^2 M_0 \tag{25b}$$

where the initial conditions $M_0(t=0)$ and $M_1(t=0)$ are determined by integration over the initial distribution of polymer chains, $p(v, t=0)$. For a constant mass system, $dM_1/dt = 0$ and $dM_0/dt = kM_1$. The sink terms in equations 25 are due to the introduction of a critical MW of volatization, v_C. A large value of v_C allows for more molecules to volatize and thus faster rates of mass and number loss. Furthermore, the average MW of the lost molecules is found to be $(-kv_C^2 M_0)/(2v_C M_0) = \frac{1}{2}v_C$. It should be noted that these equations take a similar form to equations 12 in [62]; the difference between the two pairs of equations being an additional term in each due to random recombination.

Equations 25 can be solved analytically for the case of isothermal degradation. The solution can be carried out in terms of the number-averaged MW, $\bar{v}$, as follows. Recognizing that

$$\frac{d\bar{v}}{dt} = \frac{d(M_1/M_0)}{dt} = \frac{1}{M_0}\frac{dM_1}{dt} - \frac{M_1}{M_0^2}\frac{dM_0}{dt}, \tag{26}$$

Substituting equations 25 into the right-hand side yields an equation for the time evolution of $\bar{v}$:

$$\frac{d\bar{v}}{dt} = -k(\bar{v}^2 - 2v_C\bar{v} + v_C^2). \tag{27}$$

For the isothermal case, k is constant with time, and the integration of equation 27 results in an explicit expression for the number-averaged MW as a function of time

$$\bar{v}(t) = v_C + \left[kt + \frac{1}{\bar{v}_i - v_C}\right]^{-1} \tag{28}$$

where $\bar{v}_i$ is the initial average MW of the population. Equation 28 shows a $1/t$ dependence of MW on time. Also, as $t \to \infty$, the number-averaged MW approaches the critical MW of vaporization. In other words, at large times, the only remaining molecules will be infinitesimally close in size to the critical MW.

Finally, in order to obtain the isothermal dependence of weight fraction on time, equation 28 is substituted into equation 25b. The resultant equation can be integrated to obtain an analytical solution for mass loss

$$w(t) = \left[\frac{kv_c}{\bar{v}_i} (\bar{v}_i - v_C)t + 1 \right] \cdot \exp(-kv_C t). \tag{29}$$

D. Radical Depolymerization

A similar process is used to transform the PBEs describing radical depolymerization, equations 11, into a small set of ODEs describing the evolution of the moments of the polymer and radical polymer chains. Applying the definition of the nth moment, and again switching the orders of integration gives

$$\frac{dM_{P,n}}{dt} = k_{t1} M_{R,n} - k_I M_{P,n+\lambda} \tag{30a}$$

$$\frac{dM_{R,n}}{dt} = \frac{2k_I}{n+1} \left(M_{P,n+\lambda} - v_C^{n+1} M_{P,\lambda-1} \right) + k_D \sum_{j=0}^{n} \binom{n}{j} (-v_1)^{n-j} M_{R,j} - \left(k_D + k_{t1} \right) M_{R,n} \tag{30b}$$

where $M_{P,n}$ is the nth-moment of the non-radical polymer chain population, and $M_{R,n}$ is the nth-moment of the radical population. The moment equations can be closed by assuming that $\lambda = 1$ and using a one-point Gaussian quadrature [62] such that

$$M_{2,x} = \int v^2 x(v) dv = M_{0,x} \hat{v}^2 = \frac{M_{1,x}^2}{M_0}. \tag{31}$$

Making these approximations, a closed set of moment equations in terms of the first two moments is found to be

$$\frac{dM_{P,0}}{dt} = k_{t1} M_{R,0} - k_I M_{P,1} \tag{32a}$$

$$\frac{dM_{P,1}}{dt} = k_{t1} M_{R,1} - k_I \frac{M_{P,1}^2}{M_{P,0}} \tag{32b}$$

85

$$\frac{dM_{R,0}}{dt} = 2k_I \left(M_{P,1} - v_C M_{P,0} \right) - k_{t1} M_{R,0} \tag{32c}$$

$$\frac{dM_{R,1}}{dt} = k_I \left(\frac{M_{P,1}^2}{M_{P,0}} - v_C^2 M_{P,0} \right) - k_D v_1 M_{R,0} - k_{t1} M_{R,1} \tag{32d}$$

Equations 32 can be numerically integrated to find the evolution of the first two moments of the polymer and radical populations.

The models expressed in equations 32 (as well as the random scission models in equations 25) contain two types of parameters. The first type is molecular weights; specifically, the critical MW of volatilization, v_c, and the MW of a single mer unit, v_1. The MW of a single mer unit is always known, and v_c can be either measured by thermal volatilization analysis (TVA) [46] or thermodynamic analysis [72]. The other type of model parameters is reaction rates: k_I, k_D, and k_t. In all of the following simulations and analysis, it is assumed that these reaction rates assume an Arrhenius form, $k = A \exp(-E/RT)$. Thus the dimensionality of the parameter space for the model represented by equations 32 is increased from 4 to 7 (excluding the known v_1). Similarly, the parameter space of the random scission model in equations 25 is of dimension three.

Equations 32 were simulated for the case of a high density polyethylene (PE) [73] of initial weight-averaged MW of 22 kg/mol undergoing isothermal degradation at a temperature of 400ºC. It was assumed that the rate coefficients were equal for all three reaction steps with $A = 2e14$ s^{-1} and $E = 200$ kJ/mol. The results of the first two moments are plotted in Figure 3.58. In these simulations, it was assumed arbitrarily that the critical chain length of volatization was 10 mer units. These model parameters were chosen arbitrarily (within reasonable limits) in order to demonstrate a possible population evolution and for numerical verification of the model. In the next section, we will use an optimization algorithm to estimate physically meaningful approximations for these parameters. Note that in the plot of the first moments, mass is initially rapidly transferred to a population of radicals. The time over which this occurs is much less than what can be seen in this graph. As the unzipping process proceeds, mass is transferred back to the non-radical polymer chains. The total mass, as expected, proceeds monotonically to zero.
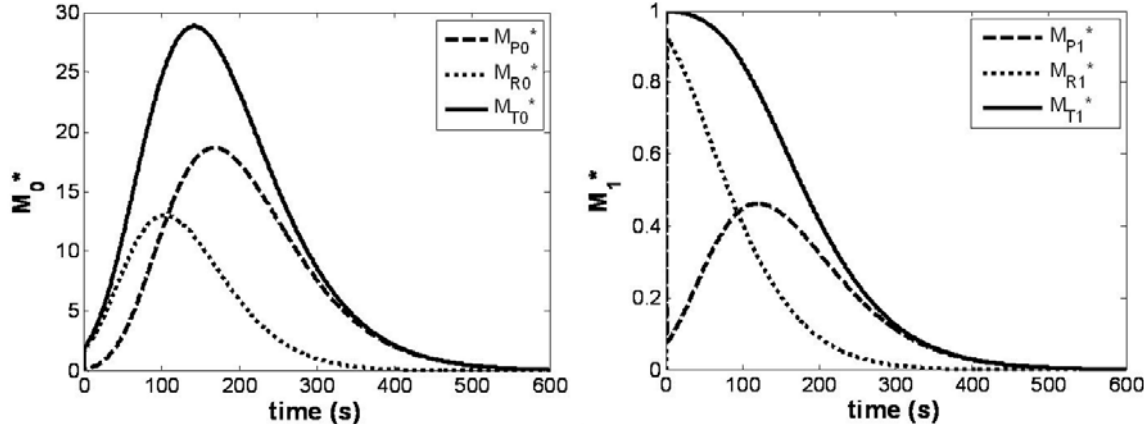
Figure 3.58 Radical depolymerization simulation of isothermal degradation of PE at T_c = 400°C. Evolution of normalized numbers (left) and evolution of normalized mass (right).

In Section 3.2.5, the moment models will be compared to a direct simulation of the underlying population balance equations.

E. Moment Closure using QMOM

Applying the moment operator to equation 14 (with equations 16, 18, and 19), the following equation is obtained after some manipulation

$$\frac{dM_n}{dt} = C_n(\alpha)k(T)M_{n+\kappa} - l(T)M_{n-\lambda} \tag{33}$$

where $C_n(\alpha) = 2M_{n,BE}(\alpha) - 1$ and $M_{n,BE}(\alpha)$ is the nth-moment of the symmetric beta distribution. These moments can be computed using

$$M_{n,BE}(\alpha) = \frac{B(\alpha+n,\alpha)}{B(\alpha,\alpha)} \tag{34}$$

where B denotes the beta function. For $n = 0$, $M_{n,BE}(\alpha) = 1$, and the right-hand side of equation 33 becomes positive in the absence of the volatilization term. Thus the 0th-moment (number of chains) increases with time. For $n = 1$, $M_{n,BE}(\alpha) = 1/2$, and the right-hand side of equation 10 is then identically zero in the absence of the volatilization term. Thus the 1st-moment (mass) is conserved. Also, note that for these two equations there is no explicit dependence on α.

The initial conditions for equations 33 are the moments of the initial number density function. Equations 33 suffer from a closure problem unless $\kappa = \lambda = 0$. Based on the underlying models, this is not a realistic scenario, and so the problem remains unclosed.

One approach for obtaining closure is the quadrature method of moments (QMOM) [74-76]. The underlying idea of QMOM is to approximate the moment integrals using Gaussian quadrature

$$M_n = \int_0^\infty v^n p_v dv \approx \sum_{i=1}^{N_Q} \hat{v}_i^n W_i \ . \tag{35}$$

The right-hand side of equation 35 contains $2N_Q$ unknowns. Therefore, a set of quadrature points, $\{(\hat{v}, W)_i\}$ can be obtained from a sequence of $2N_Q$ moments. These quadrature points can then be used to obtain unknown moments and other integral terms.

Applying quadrature approximations to the unclosed moments in equations 33 we obtain

$$\frac{dM_n}{dt} = C_n(\alpha)k(T)\sum_{i=1}^{N_Q} \hat{v}_i^{n+\kappa} W_i - l(T)\sum_{i=1}^{N_Q} \hat{v}_i^{n-\lambda} W_i \ . \tag{36}$$

By choosing a sequence of $2N_Q$ moments, this sequence can be evolved using equations 36, and equations 35 are used to find the quadrature points at each time step.

For the purpose of simulating TGA experiments, we are interested in the 0th and 1st – moments of the number density function. Thus it is necessary that the moment sequence chosen contain at least these two moments.

3.2.5 Verification of Moment Equations

The moment models for random scission and radical depolymerization, as expressed in equations 25 and equation 32, are approximations of the PBE models expressed in equation 6 and equations 11. In this section, the validity of this approximation will be tested by comparing solutions of the moment equations with direct solutions of the PBEs found using the sectional approach outlined previously.

Verification was performed by comparing the sectional solution with the moment solution for the isothermal degradation of the PE used previously [73]. Because the sectional method is much more computationally expensive, the simulations were limited in time to 100 seconds for the random scission model and only 12 seconds for the radical depolymerization model. The results of these comparisons are presented in Figures 3.59 to 3.61. On average, the sectional solutions were on the order of 100 times slower.
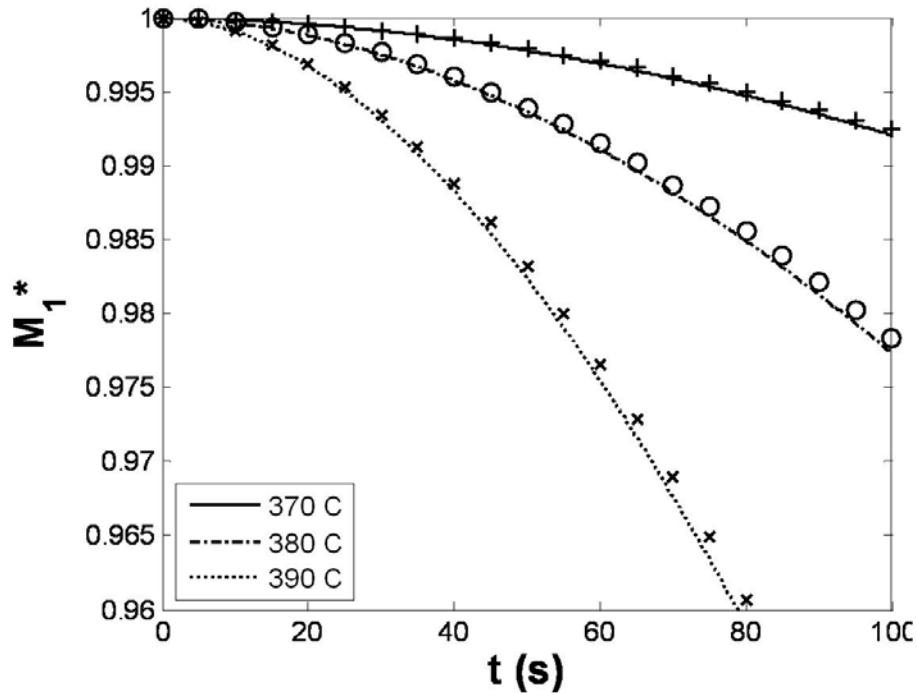
**Figure 3.59** Verification of random scission first moment model by comparison with a sectional solution for PE at 370ºC.
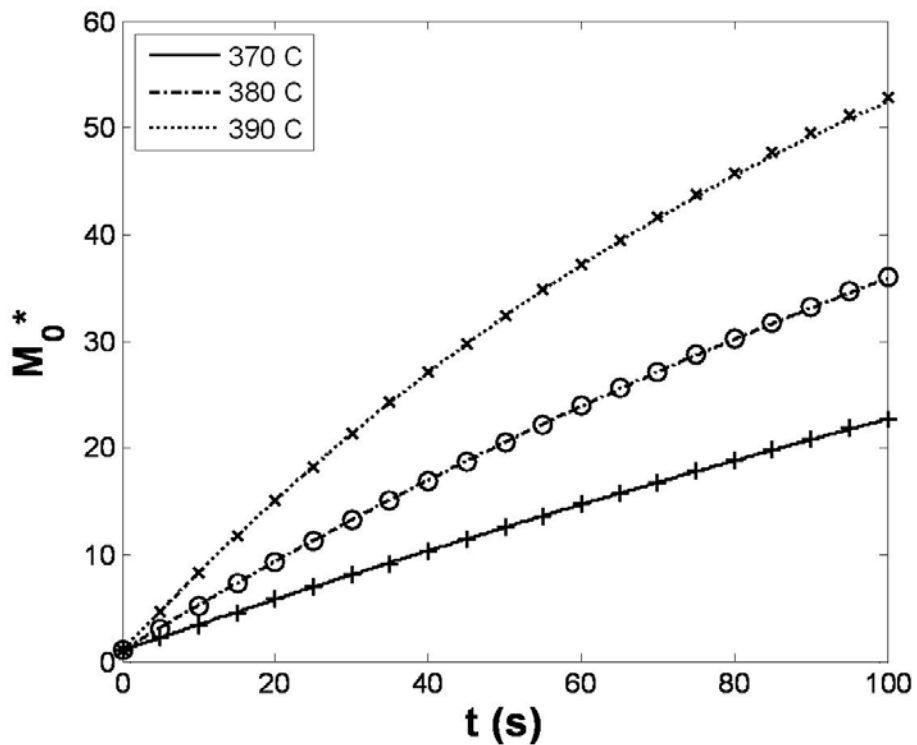

Figure 3.60 Verification of random scission zeroth moment model by comparison with a sectional solution for PE at 370ºC.
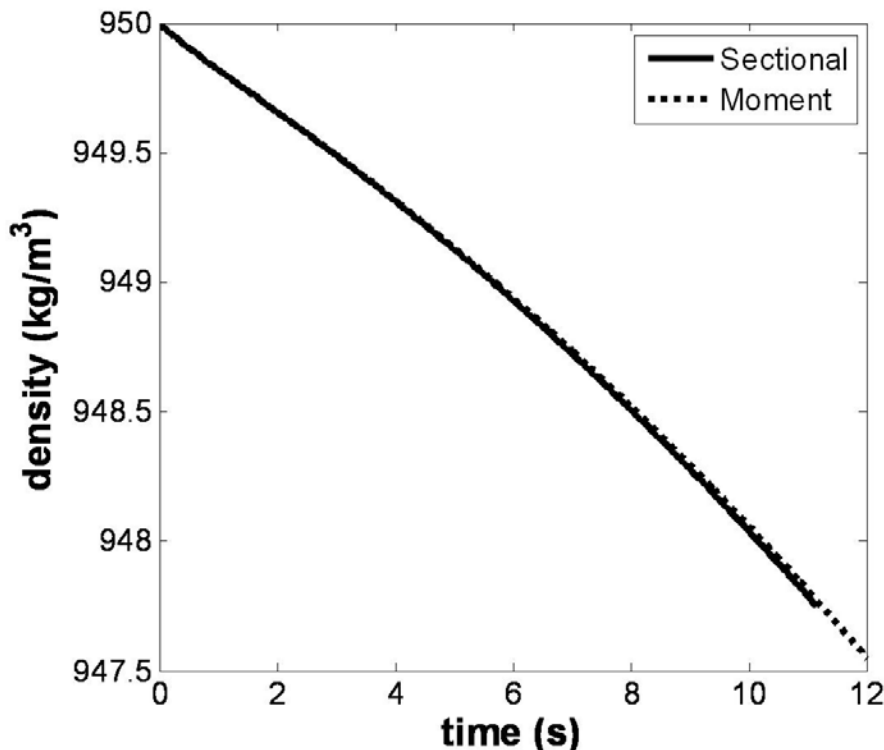
Figure 3.61 Verification of radical depolymerization moment model by comparison with sectional method for PE at 400°C.

Both moments for the random scission model are presented. It was found that the sectional solution became arbitrarily close to the moment solution as the sectional time step was decreased.

The sectional solution of the radical depolymerization model was much more expensive computationally. The density losses of the sample are plotted in Figure 3.62. The sectional and moment solutions agree well for the first 11 seconds of degradation. The density at larger times was not computed due to the expense of the sectional simulations.

Up to this point, arbitrary kinetic parameters (e.g. A and E) have been assumed. Although these values fall within the range of the kinetic compensation line for PE [75], more precise estimates of these parameters are desirable. In Sections 3.2.7 and 3.2.8, estimates of the parameters in equations 25 and equations 32 are obtained optimization routine to minimize the sum of squared errors between the moment based models and TG data and reactive molecular dynamics.

3.2.6 Sensitivity Study with Loss Models

We will now study some of the consequences of equations 33. In order to compute numerical results, we assume $\kappa = 1$ and $\lambda = 2$. The value of $\kappa = 1$ is a standard assumption as was discussed above, and the value of $\lambda = 2$ was chosen to prevent the volatilization of large molecules at high temperatures. We will use a two-point quadrature, and advance the first four moments: M_0, M_1, M_2, and M_3. Finally, we assume

an initial average MW of 22 kg/mol [73] and a variance of 0.8. In order to compute the initial moments, we assume that the initial chain number density function is distributed according to a lognormal distribution. The distribution was normalized such that $M_0 = 1$ mol and therefore $M_1 = 22$ kg. This normalization is just for convenience and will not affect the results for the quantity of interest because the problem is assumed to be spatially lumped—that is, size is unimportant. A plot of the initial distribution is given in Figure 3.62.
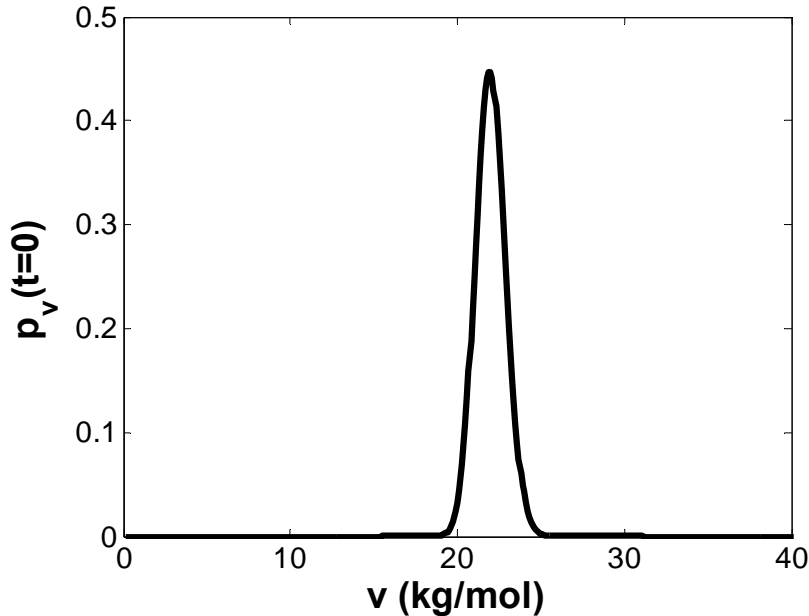

Figure 3.62 Initial number density function.

The experimental conditions were chosen to be isothermal so that the number of model parameters would be minimized. In particular, for isothermal degradation, equations 33 involve only three parameters: *l*, *k*, and α. Nominal values for these parameters were chosen as follows. First, we chose to simulate at an operating condition of *T* = 420 ºC so that qualitative comparisons could be made with experimental data available in [73]. Second, a nominal value of *k* was computed from typical values of A_k and E_k for polyethylene degradation kinetics. Due to the so-called kinetic compensation effect, a range of values for *A* and *E* are acceptable provided that they lie on the kinetic compensation line of the material [75]. Using representative values, we find that $\widetilde{k} = 1.43\text{e-}4 \text{ s}^{-1}$. We then simulated and found that $w(t; \widetilde{k}, \widetilde{l} = \widetilde{k}, \widetilde{\alpha} = 3/2)$ approximately matched the experimental data in [73].

The first parameter tested was α—the shape parameter for the scission kernel. Four TGA curves were produced at $\alpha = (1, 3/2, 2, 80)$ with constant $k = \widetilde{k}$ and $l = \widetilde{l}$. These curves are plotted in Figure 3.63. It is observed, as was expected that the shape of the

scission kernel has little influence on the mass loss rate. This makes sense because we have assumed that scission rate is independent MW.
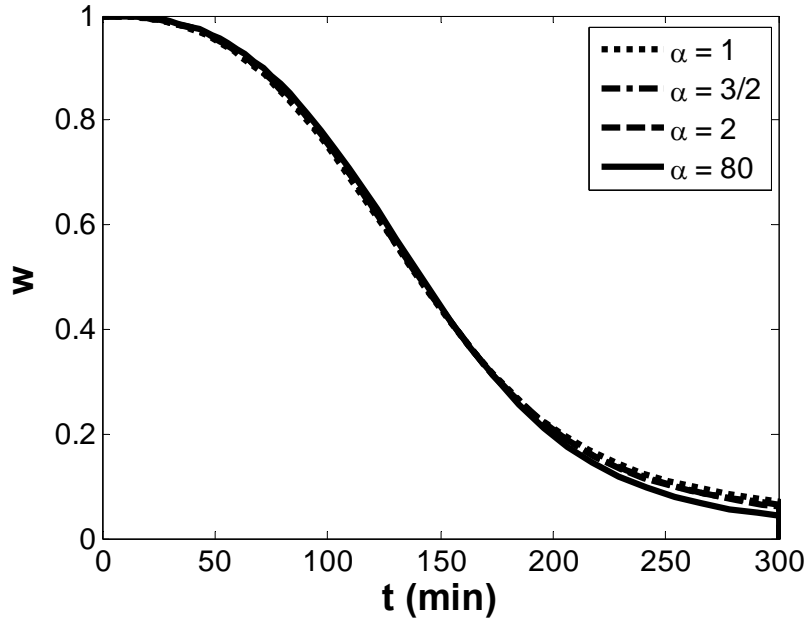
Figure 3.63 Isothermal TGA curves for varying α.

Next, we studied the effects of varying the scission and volatilization rates. First, with $l = \widetilde{l}$, w was simulated with values of $k = \widetilde{k} \times (0.1, 1, 10, 100)$. The resultant isothermal TGA curves are plotted in Figure 3.64. Second, with $k = \widetilde{k}$, w was simulated with values of $l = \widetilde{l} \times (0.1, 1, 10, 100)$. The resultant isothermal TGA curves are plotted in Figure 3.65. Of course mass is lost faster with both increasing k and increasing l, but it is seen that in these operating conditions and under these modeling assumptions mass loss is more sensitive to the scission rate. It is expected that the relative importance of k to l will vary strongly with the models of K and L.
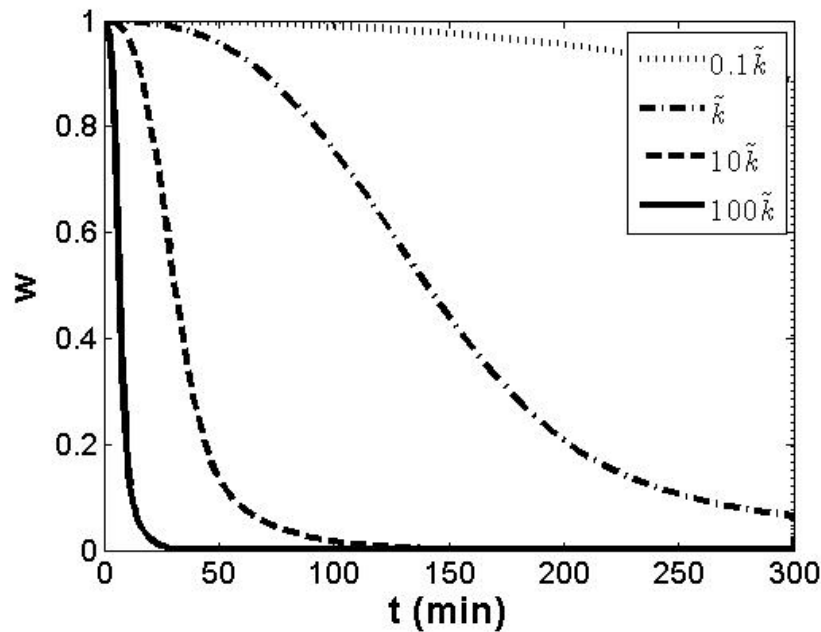
Figure 3.64 Isothermal TGA curves for varying k.
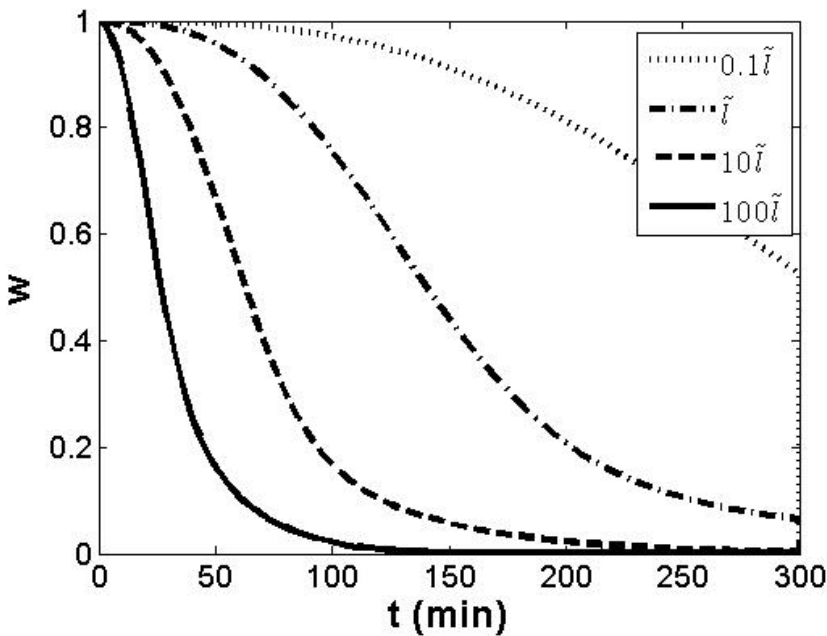
Figure 3.65 Isothermal TGA curves for varying l.

It is apparent that, for this material, at $T = 420$ ºC, that the TGA curve is more sensitive to the scission rate, k, than it is to the volatilization rate, l. Future work is needed to use this modeling framework for thermal degradation problems. In particular, we intend to study the effects of using more realistic models for K (such as equation 17) and L. Also, the numerical convergence needs to be studied in order to verify the approach presented.

93

3.2.7 Optimization to Find Kinetic Parameters

The advantage of using PBE based models of polymer degradation is that such models are developed from descriptions of the underlying reaction mechanism. Therefore, these models should perform well under all operating conditions (i.e. heating rates), unlike *ad hoc* global models such as sums of Arrhenius terms. Also, it is possible (at least in principle) to use atomistic results as inputs to these models in order to predict continuum scale behavior. Specifically, molecular scale models of polymer chains can be simulated to predict the kinetic parameters in the PBE models described above. Although there are promising means of determining these kinetic parameters (e.g. reactive molecular dynamics [76,77]), in the absence of such methods it is necessary to devise other approaches for identifying these parameters. In this section, the PBE models are fitted to experimental data for PE and PMMA using optimization to minimize the sum of squared errors.

3.2.8 Statement of the Problem

The optimization problem is to minimize the sum of squared errors computed as

$$E_2 = \sum_i \left(w_{e,i} - w(T_i, \mathbf{K})\right)^2 \tag{37}$$

where $w_{e,i}$ are the weights from dynamic TG experiments and w is the weight fraction predicted by the model at the temperatures T_i of the experimental data points and with the vector of kinetic parameters $\mathbf{K}$. The goal is to find the values of $\mathbf{K} = \mathbf{K}^*$ that minimize E_2. Since the elements of $\mathbf{K}$ are either pre-exponentials, activation energies, reaction orders, or critical number of monomer units the solution is constrained to be a vector of positive reals. Solutions were found using sequential quadratic programming.

The process was completed for two materials: polyethylene and poly(methyl methacrylate). For each material, three model forms were tried in the optimization algorithm: a single-step Arrhenius model, the random scission model of equations 25, and the radical depolymerization model of equations 32. The parameter spaces for these three models are defined by the vectors

$$\mathbf{K}_{Arr.} = [A, E, \psi]^T \tag{38a}$$

$$\mathbf{K}_{Rand.Sci.} = [A, E, v_C]^T \tag{38b}$$

$$\mathbf{K}_{Rad.Dep.} = [A_I, E_I, A_D, E_D, A_t, E_t, v_C]^T \tag{38c}$$

Since all three models include Arrhenius terms, the integration requires small time steps for fast reactions (or large A and small E). Fortunately, it was found that fast kinetic parameters do not match experimental data for the Arrhenius and random scission models. However, the radical depolymerization model includes three reactions which

can occur at vastly different rates making the system stiff. Gear's method is particularly well suited to the integration of stiff systems of equations.

Another general difficulty in finding "optimum" kinetic parameters is the so-called *kinetic compensation* effect [46]. That is, roughly the same TGA trace can be generated by simultaneously increasing the values of A and E for a given reaction. Ceamanos et al. [75] showed from a survey of the literature that the values of A and E predicted from TGA of polyethylene can vary between 175-325 kJ/mol and 10^{10}-10^{22} s^{-1}, respectively. This fact implies that there might be many solutions to the optimization problem.

Finally, as with any optimization problem the question of local minima arises. Especially when using a gradient-based algorithm like sequential quadratic programming (SQP), there is no test for determining whether the solution is indeed the global minimum. The first two models are first-order linear systems so their solutions will be well-behaved. Furthermore, because both models are in a three-dimensional parameter space, it is possible to explore the behavior of the objective function to some extent. The radical depolymerization model is more difficult on account of it having seven parameters and non-linear terms. In an attempt to overcome these difficulties, a genetic algorithm was employed towards the solution of the radical depolymerization optimization problem. Global search heuristics such as genetic algorithms allow one to find the minimum of several local minima. Unfortunately, the solutions generated by the genetic algorithm all failed to find a smaller E_2 than was found using SQP.

In the following two sections, $\mathbf{K}^*$ and $E_2(\mathbf{K}^*)$ were found for the three models and two materials. In order to check for the uniqueness of the solution, two starting points were taken for each case. It was found that different starting points led to different solutions indicating either the existence of local minima or an objective function that is relatively flat for large regions of the parameter space.

A. PMMA

TGA data for the degradation of PMMA were obtained from Ferriol et al. [78]. The material used was from Aldrich with an initial weight-averaged molecular weight of 350,000 g/mol. The data used were from dynamic experiments at heating rates of 2, 5, 8, and 10 ºC/min.

In order to better understand the behavior of the objective function, for the case of random scission, a three-dimensional surface plot of E_2 vs. A and E was generated (Figure 3.66) for a critical molecule size of a monomer unit. The region computed was limited somewhat because of the high computational cost of integrating the differential equations for large A and small E. Fortunately, this region of the parameter space does not generate results that match the experimental data—for too fast kinetics, all the mass is lost at relatively low temperatures.
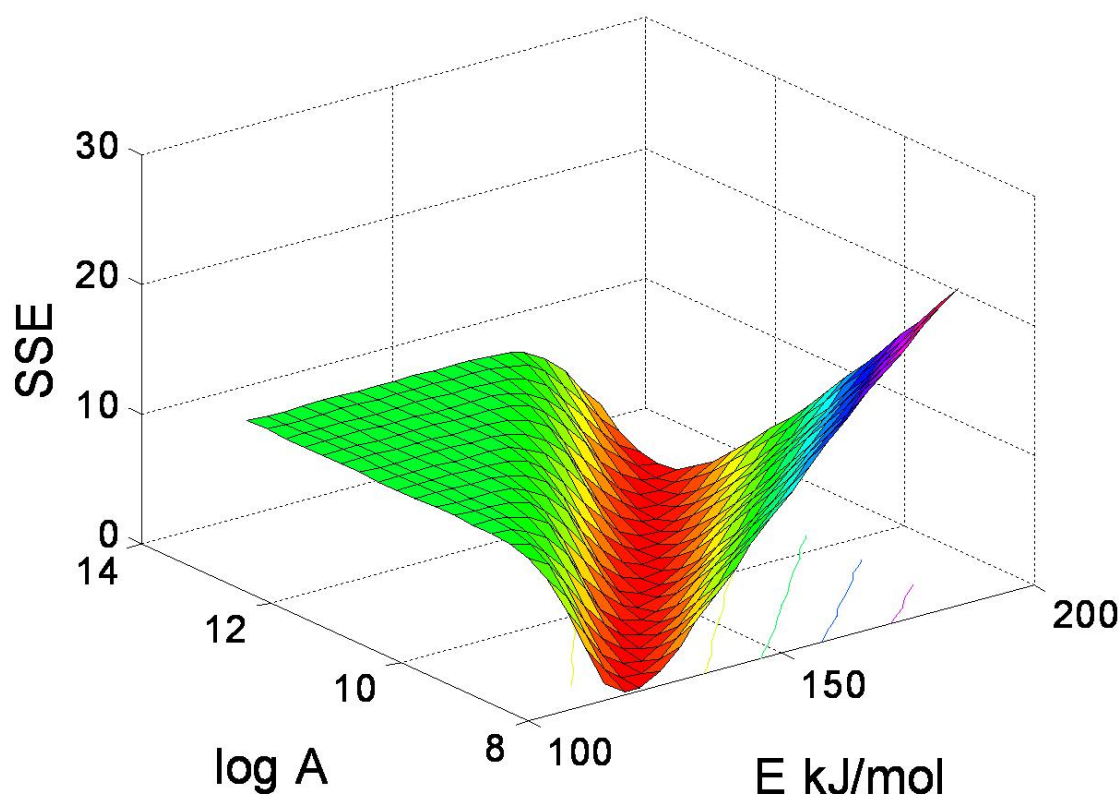
Figure 3.66 Variation of SSE versus kinetic parameters for PMMA with random scission model ($v_c = 100$ g/mol or $N_c = 1$).

Figure 3.66 is interesting for two reasons. First, it clearly shows the kinetic compensation effect: there is a distinct valley in (A,E) along which the model very closely predicts the experimental data. It was found that although the objective function is relatively flat along this kinetic compensation line, there is a distinct but shallow minimum at $A = 5.495e9$ s^{-1} and $E = 130$ kJ/mol. The second interesting feature of Figure 3.66 is the flat region for large A and small E. This is due to the fact that the experimental data points are taken only over a limited range of temperatures. The diagram in Figure 3.67 helps understand this effect. The plot shows experimental and several numerical dynamic TG traces. The large 'x' markers represent experimental data points and the lines represent the results of simulations. The "good" solution represented by the '⋯' will have some small value of E_2 associated with it. However, even though the '— ·· ' solution might, in some sense, be better than the '—' solution, both will have the same E_2 equal to the sum of squared errors of the experimental data with the temperature axis. Although it is not plotted in Figure 3.67, there is a similarly flat region corresponding to simulation results with very slow kinetics—the model completely overshoots the experimental data.
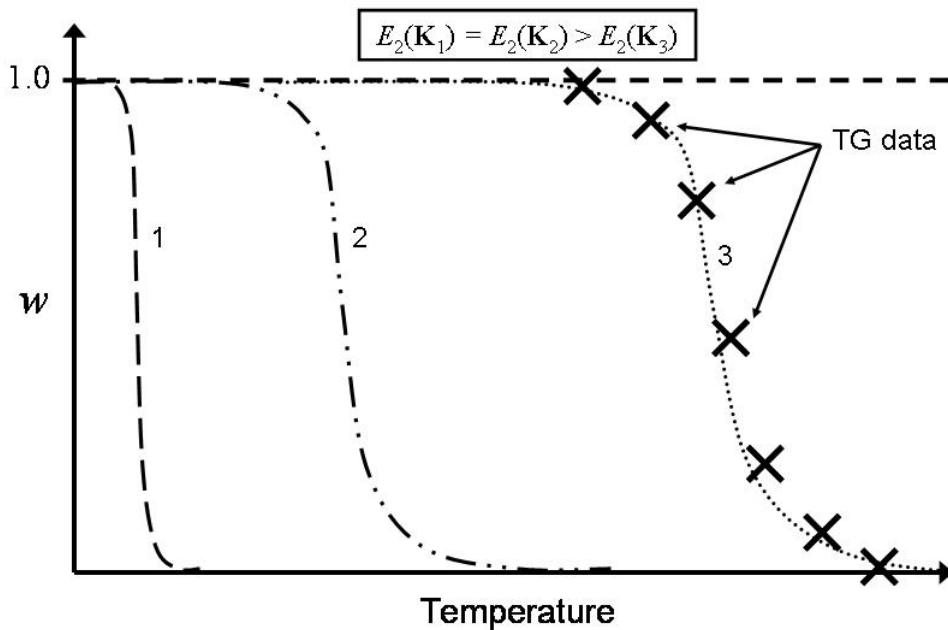
Figure 3.67 Diagram showing the independence of E_2 to K for kinetics much faster than reality.

The value of generating a plot of E_2 such as in Figure 3.66, is to build understanding of the objective function as a preliminary to optimization. A similar plot was done of the variation of E_2 with the critical number of monomer units. For both plots, it was found that the objective function, E_2, is smooth and unimodal. This is evidence that a gradient-based optimization algorithm should perform well. The only possible difficulty is the flatness of the objective function in three regions. In the too fast and too slow regions, the objective function is perfectly flat. Therefore, if a starting point is chosen in one of these regions, the optimality conditions will be satisfied, but the value of E_2 will be large. Consequently, care must be taken to start the optimization algorithm at a point in parameter space where the numerical solution is close to the experimental data. In other words, the algorithm must be started somewhere in the valley seen in Figure 3.66. The third region that might present difficult to an optimization algorithm is the line at the bottom of this valley. Although there are differences in E_2 along this line, for some regions of the parameter space, the differences might be too small to differentiate numerically.

For a three-dimensional space, this type of mapping of the parameter space is not difficult. For the seven-dimensional parameter space corresponding to the radical depolymerization model, this type of mapping is practically infeasible. There will be a kinetic compensation effect for this model, both *within* each reaction, and *between* the

three reactions. It is therefore possible that several local minima exist throughout the parameter space. As was mentioned previously, a genetic algorithm was attempted, but it failed to find a better solution than the SQP algorithm.

A summary of the optimization results for PMMA is presented in Table 3.13. For each model, two starting points were attempted, denoted by $\mathbf{K}_{0,1}$ and $\mathbf{K}_{0,2}$. Different starting points resulted in different solutions for each model. For the Arrhenius and random scission models this is most likely due to the relative flatness of the objective function along the kinetic compensation line. For the radical depolymerization model, it is possible that distinct local minima are being found. In addition to E_2 and $\mathbf{K}^*$, Table 3.13 also includes the zip length for the radical depolymerization solution at a temperature of 600 K—roughly the middle of the reaction. The zip length, $Z = k_D / k_t$ is a measure of the degree to which degradation is dominated by depolymerization.

TABLE 3.13 Summary of Optimization Results for PMMA

Arrhenius	$K_{0,1}$	K^*_1	$K_{0,2}$	K^*_2
E_2	-	0.103	-	0.075
A	3.00E+11	4.54E+11	1.00E+15	1.32E+09
E	1.00E+05	1.87E+05	2.50E+05	1.46E+05
ψ	2	1.56	2.00	1.23
Random Sci.	$K_{0,1}$	K^*_1	$K_{0,2}$	K^*_2
E_2	-	0.189	-	0.436
A	5.00E+09	1.43E+08	1.00E+15	5.79E+15
E	1.30E+05	1.12E+05	2.50E+05	2.21E+05
v_c	0.100	0.100	1.000	5.915
Radical Dep.	$K_{0,1}$	K^*_1	$K_{0,2}$	K^*_2
E_2	-	0.138	-	0.213
A_I	1.00E+06	1.99E+06	1.32E+13	4.77E+13
E_I	1.01E+05	1.03E+05	2.15E+05	2.19E+05
A_D	4.14E+08	7.62E+08	3.45E+14	2.45E+15
E_D	5.28E+04	4.51E+04	1.65E+05	1.61E+05
A_t	1.04E+14	2.17E+14	1.47E+13	1.44E+13
E_t	9.95E+04	1.04E+05	1.90E+05	1.88E+05
v_c	1.000	1.092	0.452	0.451
$Z\ (T=600\ K)$	0.046	0.450	3.52E+03	4.23E+04

The best solution was found with the Arrhenius model. The numerical simulation of this solution along with the experimental data is plotted in Figure 3.68. Much experimental work indicates that PMMA degrades by the radical depolymerization mechanism [47]. Accordingly, one would expect the PBE-based radical depolymerization model to agree more closely with experimental results. Furthermore, since PMMA degradation produces a high yield of mer volatile products, it would be expected that the zip length is very large. This was found to be the case for the second solution only. Finally, one would expect the radical depolymerization model to outperform the other two models simply because it has more than twice as many parameters. The results in Table 3.13 seem to indicate that these hypotheses are false. However, because it was found that the optimal solution is dependent on the starting point, K_0, there is no reason to suppose that the optimal solutions are at true global minima.
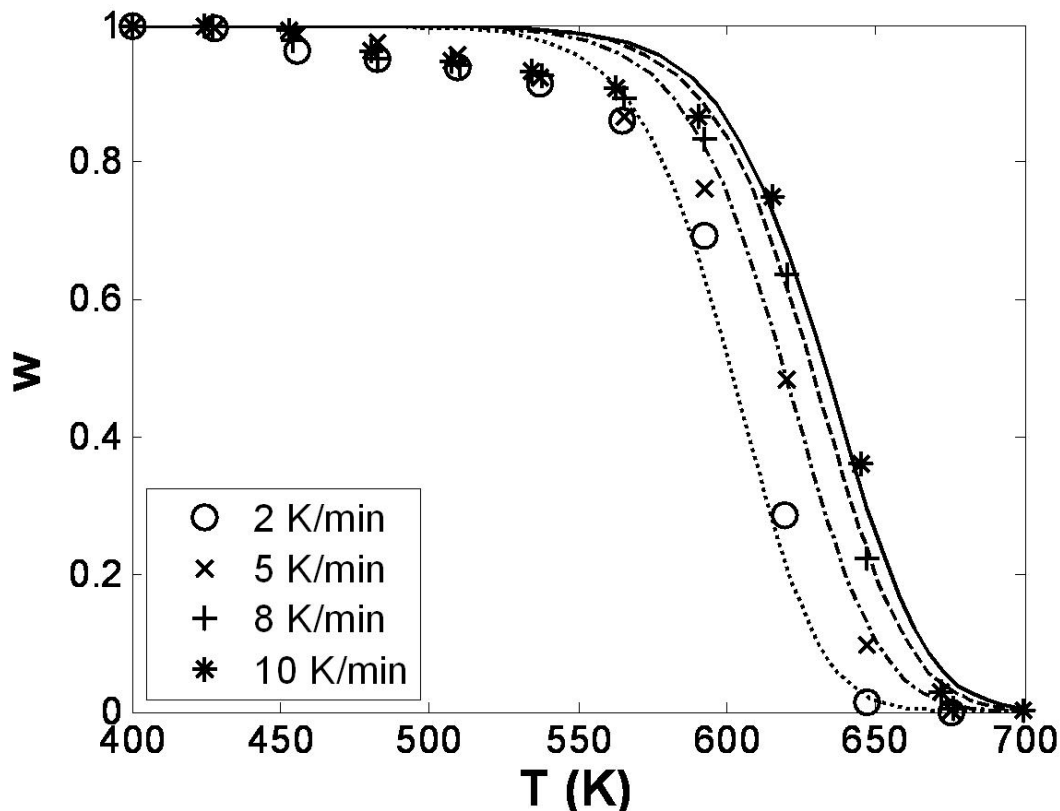

Figure 3.68. Optimal simulation of PMMA dynamic TGA with Arrhenius model and K_2^*.

B. Polyethylene

TGA data for the degradation of PE were obtained from Conesa et al. [75]. The material was a high density PE with an initial weight-averaged molecular weight of

22,000 g/mol. The data used were from dynamic experiments at heating rates of 5, 25, 50, and 100 °C/min.

   The optimization results are compiled in Table 3.14. The best solution was found for the first starting point using the random scission model. The simulated dynamic TG trace with these parameters is plotted in Figure 3.69. As with PMMA, changing the starting point resulted in different solutions, both in terms of E_2 and $\mathbf{K^*}$. Polyethylene is also thought to degrade by the radical depolymerization mechanism, but unlike PMMA, the depropagation reaction is less dominant [47]. Therefore, it should be expected that the random scission and radical depolymerization models perform equally well, and Z should be small.   Again, the results do not support these hypotheses, but since no global minimum could be identified, the models should not be rejected. That is, because the optimization problem is unresolved, the results of this analysis are inconclusive.

TABLE 3.14 Summary of Optimization Results for PE

| Arrhenius	$K_{0,1}$	K^*_1	$K_{0,2}$	K^*_2
E_2	-	0.207	-	0.214
A	3.00E+11	3.84E+11	1.00E+18	1.36E+12
E	1.00E+05	2.00E+05	2.75E+05	2.08E+05
ψ	2	1	2	1
Random Sci.	$K_{0,1}$	K^*_1	$K_{0,2}$	K^*_2
E_2	-	0.045	-	0.254
A	2.00E+12	9.25E+11	1.00E+18	7.03E+14
E	1.80E+05	1.77E+05	2.75E+05	2.20E+05
v_c	0.028	0.028	0.140	0.032
Radical Dep.	$K_{0,1}$	K^*_1	$K_{0,2}$	K^*_2
E_2	-	0.151	-	0.114
A_I	6.00E+13	3.09E+13	1.00E+10	1.06E+13
E_I	2.05E+03	2.06E+05	1.50E+05	2.20E+05
A_D	2.00E+14	9.92E+14	1.00E+10	2.72E+10
E_D	2.00E+05	3.36E+05	1.50E+05	1.18E+05
A_t	2.00E+13	5.07E+15	1.00E+13	4.37E+12
E_t	2.00E+05	2.03E+05	1.50E+05	1.64E+05
v_c	0.112	0.079	0.280	1.428
$Z\ (T=800\ K)$	10	4.23E-10	0.001	6.78
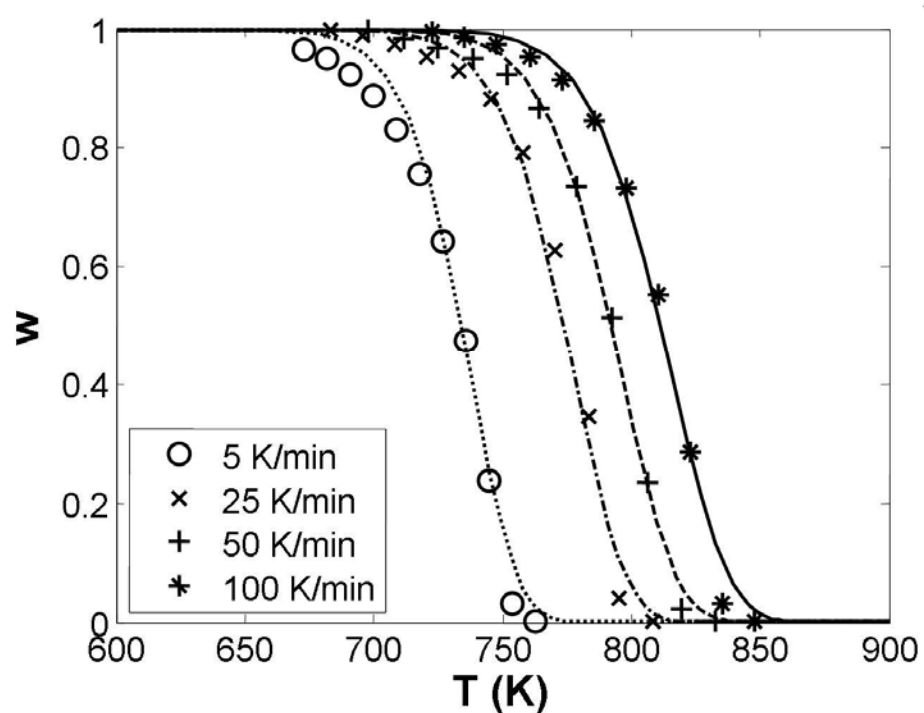
Figure 3.69 Optimal simulation of PE dynamic TGA with random scission model and $\mathbf{K}_1^*$.

3.2.8 Reactive Molecular Dynamics to Find Kinetic Parameters

Reactive molecular dynamics (RMD) is an approach for simulating chemical reactions with the classical equations of motion. Thermal degradation involves several bond breakage events. The rates of these breakage events depend upon the quantum physics of bonding transformations and the classical physics of molecular energy transfer. Molecular energy transfer can be simulated by classical molecular dynamics—assuming that the potential energy surface (PES) of the system is known. In order to account for the quantum mechanical reactive transitions, RMD uses switching functions to model the transition between standard equilibrium forcefields. These switching functions are used to stitch together a complete and smooth PES covering the phase space of the appropriate chemical reactions. The utility of RxnMD for thermal degradation is that it allows for estimates of the rate constants $k(v,T)$ and the scission kernels $\Omega(v,v')$ appearing in, for instance, equation 4.

Smith [79] has implemented RMD in a C++ program called RxnMD. RxnMD is a standard MD code built upon the RMDff forcefield. RMDff is itself based upon the equilibrium (i.e. non-reacting) MM3 forcefield. The switching functions that smoothly bind the equilibrium regions of the PES were determined by fitting functions to the data of quantum chemical calculations. For example, the switching function for a generic scission reaction is assumed to have the form

$$S(RC) = \tfrac{1}{2}\{1 - \tanh[a(RC - RC_0)]\} \tag{39}$$

101

where RC is the reaction coordinate that assumes values between 0 and 1 for points in phase space between the reactants and products. The parameters a and RC_0 are determined from fitting the data of quantum chemical calculations on a representative molecule—for instance, quantum chemical calculations on an ethane molecule were used to determine the switching function for a C—C scission in a polyethylene chain. Currently, RMDff gives a full description of the PES for C—C scission (and recombination), β-scission (and addition), and hydrogen abstraction (and transfer) reactions.

As a demonstration of the ways in which RxnMD can be used to predict kinetic parameters we performed a number of simulations to study the initial scission event in polyethylene chains of varying lengths. In particular, we performed an ensemble of simulations on:

1. a gas phase PE chain consisting of 25 monomer units (i.e. 50 carbon atoms in the backbone);
2. a condensed phase (periodic boundary conditions, PBC) PE chain of 25 units;
3. a condensed phase PE chain of 50 units;
4. a condensed phase system of 50 ethane molecules; and
5. a condensed phase system of 25 ethylene radical molecules.

The systems were created using HyperChem. Classical MD was used to relax the systems to low energy states. The condensed phase systems were constructed such that the density was approximately 0.83 g/cc. Graphical representations of the condensed phase 25 unit PE chain and the 25 molecule ethylene radical system are presented in Figure 3.70 and 3.71, respectively.
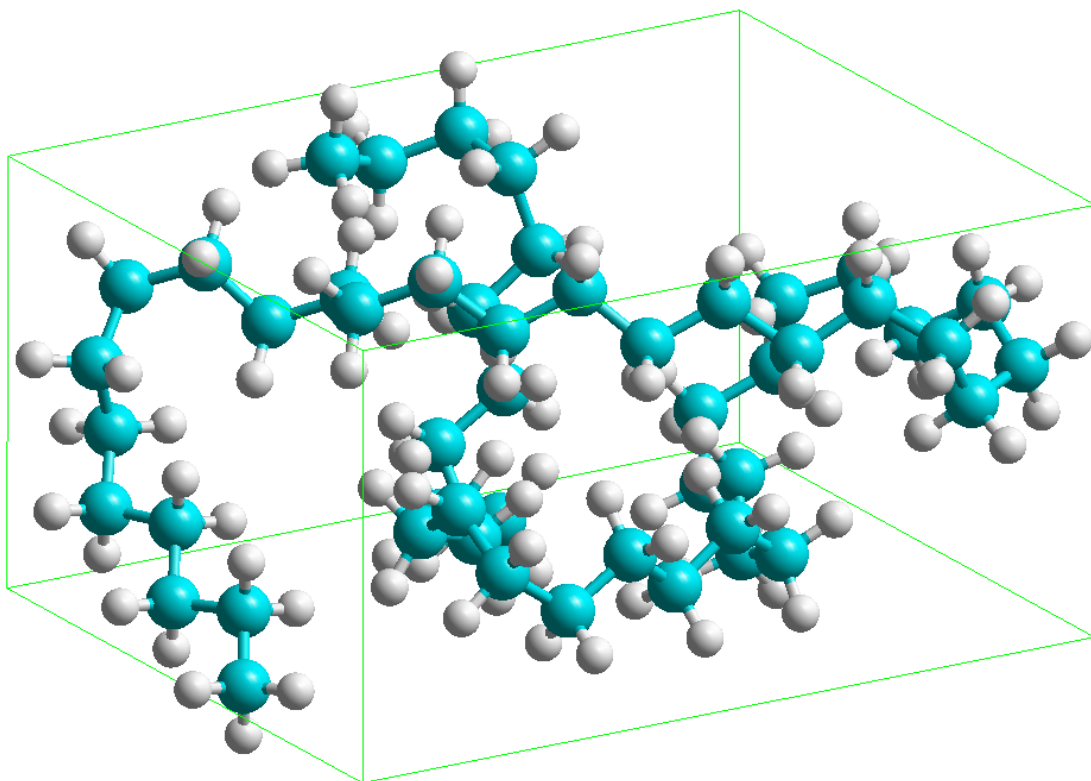
**Figure 3.70** 25 unit polyethylene chain in a periodic box.
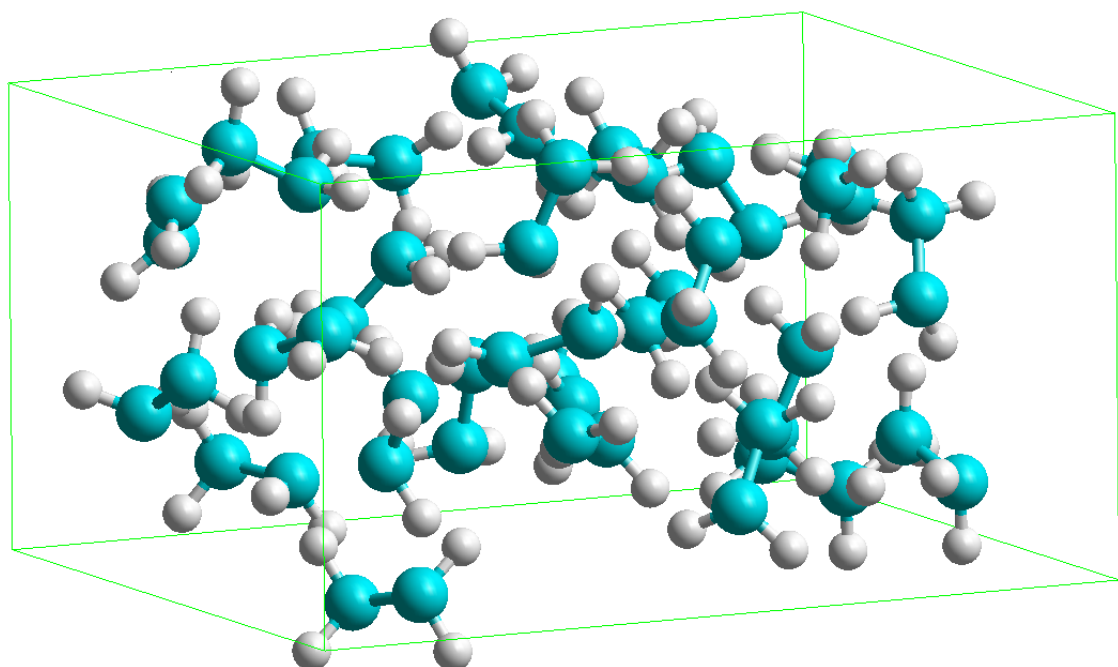
Figure 3.71 50 ethylene radical molecules in a periodic box.

Each of the systems was simulated around 100 to 200 times at temperatures varying
from 2000 K to 4500 K. These temperatures are higher than are experienced in typical

polyethylene degradation but are necessary in order to complete a statistically significant number of simulations in a reasonable amount of time.

Each simulation was begun by randomly assigning velocity vectors to the atoms of the system according to a Boltzmann distribution at the desired simulation temperature. The system was allowed to equilibrate in a thermostat controlled environment (constant temperature) for a total of 5 ps. During this equilibration phase of the simulation, all reactions were "turned off". After equilibration, the C—C scission reaction was "turned on" and the system was simulated at a constant energy. Energy was conserved reasonably well as demonstrated in Figure 3.72 but there is a slight numerical drift. The simulations were continued until the first C—C scission event. The time of this event, $t_{s,i}$ for $i = 1,2,...,N_S$ where N_S is the number of simulations, was recorded along with the location of the broken bond. Because the temperature dependence is required, the average simulation temperature T_i was also recorded.
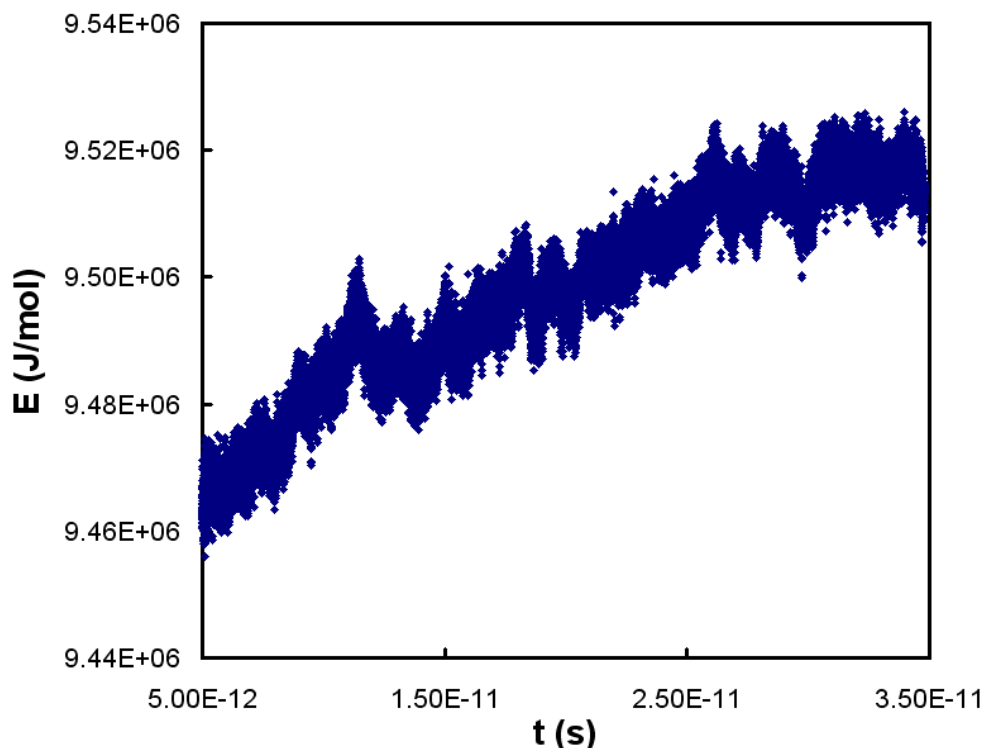
Figure 3.72 Total energy vs. time in a typical simulation of the condensed phase PE 25 system.

The scission rate, $k(v,T)$, is the average time between bond breakage events in an ensemble of molecules of molecular weight, v, at temperature, T. This rate is normalized by the number of bonds in the system. In the RxnMD simulations we measured the time that it takes a typical system to experience a backbone scission. Because the system is typical, it can be assumed that the starting point is uniformly distributed between two

bounding scission events. Mathematically, $k \equiv \langle \Delta \bar{t}_s \rangle^{-1}$ where $\langle \Delta \bar{t}_s \rangle$ is the expected value of the time between scission events per mole of bonds. But since the measured time of scission in RxnMD is uniformly distributed between two scission events, $\langle t'_s \rangle = \frac{1}{2} \langle \Delta t_s \rangle$.

If k has an Arrhenius form, then a plot of $\ln(1/\Delta t_{s,i})$ versus $1/T_i$ should be linearly decreasing. This was found to be the case as is demonstrated in Figure 3.73 which shows Arrhenius plots for the condensed phase 25 unit PE chain and the 25 ethylene radical systems. It was found that the 50 unit PE chain had similar scission times as compared to the 25 unit chain and that the 50 ethane molecules had similar scission times as compared to the 25 ethylene radical molecules.

Activation energies and pre-exponentials can be determined from linear regression fits on the data. Specifically, the pre-exponential is the exponential of the y-intercept and the activation energy is calculated as $E = -(\text{slope} \times R)$. These values are provided in Table 3.15.
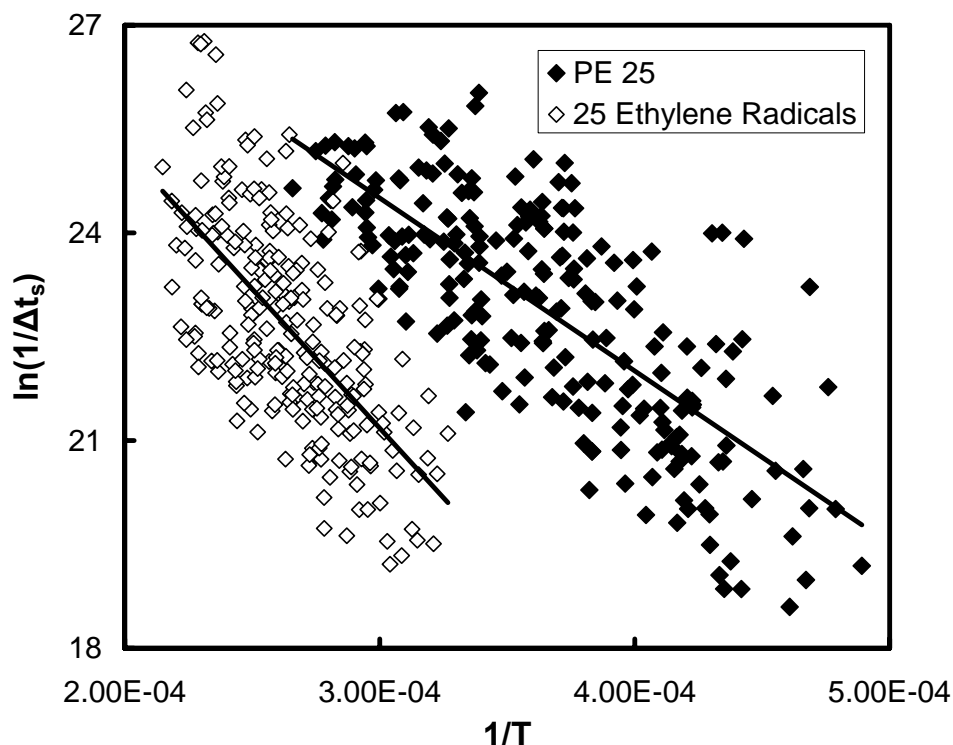

Figure 3.73 Arrhenius plot for two condensed phase systems.

TABLE **3.15 Kinetic Parameters derived from RxnMD Simulations**

System	E (kJ/mol)	A (1/s)
PE 25	208	7.86e13
25 Ethylene Radicals	334	2.71e14

For comparison, Smith [79] found that $E = 233$ kJ/mol and $A = 1.26e14$ s^{-1} for a 50 unit PE chain at a density of 80 g/cc using constant temperature simulations. Also, the comparable C—C bond dissociation energy is 340 kJ/mol and the fundamental C—C frequency is 10^{13} s^{-1}. Our results indicate that bond scission rate (per bond) increases with molecular weight but becomes constant for chains of more than 25 monomer units. Similar results have been observed by Nyden et al. [76-77] who proposed that this molecular weight dependence is due to increased mechanical strain in the longer molecules. In order to more fully resolve the function dependence of k on molecular weight, more simulations must be performed on different sized systems.

The second observed quantity was the bond location for the PE chains. Results for the 25 unit chain are presented in Figure 3.74. This data indicates that the chain scission kernel is uniformly distributed: $\Omega(v, v') = 1/v'$. Smith [79] obtained similar results for an ensemble of constant temperature simulations. Again, more simulations should be performed to confirm that this conclusion is statistically justifiable.
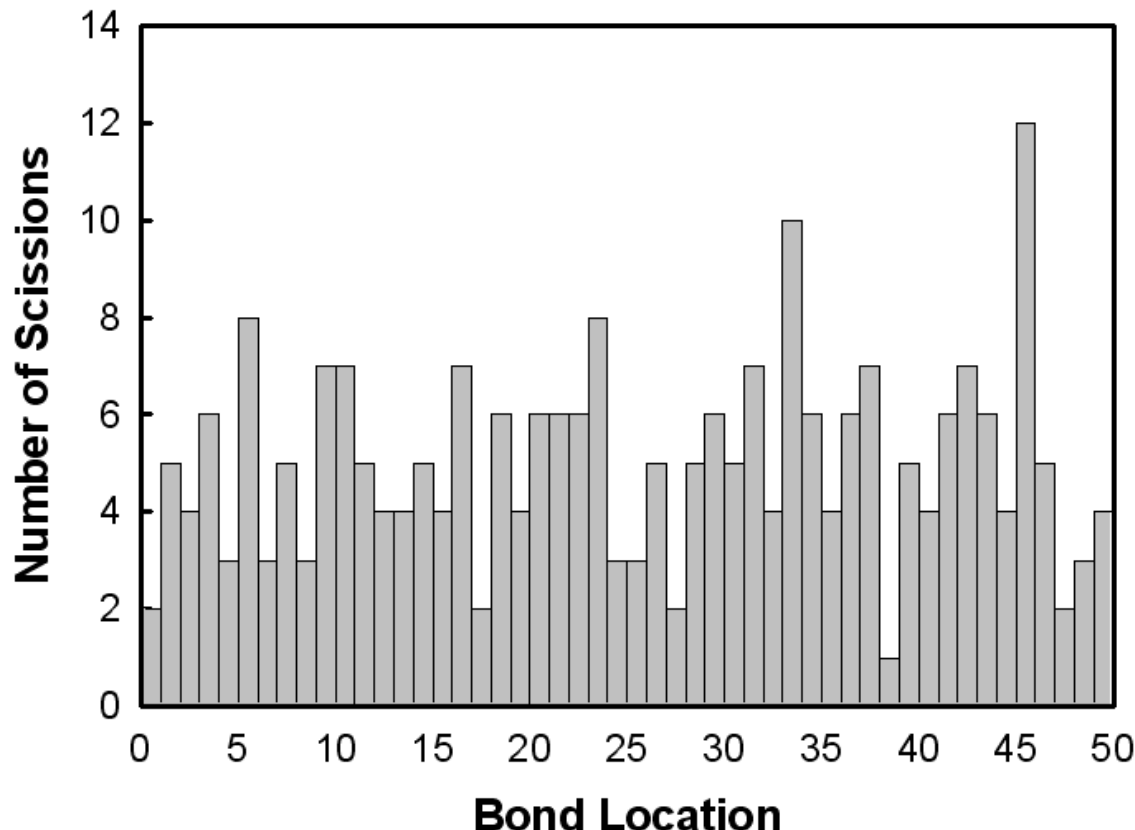
Figure 3.74 Bond location distribution for 25 unit PE chain.

3.3 Publications and Presentations

A total of 35 technical papers were presented/published/prepared through the sponsorship of this research program for the past three years:

1. Koo, J. H., Ho, D. W., and Ezekoye, O. A., "A Review of Numerical and Experimental Characterization of Thermal Protection Materials – Part I. Numerical Modeling", Paper AIAA-2006-4936, *42nd AIAA/ASME/SAE/ASEE Joint Propulsion Conference*, Sacramento, CA, July 9-12, 2006.

2. Koo, J. H., and Ezekoye, O. A., "Experimental and Numerical Characterization of Polymer Nanocomposites for Solid Rocket Motor Internal Insulation – Annual Report (Report 1)," Annual Report to AFOSR, Arlington, VA, Sept. 30, 2006.

3. Koo, J. H., Ho, D. W., Bruns, M., and Ezekoye, O. A., "A Review of Numerical and Experimental Characterization of Thermal Protection Materials - Part II. Material Properties Characterization," Paper AIAA-2007-2131, *48th AIAA/ASME/ASCE/AHS Structures, Structural Dynamics, and Materials Conference*, Waikiki, HI, Apr. 23-26, 2007.

4. Ho, D. W., Koo, J. H., Bruns, M., and Ezekoye, O. A., "A Review of Numerical and Experimental Characterization of Thermal Protection Materials - Part III.

Experimental Testing," Paper AIAA-2007-5773, *43rd AIAA/ASME/SAE/ASEE Joint Propulsion Conference*, Cincinnati, OH, July 8-11, 2007.

5. Bruns, M. C., Ezekoye, O. A., and Koo, J. H., "Determining Failure Time for Weak-Char Ablatives," Paper AIAA-2007-5772, *43rd AIAA/ASME/SAE/ASEE Joint Propulsion Conference*, Cincinnati, OH, July 8-11, 2007.

6. Nguyen, K., Koo, J. H., Ho, D. W., Bruns, M., and Ezekoye, O. A., "Experimental Characterization of Thermoplastic Polyurethane Nanocomposite under Extreme Conditions," Paper AIAA-2007-5770, *43rd AIAA/ASME/SAE/ASEE Joint Propulsion Conference*, Cincinnati, OH, July 8-11, 2007.

7. Luo, Z. P., and Koo, J. H., "Quantifying the dispersion of mixture microstructures," *J. of Microscopy*, 225 (22), 2007, pp. 118-125.

8. Koo, J. H., Ezekoye, O. A., Bruns, M. C., Ho, D. W., and Nguyen, K., "Experimental and Numerical Characterization of Polymer Nanocomposites for Solid Rocket Motor Internal Insulation – Annual Report (Report 2)," Annual Report to AFOSR, Arlington, VA, Sept. 30, 2007.

9. Koo, J. H., and Ezekoye, O.A. "1st Annual Program Review at AFRL/Edwards," Lancaster, CA, Dec. 2007.

10. Ho, D. W., "Determination of Kinetics Parameters and Char Microstructural Analysis of Thermoplastic Polyurethane Elastomer Nanocomposites for Propulsion Systems," MS thesis, Dept. of Mechanical Engineering, The University of Texas at Austin, Austin, TX, Dec. 2007.

11. Nguyen, K. C., "Experimental Characterization of Thermoplastic Polyurethane Elastomer Nanocomposites Under Extreme Conditions," MS thesis, Dept. of Mechanical Engineering, The University of Texas at Austin, Austin, TX, Dec. 2007.

12. Luo, Z. P., and Koo, J. H., "Determining the layer dispersion degree in polymer layered silicate nanocomposites by quantitative transmission electron microscopy," *Polymer*, 49, 2008, pp. 1841-1852.

13. Luo, Z. P., and Koo, J. H., "Quantitative electron microscopy of carbon nanofibers/nanotubes enhanced polymer nanocomposites," *Materials Letters*, 62, 2008, pp. 3493-3496.

14. Ezekoye, O.A., Bruns, M. C., and Koo, J. H., "Polymer Degradation using Population Balance Techniques," *NIST-BFRL 2008 Annual Fire Conference*, Mar. 31, 2008.

15. Bruns, M. C., Koo, J. H., and Ezekoye, O. A., "An Examination of Polymer Degradation and Heat Transfer using Population Balance Techniques," *2008 Spring Technical Meeting of the Central States of the Combustion Institute*, Tuscaloosa, AL, April. 2008.

16. Ho, D. W., Koo, J. H., and Ezekoye, O. A., "Thermoplastic Polyurethane Elastomer Nanocomposites: Morphology, Thermophysical, and Flammability,"

Proc. International SAMPE 2008 Symposium and Exhibit, Long Beach, CA, May 19-22, 2008.

17. Koo, J. H., Ezekoye, O.A., Bruns. M. C., and Lee, J. C., "Semi-Annual Program Review with AFRL/Edwards," Video Conference with AFRL/Edwards AFB personnel, UT-Austin, Austin, TX, June 2008.

18. Ho, D. W., Koo, J. H., Lee, J. C., and Ezekoye, O. A., "Thermophysical Properties Characterization of Thermoplastic Polyurethane Elastomer Nanocomposites," Paper AIAA-2008-5146, *44th AIAA/ASME/SAE/ASEE Joint Propulsion Conference*, Hartford, CT, July 21-23, 2008.

19. Luo, Z. P., and Koo, J. H., "Quantifying the layer dispersion degree in clay/polymer nanocomposites by advanced quantitative transmission electron microscopy," *Proc. MSA 2008 Meeting,* Albuquerque, NM, Aug. 3-7, 2008.

20. Ho, D. W., Koo, J. H., and Ezekoye, O. A., "Kinetics of Thermal Degradation of Thermoplastic Polyurethane Elastomer Nanocomposites," *Proc. International SAMPE 2008 Technical Conference*, Memphis, TN, Sept. 8-11, 2008.

21. Koo, J. H., Ezekoye, O. A., Bruns, Lee, J. C., M. C., Ho, and D. W., Nguyen, K., "Experimental and Numerical Characterization of Polymer Nanocomposites for Solid Rocket Motor Internal Insulation – Annual Report (Report 3)," Annual Report to AFOSR, Arlington, VA, Sept. 30, 2008.

22. Koo, J. H., and Ezekoye, O.A. "2nd Annual Program Review at AFRL/Edwards," Lancaster, CA, Dec. 2008.

23. Bruns, M. C., Koo, J. H., and Ezekoye, O. A., "Population-Based Models of Thermoplastic Degradation: Using Optimization to Determine Model Parameters," *Polym Deg Stab*., 94, (2009), 1013-1022.

24. Ho, D. W., Koo, J. H., and Ezekoye, O. A., "Kinetics and Thermophysical Properties of Polymer Nanocomposites for Solid Rocket Motor Insulation," *J. of Spacecraft and Rockets,* 46 (3), (2009), 526-544.

25. Lee, J., Koo, J. H., and Ezekoye, O. A., "Flammability Studies of Thermoplastic Polyurethane Elastomer Nanocomposites," AIAA-2009-2544, *50th AIAA/ASME/ASCE/AHS/ASC Structures, Structural Dynamics, and Materials Conference*, Palm Spring, CA May 4-7, 2009.

26. Bruns, M. C., Ezekoye, O. A., and Koo, J. H., "Thermal Degradation of a Spatially Lumped Population of Thermoplastic Chains," *6th U.S. National Combustion Meeting*, An Arbor, MI, May 17-20, 2009.

27. Koo, J. H., Ezekoye, O. A., Bruns, M. C., and Lee, J. C., "Characterization of Polymer Nanocomposites for Solid Rocket Motor – Recent Progress," *Proc. International SAMPE 2009 ISSE,* Baltimore, MD, May 18-21, 2009.

28. Lee, J. C., Koo, J. H., Lam, C., Ezekoye, O. A., and Erickson, K., "Heating Rate and Nanoparticle Loading Effects on Thermoplastic Polyurethane Elastomer Nanocomposite Kinetics," AIAA-2009-4096, *AIAA Thermophysics Conference*, San Antonio, TX, June 22-25, 2009.

29. Koo, J. H., Nguyen, K. C., Lee, J. C., Ho, W. C., Bruns, M. C., and Ezekoye, O. A., "Flammability Studies of a Novel Class of Thermoplastic Elastomer Nanocomposites," *J. of Fire Sciences*, July 30 (2009) as doi: 10.1177/0734904109339616.

30. Lee, J. C., Koo, J. H., and Ezekoye, O. A., "Thermoplastic Polyurethane Elastomer Nanocomposites: Density and Hardness Correlation with Flammability Performance," AIAA-2009-5273, *AIAA Joint Propulsion Conference*, Denver, CO, Aug. 2-5, 2009.

31. Ho, D. W., Koo, J. H., and Ezekoye, O. A., "Thermoplastic Polyurethane Elastomer Nanocomposites: Morphology, Thermophysical, and Flammability Properties," *Journal of Nanomaterials*, (2009), under review.

32. Koo, J. H., Ezekoye, O. A., Bruns, and Lee, J. C., "Experimental and Numerical Characterization of Polymer Nanocomposites for Solid Rocket Motor Internal Insulation – Final Report (Report 4)," Final Report to AFOSR, Arlington, VA, Sept. 30, 2009.

33. Koo, J. H., Coates, G. R., Ho, D. W., Bruns, M. C., and Ezekoye, O. A., "A Comprehensive Review of Numerical Modeling and Experimental Characterization of Thermal Protection Materials," an invited paper to *J. of Spacecraft and Rockets* in preparation.

34. Lee, J. C., Koo, J. H., and Ezekoye, O. A., "Roles of Clay, Multiwall Carbon Nanotube, and Carbon Nanofiber to Flammability and Char Strength of Thermoplastic Polyurethane Elastomer Nanocomposites," *J. of Fire Sciences* in preparation.

35. Koo, J. H., Ezekoye, O. A., Lee, J. C., and Bruns, M. C., "Rubber Composites with Layered Clays, Based on Thermoplastic Elastomers," in *Rubber Clay Nanocomposites*, M. Galimberti (eds.), Wiley & Sons, NY (2010) in preparation.

4. SUMMARY AND RECOMMENDATIONS

4.1 Experimental

For this period of performance, we processed and injection molded test specimens for the new TPU Desmopan™ DP 6065A, TPUN-clay (2.5, 5, 7.5, & 10 wt%), TPUN-MWNT (2.5, 5, 7.5, & 10 wt%), and TPUN-CNF (5, 10, 15, & 20 wt%) formulations for material characterization. The intend is to fully characterize the ablation, flammability, mechanical, physical, and thermal properties of these three families of TPUNs. We characterized the physical (density and hardness) of these thirteen (13) TPU and TPUN formulations. The addition of nanoparticle (clay, MWNT, or CNF) into the TPU material increases both the density and shore hardness values.

We have several setbacks in this project due to unforeseen circumstances. As discussed in Section 3.1.8, we were able to design the eroding thermocouple gauge but were unable to fabricate a void-free polymer block of either the TPUN-5%clay or the TPUN-15%CNF material for NANMAC to machine different components of the multi-functional sensor assembly. Better molding techniques of the thick TPUN materials need to be developed before we can successfully fabricate the MFS gauge. SSRM test

specimens in dimension of 4- by 4- by ½-inches of all the TPU, TPUNs, and Kevlar-EPDM specimens were prepared for SSRM ablation tests. TSU's SSRM facility has been under repaired for more than one year, as a result we were unable to conduct SSRM ablation testing at TSU in a timely manner. Unfortunately, this is the only facility that we can conduct ablation test cost-effectively. Half-cone Pi-K motor test specimens were fabricated for all twelve TPUN formulations and shipped to AFRL/EAFB for ablation test. Once the ablation tests are completed, we will analyze the data and report it in an ITAR controlled conference such as JANNAF Propulsion Conference or the National Space and Missile Materials Symposium (NSMMS).

Since we were unable to perform ablation tests, we conducted extensive TGA experiments in air and nitrogen (at low heating rates of 5, 10, & 20°C/min) and determined kinetic parameters for Kevlar-EPDM, neat Desmopan™ DP 6065A, TPUN-clay, TPUN-MWNT, and TPUN-CNF materials using the isoconversion technique. The thermal stability of all TPUNs increases with all nanoparticles in this project. Activation energy of all TPUNs also increases as compared to neat TPUN. We also conducted extensive flammability tests on neat TPU and TPUNs using the UL 94 test method to study the flammability properties as well as char strength of these TPUNs. Under the UL 94 test method, the TPU is flammable. The nanoparticles enhance the formation of char. Results indicate TPUN-7.5 and 10wt% clay form tougher chars than the TPUN-MWNT materials, followed by TPUN-CNF materials. This may able a good indication that TPUN-clay will have better ablation resistant property than TPUN-MWNT and TPUN-CNF materials. We performed detailed microstructural analyses on post-test TPU, TPUN-clay, TPUN-MWNT, TPUN-CNF specimens using SEM analyses to understand the protective mechanisms of each type of nanoparticles in affecting the baseline TPU.

We conducted TGA experiments in nitrogen on TPU, TPUN-5% clay and TPUN-5% MWNT to study their thermal stabilities at high heating rates (100, 250, and 500°C/min) and determined their kinetic parameters using isoconversion technique. Results indicated there is significant difference using low and high heat rating TGA data to calculate kinetics. It will be a concern to use lower heating rate TGA data for high heating rate applications. Additional experiments are planned at Sandia National Lab.

Recommendations:

- Complete characterization of the mechanical properties of this new class of TPUNs

- Prepare selective charred TPUN specimens at Texas State University-San Marcos (TSU) using their simulated solid rocket motor (SSRM) facility for specific heat, thermal diffusivity, and thermal expansion measurements

- Conduct thermophysical properties and thermal expansion measurements of selective virgin and charred TPUNs as a function of elevated temperatures for ablation modeling

- Use our newly developed algorithms to calculate kinetic parameters for these TPUNs

- Fabricate multi-functional sensor using selective TPUN-clay, TPUN-MWNT, and TPUN-CNF materials for UT radiant panel, TSU SSRM, and AFRL/WPAFB LHMEL I testing

- Complete UT radiant panel, TSU SSRM, and AFRL/WPAFB LHMEL I tests using these TPUNs

- Conduct ablation test of TPUNs using the 2-lb Pi-K char motor at AFRL/EAFB

- Conduct ablation test of selective TPUNs using the 15-lb Bates solid rocket motor at AFRL/EAFB

4.2 Numerical

For this period of performance we continued to explore methods for generating more fundamentally based reaction rate constants. It is recognized that these constants could be determined from molecular scale simulations, at least in principle. Rate constants can also be estimated from the results of solving optimization problems (e.g., least squared errors problem). For the case of PMMA and polyethylene, we solved the LSE problem using sequential quadratic programming for the two population-based models as well as a single step reaction-order Arrhenius model. We also worked on adding a connection to molecular modeling using reactive molecular dynamics to estimate the kinetic parameters.

The results of the optimization problem were inconclusive. Although it was found that the population-based models can accurately predict dynamic TG experiments, distinct global minima of the sum of squared errors were not found. The optimization problem is complicated by the flatness of the objective function in the kinetic compensation regions of the parameter space, and the high dimensionality of the parameter space in the case of the radical depolymerization model.

We are continuing investigation into how the MD simulations can provide insight into the details of the chemistry. We are in particular interested in understanding how to define the overall species spectrum during the pyrolysis process.

Recommendations:

- Determine what experimental system best exposes the dependence of heating rate to pyrolysis products

- Generate internal temperature and species fields in quasi-steady ablator model

- Develop modeling approach for product evolution in moment based model

- Formally connect meso-scale and continuum models together

- Continue MD simulations to generate rate constant data

5. REFERENCES

1. Blanski, R., Koo, J. H., Ruth, P., Nguyen, H., Pittman, C., Phillips, S., "Polymer Nanostructured Materials for Solid Rocket Motor Insulation–Ablation Performance," *Proc. 52nd JANNAF Propulsion Meeting*, CPIAC, Columbia, MD, May 2004.

2. Koo, J. H., Marchant, D., Wissler, G., Luo, Z. P., Fernandez, M., Ruth, P., Blanski, R., Phillips, S., "Polymer Nanostructured Materials for Solid Rocket Motor Insulation–Processing, Microstructure, and Mechanical Properties," *Proc. 52nd JANNAF Propulsion Meeting*, CPIAC, Columbia, MD, May 2004.

3. Ruth, P., Blanski, R., Koo, J. H., "Preparation of Polymer Nanostructured Materials for Solid Rocket Motor Insulation," *Proc. 52nd JANNAF Propulsion Meeting*, CPIAC, Columbia, MD, May 2004.

4. Blanski, R., Koo, J. H., Ruth, P., Nguyen, H., Pittman, C., Phillips, S., "Ablation Characteristics of Nanostructured Materials for Solid Rocket Motor Insulation," *Proc. National Space & Missile Materials Symposium*, Seattle, WA, June 21–25, 2004.

5. Koo, J. H., Marchant, D., Wissler, G., Ruth, P., Barker, S., Blanski, R., Phillips, S., "Processing and Characterization of Nanostructured Materials for Solid Rocket Motors," *Proc. National Space & Missile Materials Symposium*, Seattle, WA, June 21-25, 2004.

6. Marchant, D., Koo, J. H., Blanski, R. L., Weber, E. H., Ruth, P. N., Lee, A., Schlaefer, C. E., *228th ACS National Meeting*, Philadelphia, PA, 2004.

7. Vaia, R. A., Price, G., Ruth, P. N., Nguyen, H. T., Lichtenhan, J., "Polymer/layered silicate nanocomposites as high performance ablative materials," *Applied Clay Science*, 15, 1999, pp. 67-92.

8. Patton, R. D., Pittman, C. U., Wang, L., Hill, J. R., Day, A., "Ablation, mechanical and thermal conductivity properties of vapor grown carbon fiber/phenolic matrix composites," *Composites: Part A*, 33, 2002, pp. 243-251.

9. Koo, J. H., Stretz, H., Bray, A., Wootan, W., Mulich, S., Powell, B., Grupa, T., Weispfenning, J., "Phenolic-Clay Nanocomposite for Rocket Propulsion Systems," *Int'l SAMPE Symposium and Exhibition*, 47, 2002, pp. 1085–1099.

10. Koo, J. H., Stretz, H., Bray, A., Weispfenning, J., Luo, Z. P., Blanski, R., Ruth, P., "Nanostructured Ablatives for Rocket Propulsion System – Recent Progress," Paper AIAA-2003-1769, *44th AIAA/ASME/ASCE/AHS Structures, Structural Dynamics, and Materials Conference*, Norfolk, VA, Apr. 7-10, 2003.

11. Koo, J. H., Stretz, H., Bray, A., Weispfenning, J., Luo, Z. P., Wootan, W., "Nanocomposite Rocket Ablative Materials: Processing, Characterization, and Performance," *Int'l SAMPE Symposium and Exhibition*, 48, 2003, pp. 1156–1170.

12. Koo, J. H., Stretz, H., Weispfenning, J., Luo, Z. P., Wootan, W., "Nanocomposite Rocket Ablative Materials: Subscale Ablation Test," *Int'l SAMPE Symposium and Exhibition*, 49, 2004, pp. 1000–1014.

13. Koo, J. H., Pilato, L. A., "Thermal Properties and Microstructures of Polymer Nanostructured Materials," in *Nanoengineering of Structural, Functional, and*

Smart Materials, Schulz, M. J., Kelkar, A. D., and Sundaresan, M. J., (eds.), CRC Press, Boca Raton, FL, 2006, pp. 409-441.

14. Koo, J. H., Pilato, L. A., Wissler, G. E., "Polymer Nanostructure Materials for Propulsion Systems," *J. of Spacecraft and Rockets,* 44(6), 2007, pp. 1250-1262.

15. Donskoi, A. A., *Physico-Chemistry of Elastomer Heat-Shield Materials*, Nova Science Publishers, Commack, NY, 1998.

16. Donskoi, A. A., Baritko, N. V., "Fillers and Their Modifications for Elastomeric Heat-Shielding Materials of Low Density," in *Low Flammability Polymeric Materials*, Zaikov, G. E., Khalturinskii, N. A., (eds.), Nova Science Publishers, Commack, NY, 1999, pp. 119-162.

17. Mares, G., Budrugeac, P., "Thermal and Oxidative Stability of Ethylene-Propylene Rubbers," in *Elastomer Technology Handbook*, Cheremisinoff, M. P., (ed.), CRC Press, Boca Raton, FL, 1993, pp. 461-471.

18. Glockler, J., "Innovative TPE Solutions in Automotive Weatherseal Applications," in *TPE '98 - New Opportunities for Thermoplastic Elastomers '98*, Rapra Technology Ltd., Shawbury, Shropshire, UK, 1998, Paper 13, 1-7.

19. Schrooten, R., "Recent Advancements in the Application Developments of Thermoplastic Vulcanisates (TPE-V)," in *TPE '98 - New Opportunities for Thermoplastic Elastomers '98*, Rapra Technology Ltd., Shawbury, Shropshire, UK, 1998, Paper 2, 1-4.

20. Koo, J. H., Ezekoye, O. A., "Experimental and Numerical Characterization of Polymer Nanocomposites for Solid Rocket Motor Internal Insulation – Annual Report (Report 1)," Annual Report to AFOSR, Arlington, VA, Sept. 30, 2006.

21. Koo, J. H., Ezekoye, O. A., Bruns, M. C., Ho, D. W., Nguyen, K., "Experimental and Numerical Characterization of Polymer Nanocomposites for Solid Rocket Motor Internal Insulation – Annual Report (Report 2)," Annual Report to AFOSR, Arlington, VA, Sept. 30, 2007.

22. Koo, J. H., Ezekoye, O. A., Bruns, Lee, J. C., M. C., Ho, D. W., Nguyen, K., "Experimental and Numerical Characterization of Polymer Nanocomposites for Solid Rocket Motor Internal Insulation – Annual Report (Report 3)," Annual Report to AFOSR, Arlington, VA, Sept. 30, 2008.

23. Typical Physical Properties of Pellethane™-Thermoplastic Polyurethane Elastomers, Dow Chemical Company, Midland, MI, Aug. 2001.

24. Desmopan DP 6065A technical data sheet, Bayer AG, Plastics Business Group, D51368 Leverkusen, Germany.

25. Koo, J. H., *Polymer Nanocomposites: Processing, Characterization, and Applications*, McGraw-Hill, New York, 2006, pp. 10-26.

26. Cloisite® 30B technical data sheet, Southern Clay Products, Gonzales, TX.

27. PR-19-PS CNF technical data sheet, Applied Sciences, Inc./Pyrograf® Products Cedarville, OH.

28. Graphistrength® C100 MWNT technical data sheet, Arkema, Lacq, France.

29. "UL 94: Tests for Flammability of Plastic Materials for Parts in Devices and Appliances," Underwriters Laboratories Inc., Northbrook, IL.

30. Luo, Z. P., Koo, J. H., "Quantifying the dispersion of mixture microstructures," *J. of Microscopy*, 225 (22), 2007, pp. 118-125.

31. Luo, Z. P., Koo, J. H., "Determining the layer dispersion degree in polymer layered silicate nanocomposites by quantitative transmission electron microscopy," *Polymer*, 49, 2008, pp. 1841-1852.

32. Luo, Z. P., Koo, J. H., "Quantitative electron microscopy of carbon nanofibers/nanotubes enhanced polymer nanocomposites," *Materials Letters*, 62, 2008, pp. 3493-3496.

33. Friedman, H. L., "Kinetics of Thermal Degradation of Char-Forming Plastics from Thermogravimetry. Application to a Phenolic Plastic," *Journal of Polymer Science: Part C*, Vol. 6, 1965, pp. 183-195.

34. Henderson, J. B., "An Analytical and Experimental Study of the Pyrolysis of Composite Ablative Materials," PhD Dissertation, Oklahoma State University, Stillwater, OK, Dec. 1980.

35. Henderson, J. B., Tant, M. R., Moore, G. R., Wiebelt, J. A., "Determination of Kinetic Parameters for the Thermal Decomposition of Phenolic Ablative Materials by a Multiple Heating Rate Method," *Thermochimica Acta*, 44, 1981, pp. 253-264.

36. Ceamano, J., Mastral, J. F., Millera, A., Aldea, M. E., "Kinetics of Pyrolysis of High Density Polyethylene: Comparison of Isothermal and Dynamic Experiments," *Journal of Analytical and Applied Pyrolysis*, Vol. 65, 2002, pp. 93-110.

37. Day, M., Budgell, D. R., "Kinetics of the Thermal Degradation of Poly(phenylene sulfide)," *Thermochimica Acta*, Vol. 203, 1992, pp. 465-474.

38. Ho, D. W., Koo, J. H., Lee, J. C., Ezekoye, O. A., "Thermophysical Properties Characterization of Thermoplastic Polyurethane Elastomer Nanocomposites," Paper AIAA-2008-5146, *44th AIAA/ASME/SAE/ASEE Joint Propulsion Conference*, Hartford, CT, July 21-23, 2008.

39. Ho, D. W., Koo, J. H., Ezekoye, O. A., "Kinetics and Thermophysical Properties of Polymer Nanocomposites for Solid Rocket Motor Insulation," *J. of Spacecraft and Rockets,* 46 (3), (2009), 526-544.

40. Lee, J., Koo, J. H., Ezekoye, O. A., "Flammability Studies of Thermoplastic Polyurethane Elastomer Nanocomposites," AIAA-2009-2544, *50th AIAA/ASME/ASCE/AHS/ASC Structures, Structural Dynamics, and Materials Conference*, Palm Spring, CA May 4-7, 2009.

41. Lee, J. C., Koo, J. H., Lam, C., Ezekoye, O. A., Erickson, K., "Heating Rate and Nanoparticle Loading Effects on Thermoplastic Polyurethane Elastomer Nanocomposite Kinetics," AIAA-2009-4096, *AIAA Thermophysics Conference*, San Antonio, TX, June 22-25, 2009.

42. Lee, J. C., Koo, J. H., Ezekoye, O. A., "Thermoplastic Polyurethane Elastomer Nanocomposites: Density, Hardness, and Flammability Properties Correlations," AIAA-2009-5273, *AIAA Joint Propulsion Conference*, Denver, CO, Aug. 2-5, 2009.

43. ASTM D2240–05 "Standard Test Method for Rubber Property—Durometer Hardness", *ASTM International,* West Conshohocken, PA, 2005.

44. Amar, A. J., Blackwell, B. F., Edwards, J. R., "One-dimensional Ablation with Pyrolysis Gas Flow Using a Full Newton's Method and Finite Control Volume Procedure," 39th AIAA Thermophysics Conference, 2007.

45. Quintiere, J. G., *Fundamentals of Fire Phenomena*, John Wiley & Sons, Chichester, 2006.

46. Brown, M. E., *Introduction to Thermal Analysis*, Kluwer Academic Press, Dordrecht, 2001.

47. Grassie, N., Scott, G., *Polymer Degradation and Stabilisation*, Cambridge University Press, Cambridge, 1985.

48. Ramkrishna, D., *Population Balances: Theory and Applications to Particulate Systems in Engineering*, Academic Press, San Diego, 2000.

49. Simha, R., Wall, L. A., Bram, J., "High-Speed Computations in the Kinetics of Free-Radical Degradation. I. Random Initiation," *J Chem Phys*, 29, 1958, pp. 894-904.

50. Boyd, R. H., "Theoretical Depolymerization Kinetics in Polymers Having an Initial "Most Probable" Molecular Weight Distribution," *J Chem Phys*, 31, 1959, pp. 321-328.

51. Boyd, R. H., Lin, T. P., "Theoretical Depolymerization Kinetics. II. The Effect of Molecular-Weight Distribution in Degrading Polymers Undergoing End-Group Initiation," *J Chem Phys*, 45, 1966 pp. 773-777.

52. Boyd, R. H., Lin, T. P., "Theoretical Depolymerization Kinetics III. The Effect of Molecular-Weight Distribution in Degrading Polymers Undergoing Random-Scission Initiation," *J Chem Phys,* 45, 1966, pp. 778-781.

53. Inaba, A., Kashiwagi, T., "A Calculation of Thermal Degradation Initiated by Random Scission. 1. Steady-State Radical Concentration," *Macromolecules*, 19, 1986, pp. 2412-2419.

54. McCoy, B. J., Madras, G., "Degradation Kinetics of Polymers in Solution: Dynamics of Molecular Weight Distributions," *AIChE J*, 43, 1997, pp. 802-809.

55. Madras, G., McCoy, B. J., "Time Evolution to Similarity Solutions for Polymer Degradation," *AIChE J*, 44, 1998, pp. 647-655.

56. Staggs, J. E. J., "Modelling random scission of linear polymers," *Polym Degrad Stab*, 76, 2002, pp. 37-44.

57. Staggs, J. E. J., "Modelling end-chain scission and recombination of linear polymers," *Polym Degrad Stab*, 85, 2004, pp. 759-767.

58. Staggs, J. E. J., "A continuous model for vapourisation of linear polymers by random scission and recombination," *Fire Saf J*, 40, 2005, pp. 610-627.

59. Staggs, J. E. J., "Discrete bond-weighted random scission of linear polymers," *Polymer*, 47, 2006, pp. 897-906.

60. Staggs, J. E. J., "Population balance models for the thermal degradation of PMMA," *Polymer*, 48, 2007, pp. 3868-3876.

61. Ranzi, E., Dente, M., Faravelli, T., Bozzano, G., Fabini, S., Nava, R., Cozzani, V., Tognotti, L., "Kinetic modeling of polyethylene and polypropylene thermal degradation," *J Anal Appl Pyrolysis*, 40-41, 1997, pp. 305-319.

62. Upadhyay, R. R., Ezekoye, O. A., "Evaluation of the 1-point quadrature approximation in QMOM for combined aerosol growth laws," *J Aerosol Sci*, 34, 2003, pp. 1665-1683.

63. Upadhyay, R. R., Ezekoye, O. A., "Treatment of size-dependent aerosol transport processes using quadrature based moment methods," *J Aerosol Sci*, 37, 2006, pp. 799-819.

64. Ozawa, T., "Kinetic Analysis of Derivative Curves in Thermal Analysis," *J Therm Anal*, 2, 1970, pp. 301-324.

65. Flynn, J. H., Wall, L. A., "General Treatment of the Thermogravimetry of Polymers," *J Res Nat Bur Stand*, 70A, 1966, pp. 487-523.

66. McCoy, B. J., Wang, M., "Continuous-Mixture Fragmentation Kinetics: Particle Size Reduction and Molecular Cracking," *Chem Eng Sci*, 49, 1994, pp. 3773.

67. Ziff, R. M., "New solutions to the fragmentation equation," *J Phys A Math Gen*, 24, 1991, pp. 2821-2828.

68. Hathorn, B. C., Sumpter, B. G., Noid, D. W., "On the Distribution of Fragment Sizes in the Fragmentation of Polymer Chains," *Macromol Theory Simul*, 10, 2001, pp. 587-591.

69. Bruns, M. C., Koo, J. H., Ezekoye, O. A., "Population-based models of thermoplastic degradation: Using optimization to determine model parameters," *Polym Degrad Stab*, 94, 2009, pp. 1013-1022.

70. Hu, Q., Rohani, S., Jutan, A., "New Numerical Method for Solving the Dynamic Population Balance Equations," *AIChE J*, 51, 2005, pp. 3000-3006.

71. Madras, G., Chung, G. Y., Smith, J. M., McCoy, B. J., "Molecular Weight Effect on the Dynamics of Polystyrene Degradation," *Ind Eng Chem Res*, 36, 1997, pp. 2019-2024.

72. Chickos, J. S., "Hypothetical Thermodynamic Properties: The Boiling and Critical Temperatures of Polyethylene and Polytetrafluoroethylene," *J Chem Eng Data*, 49, 2004, pp. 518-526.

73. Conesa, J. A., Marcilla, A., Font. R., Caballero, J. A., "Thermogravimetric studies on the thermal decomposition of polyethylene," *J Anal Appl Pyrolysis*, 36, 1996, pp. 1-15.

74. McGraw, R., "Description of Aerosol Dynamics by the Quadrature Method of Moments," *Aerosol Sci Tech*, 27, 1997, pp. 255-265.

75. Ceamanos, J., Mastral, J. F., Millera, A., Aldea, M. E., "Kinetics of pyrolysis of high density polyethylend. Comparison of isothermal and dynamic experiments," *J Anal Appl Pyrolysis*, 65, 2002, pp. 93-110.

76. Nyden, M. R., Stoliarov, S. I., Westmoreland, P. R., Guo, Z. X., Jee, C., "Applications of reactive molecular dynamics to the study of the thermal decomposition of polymers and nanoscale structures," *Mat Sci Eng A*, 365, 2004, pp. 114-121.

77. Stoliarov, S. I., Westmoreland, P. R., Nyden, M. R., Forney, G. P., "A reactive molecular dynamics model of the thermal decomposition in polymers: I. Poly(methyl methacrylate)," *Polymer*, 44, 2003, pp. 883-894.

78. Ferriol, M., Gentilhomme, A., Cochez, M., Oget, N., Mielosynski, J. L., "Thermal degradation of poly(methyl methacrylate) (PMMA): modeling of DTG and TG curves," *Polym Degrad Stab*, 79, 2003, pp. 271-281.

79. Smith, K. D., "Developing Reactive Molecular Dynamics for Understanding Polymer Chemical Kinetics," PhD Dissertation, University of Massachusetts Amherst, 2009.

ACKNOWLEDGMENTS